Advanced Detection and Removal Method of Polymer Residues in Through Silicon Vias (TSV)

Fortschrittliche Detektions-und Entfernungsmethode von Polymerrückständen in Through Silicon Vias (TSV)

der Technischen Fakultät
der Friedrich-Alexander-Universität
Erlangen-Nürnberg
zur Erlangung des Grades

Doktor-Ingenieur

vorgelegt von

Helene Gehles
aus Pawlowka

Als Dissertation genehmigt

von der Technischen Fakultät

der Friedrich-Alexander-Universität Erlangen-Nürnberg

Tag der mündlichen Prüfung: 15/03/2019

Vorsitzende des Promotionsorgans: Prof. Dr. Reinhard Lerch

Gutachter: Prof. Dr. Lothar Pfitzner
Prof. Dr.-Ing. Robert Weigel
Prof. Dr.-Ing. Richard Hagelauer

Abstract

With conventional planar monolithic integrated circuit designs approaching their limits, emerging 3D integration technology is enabling higher levels of performance and functionality using through-silicon vias (TSVs) for vertical interconnections. The basic TSV manufacturing process consists of four major components: formation, isolation, metallization, and passivation. Polymer contaminations formed inside the TSVs during processing can cause delamination of deposited metal and isolation layers, resulting in an immediate or delayed electrical failure of the device. The post-etch polymer removal process usually consists of a wet and dry cleaning sequence, which prepares the wafer surface for subsequent material deposition. With increasing aspect ratios, removal and inspection of the sidewall polymer residue are becoming increasingly difficult.

The first goal of this thesis is to develop a cleaning evaluation method for TSVs after a wet-chemical cleaning that follows a through-spacer-oxide etching step (TSE). Special attention should be paid to the adaption to shrinking dimensions, reduction of the inspection duration, and specimen preparation complexity. Secondly, this thesis intends to formulate an improved cleaning method for a dry or wet cleaning subsequent to a TSE. The new or extended cleaning method should also be adaptable to shrinking dimensions, as well as reduce the cleaning duration compared to previous cleaning times.

As part of a co-operation between the *ams AG* and *FhG IISB,* both a novel TSV wafer cleaning process evaluation method, as well as a cleaning method have been developed. Both methods have been experimentally investigated on the base of TSVs that have been processed up to and including the TSE. For each of these methods, wafers with specific TSV sizes, or rather specific aspect ratios (AR 1:5 and 1:2.5), have been provided by *ams AG*.

For an accurate wafer cleaning evaluation, a new method for sidewall polymer residue detection inside the TSVs has been developed. In general, this method is based on labelling of the sidewall polymers with fluorophores. Due to polymer material characteristics, the small interaction volume, and the location of polymer residue, many of the conventional labelling methods such as chemical or physical activation of the polymer surface cannot be used. For this reason, the newly-developed polymer detection method operates with supercritical CO_2 and its diffusion into the polymer matrix. To this end, an innovative laboratory autoclave has been designed and constructed. The residual polymers are labelled by means of impregnation with fluorophores, which are transported into the polymer matrix with CO_2 as a carrier. A non-destructive examination under a confocal laser scanning microscope (CLSM) detects the existence and location of residue. This novel optical detection method, based on fluorophore pressure impregnation, circumvents the drawbacks of destructive analysis methods and provides an efficient and reproducible procedure to detect polymer residue on wafer-level.

The second part of this thesis involves the development of a novel TSV sidewall polymer stripping method. This method, tested within different TSV aspect ratios following a TSE, consists of a dry and a wet-chemical cleaning, and is based on knowledge gained from fluorophore pressure impregnation experiments and on extended state-of-the art wet cleaning procedures. In accordance with the experimental results, TSV surface wetting behaviour, polymer stripping mechanism, and the influence of CO_2 on polymer residue are discussed. With the novel sidewall polymer stripping method, a total cleaning with reduced cleaning process time for TSVs after the TSE has been realized.

One of the primary findings of this research is that supercritical CO_2 can be applied to polymer detection as well as to TSV cleaning processes. Characteristics such as non-toxicity, non-apparent wafer material interactions, operational simplicity, and competitive price have made CO_2 attractive to the semiconductor manufacturing industry for many years. While CO_2 will presumably not replace the complete wet cleaning chemistry in wafer cleaning technology, due to its many advantages it will likely reduce the cleaning agents to a minimum.

Zusammenfassung

Da herkömmliche planare Designs integrierter Schaltungen an ihre Grenzen stoßen, wurde eine neue Technologie der 3D Integration eingeführt. Unter Verwendung von Through-Silicon-Vias (TSVs) für vertikale Verbindungen ermöglicht die aufkommende 3D-Integrationstechnologie ein höheres Maß an Leistung und Funktionalität.

Der grundlegende TSV-Herstellungsprozess besteht aus vier Hauptkomponenten: Bildung, Isolierung, Metallisierung und Passivierung. Polymerverunreinigungen, die während der Verarbeitung in den TSVs gebildet werden, können eine Ablösung des abgeschiedenen Metalls und der Isolationsschichten verursachen, was zu einem sofortigen oder verzögerten elektrischen Versagen des Bauelementes führt. Zur Vermeidung von Ausfällen auf Grund von Polymerrückständen, werden diese durch eine Reinigung entfernt. Die Entfernung der Polymere nach einem Trockenätzprozess besteht im Grunde aus einer nasschemischen und einer trockenchemischen Reinigungsabfolge. In diesem Sinne wird die Wafer Oberfläche auf die nachfolgende Materialabscheidung vorbereitet. Mit steigendem Aspekt-Verhältnis werden allerdings die Entfernung und auch die anschließende Inspektion auf Polymerrückstände zunehmend schwierig.

Das Ziel dieser Arbeit war es, einerseits eine Methode zur Evaluierung der Reinigungseffizienz zu entwickeln. Dabei sollen primär TSVs nach einem Spacer-Oxid-Ätzschritt untersucht werden. Der Schwerpunkt soll im Besonderen auf die Anpassung an die immer kleiner werden TSV Abmessungen liegen, außerdem soll die Inspektionsdauer und der Aufwand einer Probenvorbereitung deutlich reduziert werden. Zum anderen soll eine verbesserte nass- und/oder trockenchemische Reinigungsmethode von TSV nach einem Spacer-Oxid-Ätzschritt erarbeitet werden. Das neue oder erweiterte Reinigungsverfahren sollte ebenfalls an die immer kleiner werdenden TSV Abmessungen anpassbar sein. Außerdem soll die Reinigungsdauer im Vergleich zur Prozessdauer derzeitiger Reinigungsmethoden deutlich reduziert werden.

Im Rahmen einer Kooperation zwischen der *ams AG* und dem *FhG IISB* wurden sowohl ein neuartiges TSV-Wafer-Reinigungsevaluierungsverfahren als auch ein TSV-Wafer Reinigungsverfahren entwickelt. Beide Methoden wurden experimentell auf der Grundlage von TSV Wafer nach einem Spacer-Oxid-Ätzschritt getestet. Für jedes dieser Verfahren

wurden von der *ams AG* Wafer mit spezifischen TSV-Größen bzw. spezifischen Aspektverhältnissen (AR 1:5 und 1:2,5) zur Verfügung gestellt.

Für eine genaue Bewertung der Wafer-Reinigung wurde ein neues Verfahren zur Detektion von Polymerrückständen in den TSVs entwickelt. Im Allgemeinen basiert diese Methode auf der Markierung der Seitenwandpolymere mit Fluorophoren. Aufgrund der Materialeigenschaften des Polymers, des geringen Volumens und der Lokalisierung von Polymerrückständen können viele der herkömmlichen Markierungsmethoden wie die chemische oder physikalische Aktivierung der Polymeroberfläche nicht angewendet werden. Aus diesem Grund arbeitet die neu entwickelte Polymer-Detektionsmethode mit überkritischem CO_2 und dessen Diffusion in die Polymermatrix. Zu diesem Zweck wurde ein innovativer Laborautoklav konstruiert und angefertigt. Die Kennzeichnung der Restpolymere erfolgt durch Imprägnierung mit Fluorophoren, die mit CO_2 als Träger in die Polymermatrix transportiert werden. Eine zerstörungsfreie Untersuchung unter einem konfokalen Laser-Scanning-Mikroskop (CLSM) erkennt das Vorhandensein und die Lage von Rückständen. Diese neuartige optische Detektionsmethode, die auf der Fluorophor-Druckimprägnierung basiert, umgeht die Nachteile destruktiver Analysemethoden und bietet ein effizientes und reproduzierbares Verfahren zur Detektion von Polymerrückständen auf Waferebene.

Der zweite Teil dieser Arbeit galt der Entwicklung einer neuartigen TSV Seitenwandpolymer-Entfernung. Basierend auf den gewonnen Erkenntnissen aus den Fluorophor-Druck-Imprägnier Experimenten und einer Erweiterung einer Stand-der-Technik Reinigungsmethode, besteht die neuartige Methode aus einer trocken und einer nasschemischen Reinigungssequenz. Diese Methode wurde für TSVs nach einem Spacer-Oxid-Ätzschritt entwickelt und an TSVs verschiedener Aspekt-Verhältnisse getestet. Auf der Grundlage der Untersuchungsergebnisse wurden das TSV Benetzungsverhalten, der Polymerablöse-Mechanismus und die Wirkung von CO_2 auf die Polymerreste diskutiert. Mit der neuartigen Seitenwandpolymerablöse-Methode wurde eine Reinigung mit verminderter Prozessdauer für TSVs mit variierendem Aspekt-Verhältnis nach einem Spacer-Oxid-Ätzschritt erfolgreich realisiert.

Eines der zentralen Erkenntnisse dieser Arbeit ist, dass überkritisches CO_2 sowohl in dem Inspektions- als auch in dem Reinigungsprozess von TSVs eine geeignete Anwendung erlaubt. Eigenschaften wie die Ungiftigkeit, fehlende Zwischenreaktionen mit den restlichen Wafer Materialien, die leichte Handhabung und die niedrigen Anschaffungskosten macht CO_2 seit einiger Zeit zu einem attraktiven Medium in der Halbleiter-Entwicklungsindustrie.

Aufgrund seiner Vorteile wird CO_2 basierte Reinigung die nasschemische Reinigung in der Wafer-Reinigungstechnologie, möglicherweise nicht vollständig ersetzen, aber auf ein Minimum reduzieren.

Contents

Chapter 1 Introduction

Imagine, you are trying to find a blue colored raft that is bobbing up and down somewhere in the world´s oceans!

This quote explains what an engineer must feel when looking for defects only a few nanometers in size on a 200-mm silicon wafer. Measuring instruments designed for quality control are adapted to the constantly growing demands of semiconductor technology, such as ever-decreasing structural sizes. However, at a certain point an alternative method must be developed. This point is reached when the standard methodology of quality control becomes complex, time consuming, or less reliable.

1.1 TSVs for the More than Moore Technology

Since Moore´s law can no longer be fulfilled, More than Moore is progressively gaining importance (more details in chapter 2, section 2.1). In More than Moore technology, three-dimensional integrated circuits with reliable vertical interconnect access are increasingly important. These electrical connections, also known as through-silicon vias (TSVs) are formed by multiple material removal and deposition sequences, which create a hollow cylinder passing completely through a silicon substrate (wafer) or a die. During TSV formation, it is particularly important that the deposited material layer does not delaminate from the TSV sidewall, as this delamination can cause a potential defect of the TSV. A material delamination can occur when previous process-related residue remains on the sidewall; for this reason, the residue, also called sidewall polymer residue, is removed by a cleaning sequence.

In order to save space on the silicon substrate or die, the TSV’s diameter is reduced, which leads to an increased aspect ratio of the TSV. Pursuant to the ITRS roadmap TSVs have, depending on the size of the circuit blocks to be stacked, a minimum diameter of 2-3.5µm (for large circuit blocks) or 0.5-2µm (for smaller circuit blocks) and a maximum aspect ratio of 12:1-20:1 (for large circuit blocks) or 5:1-20:1 (for smaller circuit blocks) [1].

With increasing aspect ratios, not only is the removal of the sidewall polymer residue becoming more difficult, but also the inspection thereof. This fact has already been observed for some time in the semiconductor industry. If the trend of shrinking TSV diameter sizes continues, quick adaption of the TSV metrology and TSV cleaning to the new TSV dimensions is absolutely essential.

Currently, an appropriate inspection of the TSV sidewall can only be achieved through destructive methods, such as a cross-sectional scanning electron microscopy (SEM) inspection. State-of-the-art TSV inspection methods are explained in more detail in section 2.2.2. Since numerous TSVs must be inspected, the sample preparation and TSV inspection is time consuming and costly. In addition, with the continuously-improving cleaning process performance, inspections are becoming more complex. This complexity is due to both the decreasing amount of polymer residue to be detected and random distribution of this residue inside the TSV and across the wafer. The difficulty of polymer removal is determined by many factors, including trench size and geometry, surface tension of the cleaning agent, and the material properties of the fluoropolymer to be removed. To overcome all these obstacles, a cleaning and inspection process utilizing supercritical CO_2 (hereafter $scCO_2$) has been invented.

As part of a co-operation between *ams AG,* an Austrian semiconductor manufacturer, and *FhG IISB,* a German research institute, this thesis investigates a new non-destructive method of evaluating the TSV wafer-cleaning process as well as a new TSV wafer-cleaning method, and adapts both to the next shrinking TSV generation. Both methods were experimentally investigated on the base of TSVs after the through-spacer-oxide etching step (TSE). For both of these methods, wafers with specific TSV sizes or aspect ratios (AR 1:5 and 1:2.5) were provided by *ams AG*. The TSV wafers were stopped at different steps of the redistribution layer (RDL) formation sequence, resulting in various level of contamination.

The first challenge was to detect minute traces of polymer residue inside TSVs with small diameter sizes and high aspect ratios; therefore, a new technique of polymer labelling based on signal amplification was invented. The signal amplification occurs by labelling the polymer with a fluorophore. The fluorophore emits fluorescent light after excitation with light of a corresponding wavelength. The emitted light is recorded optically and provides information about presence of polymer residue. Consequently, the polymer residue no longer need to be detected, because well-characterised fluorophores (encased inside the residue) created exclusively for labelling issues can be detected instead. Therefore, different structure sizes can be inspected in a non-destructive way without interaction with the substrate material.

For the new inspection method developed in this work, a confocal laser scanning microscope (CLSM) was tested to determine its suitability for fluorescent light detection. This microscope applied the principle of fluorescence excitation, taking optical thin sections at successive focal planes, enabling a 3D reconstruction of the fluorophore-labelled polymer matrix. The labelling procedure was performed using a transport medium capable of diffusing into the polymer matrix and simultaneously dissolving the fluorophore. Carbon dioxide in its supercritical state was revealed to be a suitable transport medium on the strength of its physical properties, including its negligible surface tension, gas-like diffusivity, and high dissolving capacity of organic compounds.

Labelling experiments were performed in a laboratory autoclave with an 85-ml capacity. The autoclave was designed and constructed to fulfil process conditions such as adjustable temperature, pressures in the range of $scCO_2$, and process time, as well as absence of specimen material changes. The new labelling method was tested first on TSV wafers after a TSE without a subsequent cleaning. After positive evaluation of the polymer labelling and characterization method on uncleaned wafer samples, which indicated a high degree of polymer residue concentration, the characterization method's detection limit was tested on partially-cleaned samples. For this purpose, samples with a lower degree of contamination were prepared and analysed. Semi-cleaned wafers were prepared by applying only a single wet-cleaning step after completion of the TSE.

For an investigation of up to 200-mm sized wafers, a scale-up of the laboratory autoclave was designed and constructed. The scale-up had additional extensions, including a separate gas cylinder connection for fluid CO_2 supply directly to the autoclave. A mixing unit connected to a syringe pump ensured homogeneous fluorophore-CO_2 dispersion in its supercritical state. By introducing a heating and a cooling plate inside the autoclave, setting the temperature with a minimized time delay was made possible. Temperature and pressure controller as well as two sight glasses facilitated the control of the process conditions.

For the new TSV wafer-cleaning method, the wettability of TSVs with different aspect ratios (AR 1:5 and 1:2.5) and surface properties (hydrophilic and hydrophobic) were analysed. Therefore, a wetting behaviour test, using dispersions of defined surface tension was developed. Additionally, the effect of agitation on the infiltration behaviour was tested. The wetting behaviour test results enabled conclusions to be drawn about possible cleaning agents. It has also emerged that physical properties of $scCO_2$ support the TSV cleaning process in different ways, like polymer swelling or complete penetration in TSV. An additional TSV pre-treatment with $scCO_2$ reduced the cleaning duration many times over.

The research results achieved during the TSV metrology adaption to shrinking TSV diameter sizes contribute towards a better understanding of pressure induced CO_2 diffusion processes in a semi-crystalline polymer and the associated mechanical interactions. The literature provides only a few articles about experiments on CO_2 (especially CO_2 in supercritical state) diffusion in semi-crystalline polymers (in particular polytetrafluoroethylene (PTFE)). Bonavoglia et al. uses direct visualization to obtain swelling of the investigated polymers while sorption was measured using a gravimetric apparatus [2]. While swelling of certain polymers (e.g. Poly(methyl methacrylate) (PMMA)) can be observed with the naked eye other polymers (e.g. PTFE) show no visible identifiable changes in their shape after pressure induced CO_2 diffusion.

This thesis demonstrates also the various possibilities of CO_2 application in different fields of the semiconductor industry like the TSV metrology and polymer residue removal. Using the new developed TSV metrology, dry-etching processes can be optimized by controlling the resulting thickness of the sidewall polymer and thus provide a uniform TSV shape. Additionally, cleaning processes like residue stripping can be evaluated more effective. The experimental results gained in this work can be taken advantage of not only in research institutions but also in fabs[1] since the experiments are performed on wafer samples taken from a modern fab.

---

[1] Semiconductor fabrication plant

1.2 Thesis outline

Chapter 1 provides an overview of motive and topic of this thesis. Theoretical and practical relevance of the research as well as the current scientific situation are outlined in section 1.1.

Chapter 2 introduces the most important definitions of key terms in the field of TSV technology and the state-of-the-art TSV formation. A CLSM, its modular design, and the parameter setting are discussed with regard to application to fluorophore detection. Further, two sequences, the through-wafer etch (TWE) and TSE, are characterized and compared in detail. TSV polymer residue formation mechanism and state-of-the art polymer residue stripping are presented, concluding with related state-of-the art cleaning tools.

Chapter 3 outlines the theoretical principles of the processes taking place during the newly-developed TSV inspection method. The foundation for the first aim of this thesis – a newly-developed TSV inspection method – is formed by CO_2 characteristics, interactions between CO_2 and the fluorophore, CO_2 and the residue polymer concluding, with more adjusted CLSM settings for the selected fluorophore. For the second aim of this thesis – a newly-developed TSV wafer cleaning method – TSV-relevant information about wetting behaviour, trapped air, and polymer undercut, as well as a newly-developed infiltration evaluation test for TSVs with different properties, are presented.

Experimental results achieved during the newly-developed fluorophore impregnation method, wetting experiments on TSV wafers with different surface properties and dimensions, as well as during TSV polymer residue removal, are summarized in chapter 4.

Chapter 5 provides a conclusion of this thesis and recommendations for further studies in this specific field.

Chapter 2 State-of-the-Art and Literature Survey

This chapter introduces Moore´s law as the rule of thumb for the integrated circuit (IC) technology and its development over a period of several years. Furthermore, the concept of 3D integration is explained in detail. Background information on the origins of TSV and its diverse application in semiconductor technology along with a description of the redistribution layer (RDL) formation is provided and concludes section 2.1. Further this chapter covers the literature survey on the key issues of this thesis: TSV inspection and TSV residue stripping.

Section 2.2 summarizes the state-of-the-art inspection methods used for detecting polymer residue inside TSVs. Current and future difficulties in TSV inspection are mentioned. The subsequent section 2.3 Modular Design of a Confocal Laser Scanning Microscope introduces a confocal laser scanning microscope (CLSM) as an alternative to state-of-the-art inspection measurement systems. This section also describes in detail the functionality of the microscope used for inspecting TSVs.

Section 2.4 is divided into six subsections that provide information about criteria to consider when selecting the right fluorophore, the microscope's objective, and its resolution. The pinhole, the detector, and their functioning are explained in subsequent sections, concluding with the software settings and an explanation of the 3D reconstruction.

Section 2.5 provides detailed information about TSV formation using deep reactive ion etching (DRIE), through silicon-oxide-spacer etching (TSE) and the chemical processes that are taking place. Furthermore, polymer formation during the TSE is considered more closely. The state-of-the-art residue stripping procedure and its accompanying chemical reactions are described in Section 2.6. In addition, an alternative polymer stripping method using CO_2 is introduced. The chapter concludes with an overview of possible sequences of wafer cleaning and the difference between single-wafer cleaning and batch-wafer cleaning.

2.1 Motive and Motivation of the TSV Technology

2.1.1 Moore´s Law

Many of the technological advancements that are taken for granted and which enable our interconnected digital world (such as the personal computer), are strongly linked to Moore´s law. In 1965, Gordon E. Moore observed that the number of integrated circuit elements on a chip had doubled every 18 months throughout the history of computing hardware, and predicted this trend would continue “for at least 10 years” [3]. His publication became famous as “Moore’s law” and served as the primary means for predicting technology development in the semiconductor industry. Moreover, Moore noted that for each technology, a minimum cost per component exists. With the number of added components growing, lower yields compensate for increased IC complexity and lead to increased costs [4]. To improve performance and lower cost, greater numbers of integrated circuits must be located on the chip; consequently, the available chip area must be reduced. Ever decreasing sizes of components such as transistors demand innovative solutions not only for the processing tools, but also for the physical feasibility of the components themselves.

The latest transistor measures mere nanometres in size. IBM announced the first functional transistor of 7 nm in July 2015 [5]. However, by reducing the circuit features to the atomic scale, electron behaviour becomes unstable, rendering the transistors unreliable.

The graph depicted in Figure 2.1 illustrates the enormous growth in transistor count since 1978, from only a few in the earliest integrated circuits up to more than two billion today [6].

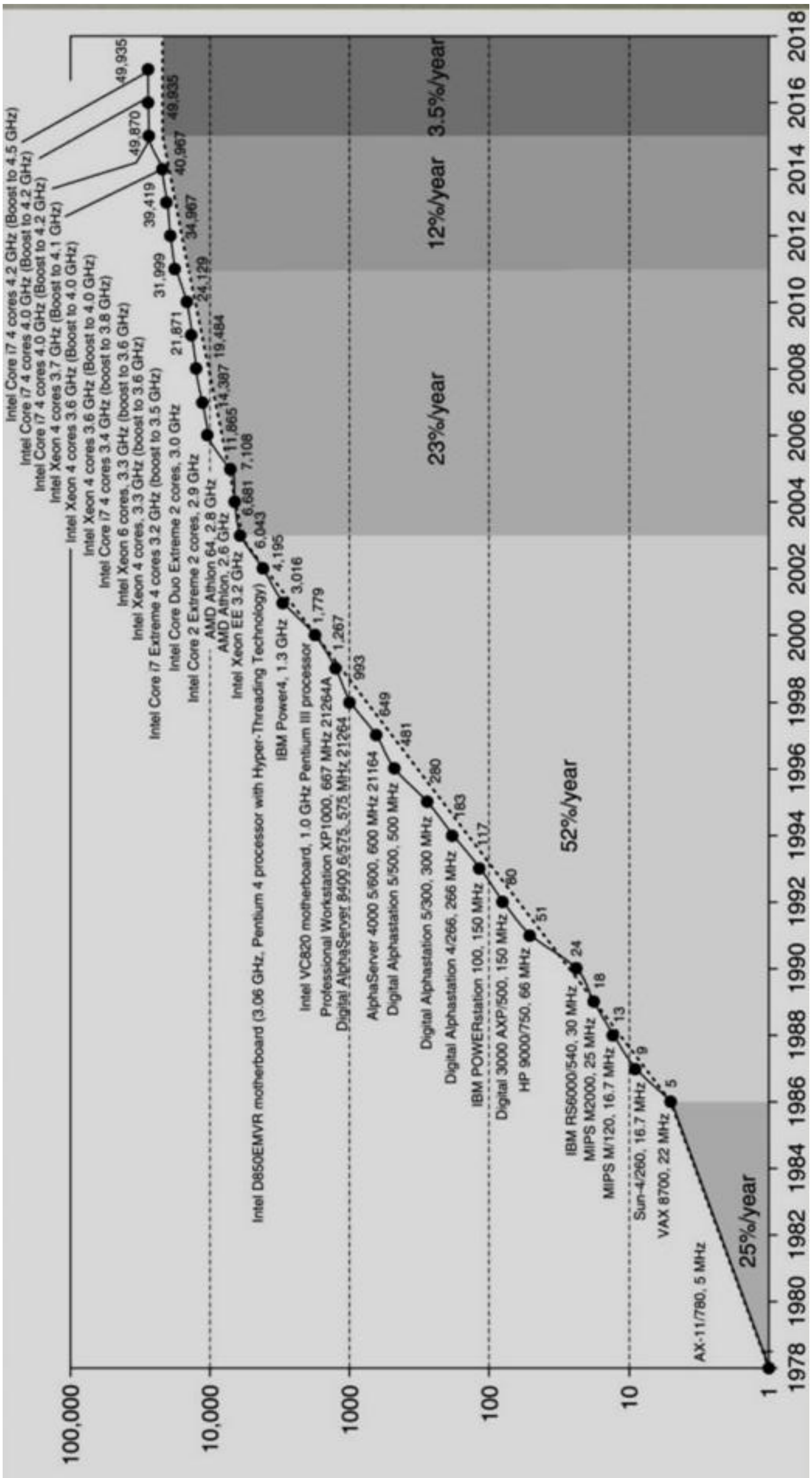

Figure 2. 1: Diagram with expanding transistor counts over the years. [6]

2.1.2 More than Moore

As has been long assumed, “Moore´s law, the most important guideline since the 1960s in the IC technology, is nearing its end.” [7]. This statement was acknowledged by the worldwide semiconductor industry in March 2016. The end of Moore´s law and overcapacities supplied by new Asian companies make it difficult for established suppliers to compete in the international market. The alternative is the More than Moore approach, where the components become application-driven through the addition of functionalities that do not necessarily scale according to Moore’s law. The combination of digital and non-digital functionalities in an integrated system is a design-focused topic that requires new architectures to be examined and new integration options to be developed for the creation of advanced More than Moore devices. These advances include interaction with the environment through appropriate signal transducers such as sensors and actuators. Building-block components such as radio frequency (RF), micro-electro-mechanical systems (MEMS), sensors, and opto- and power devices enable different functionalities. These functionalities may include analogue and mixed-signal processing. Typical More than Moore products with non-digital functionalities include audio or video players, cameras, GPS functionalities, and compasses in mobile devices.

Nevertheless, More than Moore technologies do not exclude the continued shrinking of complementary metal-oxide-semiconductor (CMOS) processes based on the model of Moore´s law; they simply allow non-digital functionalities to migrate from the system board-level into the package which is a casing containing one or more electronic components.

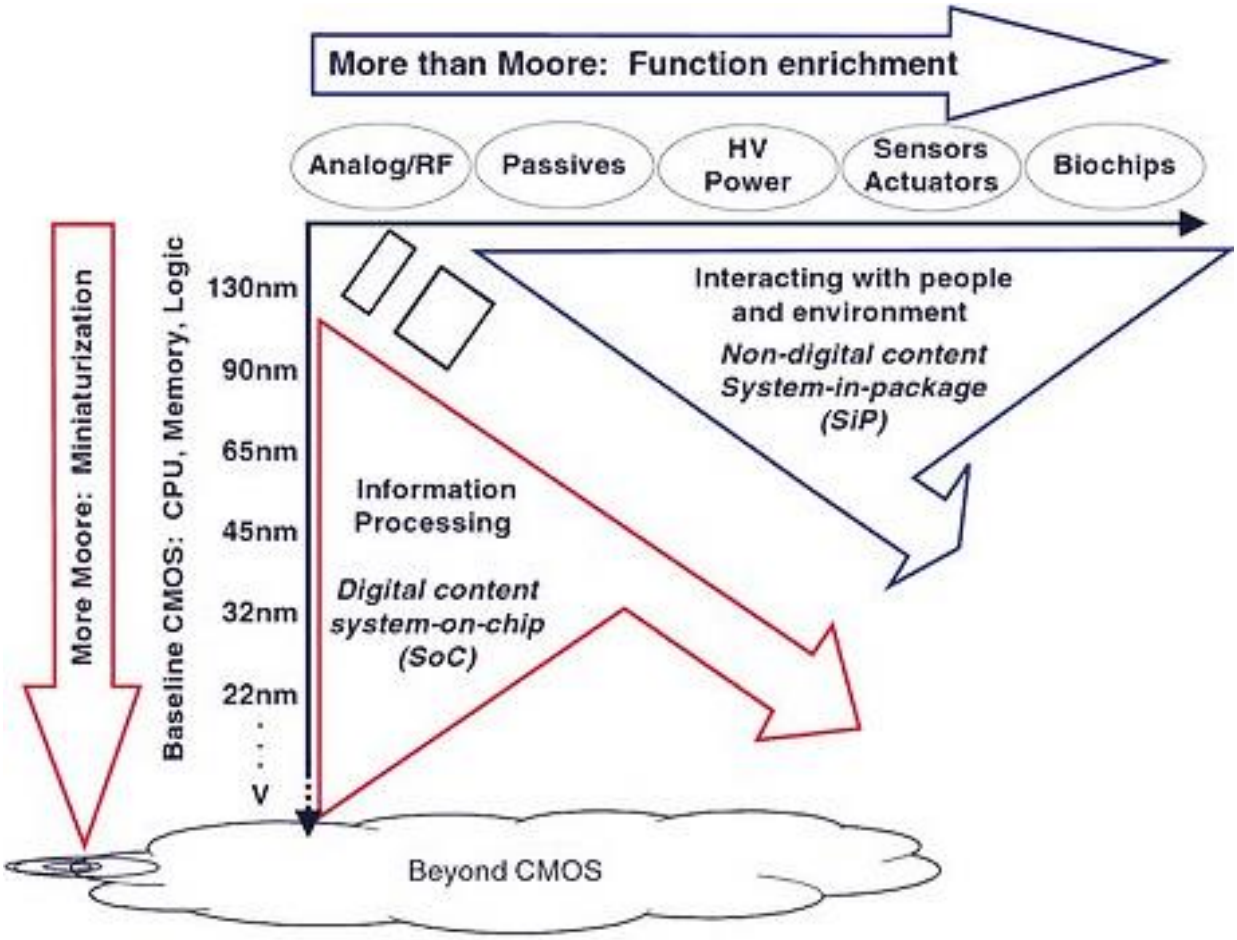

Figure 2. 2: ITRS nanoelectronics technology roadmap. Diagram shows the integration of More Moore technology (with main focus on digital functions) and More than Moore (with main focus on non-digital functions via heterogeneous system integration). [8]

There are two packaging solutions that offer benefits in terms of complexity and component count: System-in-Package (SiP) and System-on-a-Chip (SoC). The international technology roadmap for semiconductors (ITRS) presents the connection between More than Moore and More Moore (which is a scaling as per Moore´s law), as Figure 2.2 illustrates [8]. While More Moore concentrates on miniaturization, More than Moore combines components and enriches device functionalities.

2.1.3 3D Integration

Based on a modular principle, SiP combines existing chips with diverse functionalities in a single package. Figure 2.3 depicts examples of different existing technologies which can be organized in a 3D structure. The chips are electrically connected via wire bonds or TSV. This architecture enables 3D integration, where active electric components are integrated horizontally as well as vertically in two or more layers. Various devices can be integrated in a package (also known as “heterogeneous integration”) with a favourable effect on performance, functionality, and form factor. In this way wafers with a specific function can be interconnected, either chip to wafer or wafer to wafer [9].

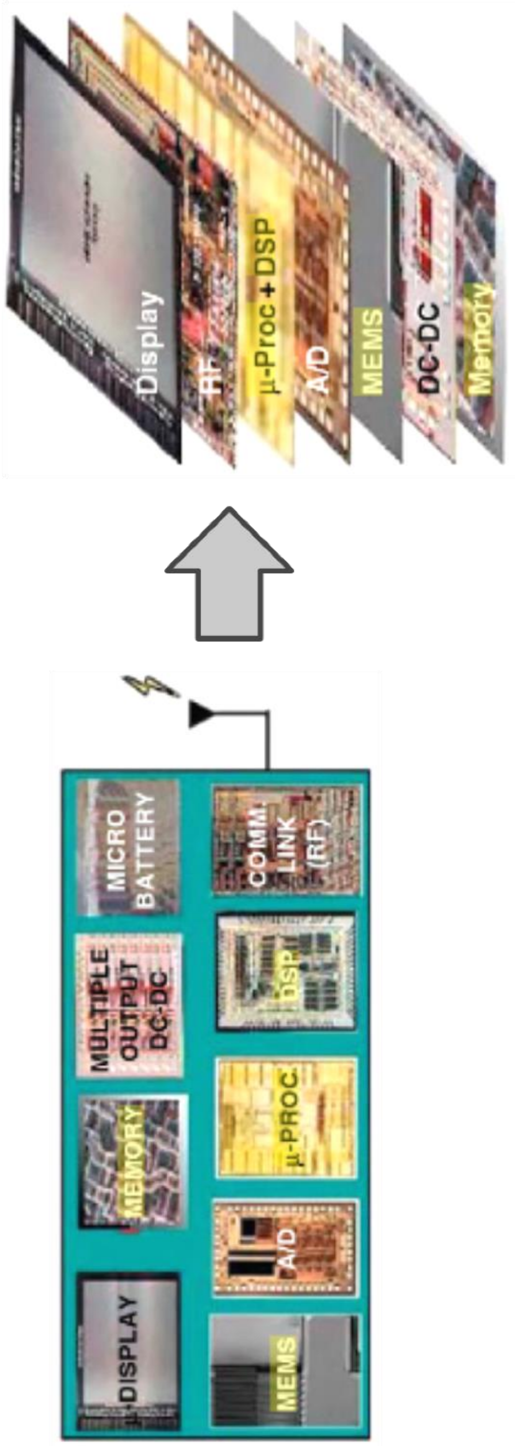

Figure 2. 3: 3D stacking for “heterogeneous integration”. [9]

2.1.4 Through-Silicon Via

A TSV is a technology that employs vertical electrical interconnections passed through a silicon wafer or chip. With increasing numbers of vertically mounted chips, the process complexity and mechanical requirements on the interface between the chip and the wire bonds can become limitless. TSVs are one of the key building blocks for 3D integration technology. The patent “Semiconductive wafer and method of making the same”, which describes the basic idea of a TSV, was filed in 1958 by William Shockley, one of the co-inventers of the transistor [10]. According to a Yole Development business development forecast, the market value of all TSV-packaged devices will represent 9% of the total semiconductor value by 2017 [11]. Starting with low-end applications such as MEMS devices and sensors, TSVs have now been adopted for high-end memory devices, as illustrated in Figure 2.4 [12].

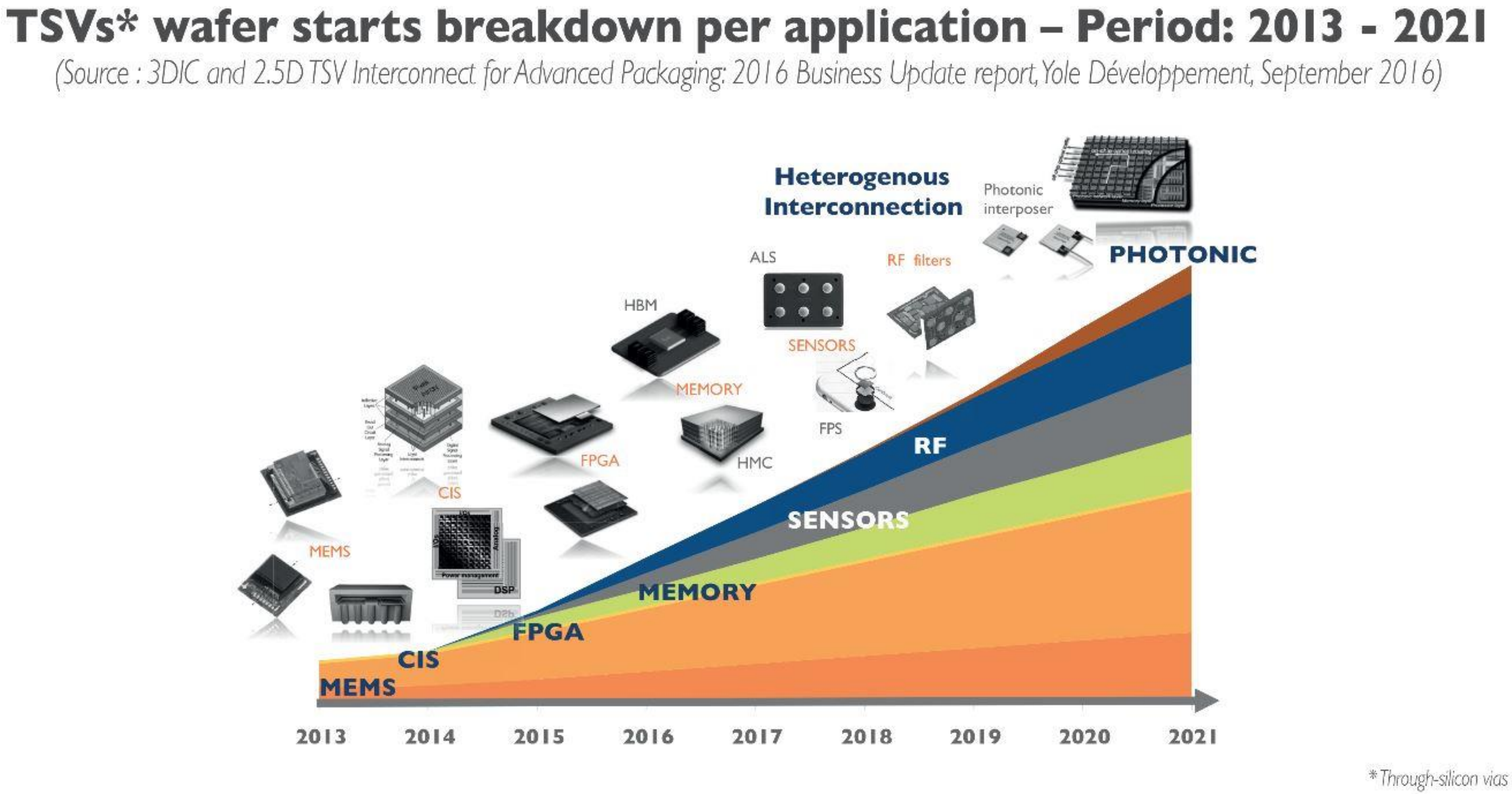

TSVs* wafer starts breakdown per application – Period: 2013 - 2021

(Source : 3DIC and 2.5D TSV Interconnect for Advanced Packaging: 2016 Business Update report, Yole Développement, September 2016)

* Through-silicon vias

Figure 2. 4: 3D TSV application in new packaging strategies. 3D TSV technology is a key solution platform for heterogeneous interconnection, high end memory and performance applications. [12]

2.2 State-of-the-Art TSV Formation and Inspection Method

2.2.1 Adaption to Shrinking TSV Geometry Sizes

As mentioned previously, TSV makes 3D integration technology possible, enabling the stacking of diverse dies. Just as dies undergo modifications that reduce their size and increase their sensitivity and power, TSVs must also adapt. New applications demand new TSV dimensions, which usually tend toward smaller diameter sizes and higher aspect ratios. In order to fulfil these demands, production processes must be adapted to the new requirements. This adaptation often means that along with process parameters, materials must likewise be varied. Certain process steps, including the DRIE of the TSVs, are adjustable, but others, such as optical inspections, are reaching their physical limits.

Various process steps are included in the RDL formation sequence, simplified to seven steps as illustrated in Figure 2.5. A CMOS wafer is fixed on a handling wafer face-down and thinned to a thickness of approximately 200 µm or less. By means of a resist or hard mask, the wafer is structured for the subsequent DRIE step (step 1 of 7), where TSVs are etched from the backside of the now-thinned CMOS wafer (step 2 of 7). Afterwards, a spacer oxide isolation layer is deposited inside the TSVs (step 3 of 7), which is removed at the TSV bottom in the following step (step 4 of 7). After metal deposition and metal etch, the electrical contacts are conducted from the CMOS topside to the backside of the CMOS wafer (step 5 and 6 of 7). The RDL formation concludes with a passivation deposition and pad etch step (step 7 of 7).

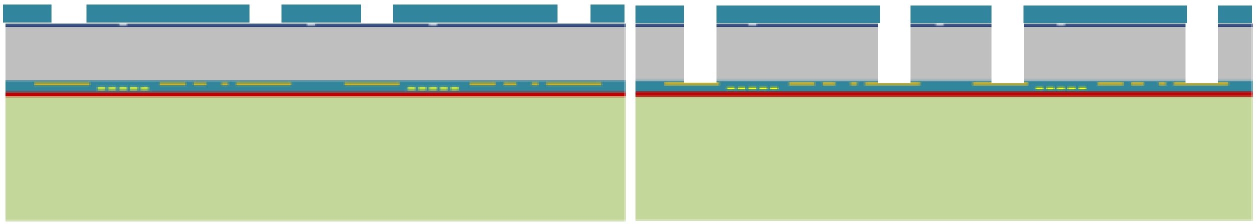

1) TSV Resist-/ hard mask

2) TSV DRIE

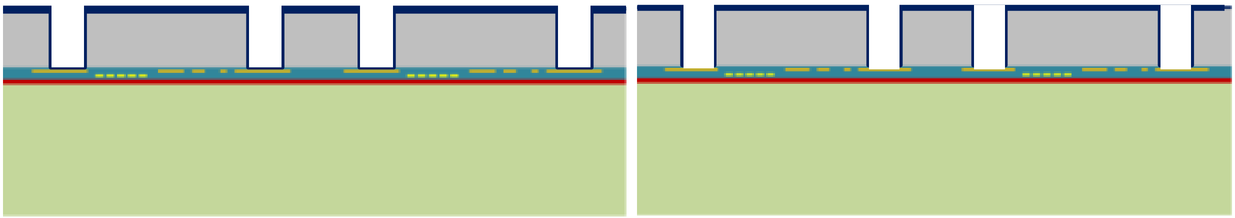

3) Spacer oxide deposition

4) Spacer oxide etch

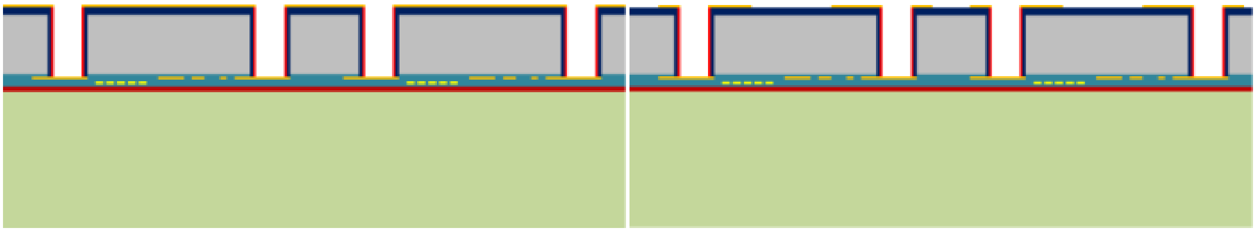

5) Metallization

6) Metal etch

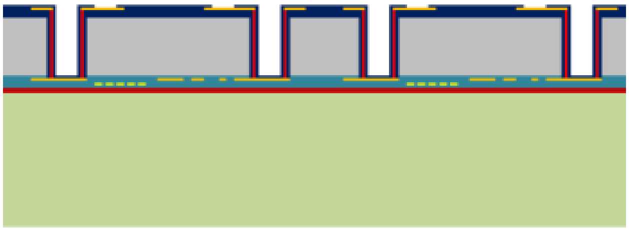

7) Passivation deposition and pad etch

Figure 2. 5: RDL formation sequence. [*ams AG*, presentation slide from the R&D department]

Following the DRIE and TSE, TSV cleaning is crucial, as etch residue can cause delamination of subsequent deposited metal and insulating layers. For this purpose, TSV cleaning is one of the topics covered in this thesis. The second topic is the TSV inspection that follows the cleaning step, which is important for preventing subsequent electrical contact failures. TSV cleaning and TSV inspection are directly interrelated, since a complete removal of residue inside TSVs can only be proven with a reliable inspection of the TSVs.

2.2.2 TSV Inspection

Starting with CMOS wafer multiple-sequential process steps such as wafer bonding, wafer thinning, isolation deposition, metal deposition and etching are applied to fabricate a 2.5D/3D integrated CMOS wafer, while 2.5D and 3D indicates the spatial arrangement of the active electronic components. In addition to the measurement of TSV dimensions such as depth and diameter to monitor the TSV etch process, it is crucial to monitor the quality of the post-etch residue removal process.

During TSV formation, a sub-micrometre thin polymer film is produced at the TSV sidewall, which is removed in the post-etch cleaning step (a detailed description of the TSV formation can be found in section 2.5.1). In order to ensure the cleaning efficiency, TSVs are analysed using state-of-the-art instruments of measurement. In general, a top-down inspection using SEM has been widely adopted for identifying sidewall residue and assessing the cleanliness of the sidewall after a wet clean process [13]. The elemental composition and chemical bonding structure of the polymer residue inside the TSVs can be determined using energy-dispersive X-ray spectroscopy (EDS) and X-ray photoelectron spectroscopy (XPS). In the EDS analysis, the sample surface layer is excited by an electron beam of consistent energy. X-rays emitted by the atoms provide information about the elemental composition. In contrast to EDS, XPS uses an X-ray beam to release photoelectrons from the sample surface layer. The emitted photoelectrons, with specific kinetic energy, are collected by an electron detector. The XPS spectrum is recorded by counting the ejected electrons over a range of kinetic energies, enabling the identification and quantification of surface elements. Although the measuring spot is only a few µm in size (<150 µm), these analytical methods are limited in their application on large topographical structures. Furthermore, these methods produce partly different results for chargeable surfaces, such as XPS peaks shifting to higher binding energies [14]. However, XPS analysis does not yield the bonding and structural information of the polymer, which is necessary to estimate the cross-linking densities of etch residue and subsequently their stripping ability.

In-line inspection methods in the TSV manufacturing process must be capable of determining the presence of polymer residue and sidewall damages. Detection of both factors can be achieved with an in-line, tilted-view scanning electron microscopy inspection. SEM produces images by scanning the sample surface with a focused beam of high-energy electrons, initiating an emission signal in the form of electromagnetic radiation. These electrons are collected by a detector and a corresponding image is generated. Since the TSVs can reach high AR and sometimes have a negative edge, the TSV is tilted during sidewall inspection. To overcome the bottleneck of the tilted-view SEM inspection and to perform a precise inspection of the bottom and sidewall of high AR TSV structures, samples must be inspected in cross-sectional view. This type of inspection requires a time-consuming sample preparation, applying a two-step cleaving procedure. In the first step, samples are prepared using a manual pre-cleaving tool, cleaving close to the structure of interest. In the second step, a precise cleave through the TSV structure is applied using a semi-automated precision cleaving tool. For an accurate inspection, the crack should pass precisely through the TSV middle, resulting in a high-quality perpendicular cross-section. A smooth cleave facilitates polymer residue detection, due to the visible contrast in the area of the edge.

The sample preparation becomes more complicated with shrinking TSV diameters and aspect ratios. In addition, the combination of different material layers with different fracture properties are prone to adversely affect the quality of the sample cleave. A reliable process-monitoring method must be able to determine, preferably in a non-destructive manner, minimal differences in polymer residue concentrations originating from inhomogeneity (wafer centre and wafer edge) of plasma processes such as DRIE. To meet these requirements, a multitude of TSVs must be inspected in cross-sectional view, which makes the detailed inspection very costly and time-consuming.

In general confocal laser scanning microscopy is widely applied in biological science disciplines such as cell biology, but is also used in material science and technology such as visualization of micro-corrosion [15]. However, the application of the CLSM to semiconductor device inspection has not been explored.

2.3 Modular Design of a Confocal Laser Scanning Microscope (CLSM) [16]

CLSM applies the principle of fluorescence excitation for producing high-resolution 3D images of a variety of different sample types. One of the major differences between a standard fluorescence microscope and the CLSM is that the latter can generate optical thin sections. Another important feature of CLSM is the application of a pinhole aperture oriented in a conjugate focal plane to the specimen. Together with a second pinhole aperture that limits the field of illumination, this arrangement of the optical system allows for a significantly improved image resolution, since only light emitted from the focal plane is able to pass through. With these two pinhole apertures, the microscope has the ability to take optical thin sections at successive focal planes, enabling a 3D reconstruction of the sample.

The specimen can be illuminated with lasers of various available wavelengths from UV up to infrared light. For each illuminating wavelength used, a specific fluorophore (which is a fluorescent chemical compound that can re-emit light after light illumination; also described in detail in section 2.4.1) with corresponding excitation wavelength must be selected.

The focused beam of the laser illuminates only a small spot in the specimen, exciting the fluorophore. The emitted fluorescent light is collected by the objective lens, rescanned by the galvanometric mirrors, and focused through the pinhole onto the point detector, which measures the fluorescence intensity for a single spot. This spot corresponds to one pixel of the final image. In order to collect a complete image of the specimen, the light beam has to move across the specimen, scanning it.

A moving mirror deflecting the focused spot enables quick scanning of the specimen to generate an image pixel by pixel. Figure 2.6 depicts an inverted CLSM [17], the same type as was used for inspection of TSVs in this thesis. In this context, an inverted microscope means that the specimen is placed face down and the objectives are located beneath the specimen. Figure 2.6 shows components arranged from left to right beginning with the ① laser source providing monochromatic light of a discrete wavelength, the ② inverted microscope, the two ③ monitors for software setting and specimen view and the ④ control panel where parameters like smart gain, pinhole size, zoom or the z-position can be set.

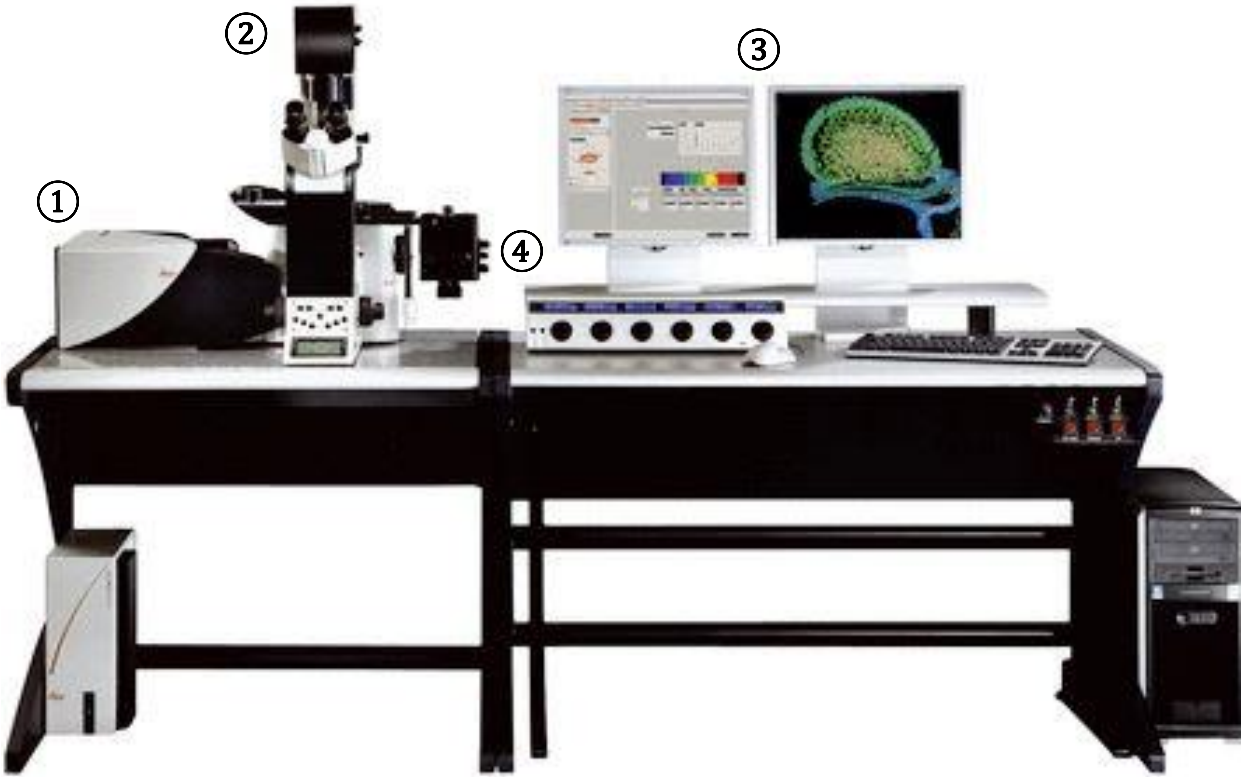

Figure 2. 6: Leica confocal laser scanning microscope SP5 (inverted). [17]

Light Path in a CLSM

The Acousto-Optical Beam-Splitter (AOBS) replaces the dichroic mirror in a CLSM, and is used to separate the illumination and detection paths.

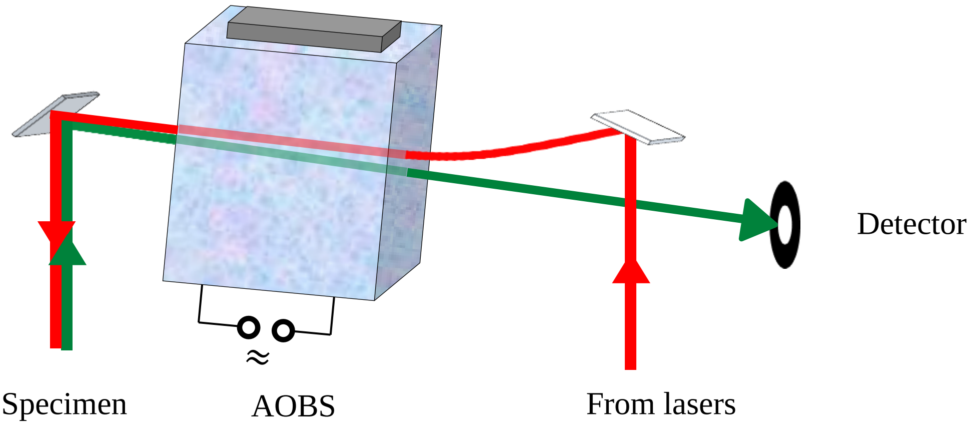

Figure 2. 7: Acousto-Optical Beam Splitter. [16]

The ultrasound field deflects certain bands of wavelength with an accuracy of around 1 nm. The laser light with the desired wavelength (red path in Figure 2.7), which is the excitation light, is directed into the AOBS crystal. When the appropriate radio frequency is set, the light exits the crystal along the optical axis into the specimen and excites the fluorophore. The emitted light with a shifted wavelength up to 20 nm, depending on the fluorophore applied, passes straight through the crystal in the direction of the detector, without being affected by the refractive index grid (green path in Figure 2.7).

The emission is then fed into a multichannel detector (like the schematic sketched five grey squares designated as Detector 1, 2… 5 at Figure 2.8), converting photons into electrical signals.

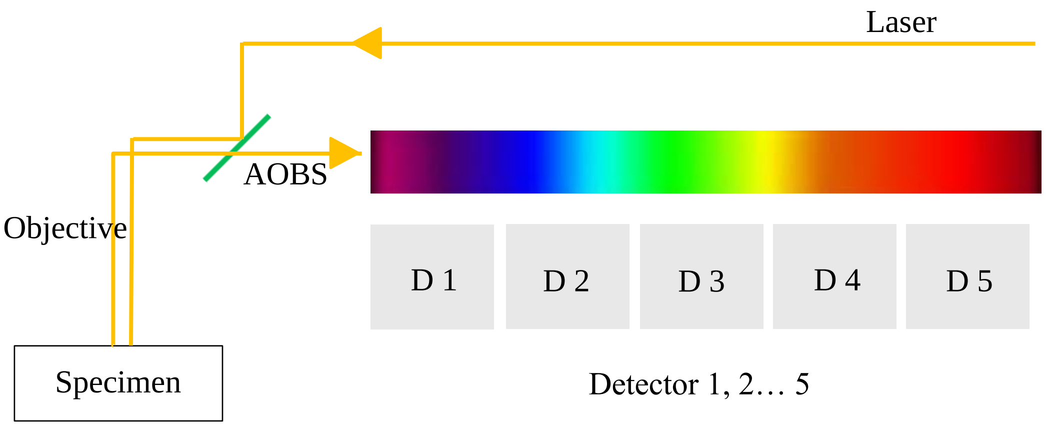

Figure 2. 8: Laser beam and fluorescence light path. [*Leica* LAS AF software]

2.4 Parameter Settings for Confocal Laser Scanning Microscopy

The following definitions provide the basis for a better understanding of available degrees of freedom when using confocal laser scanning microscopy. Starting with the selection of a suitable fluorophore, the quality of the CLSM analysis strongly depends on the objective and the combination of detector types used. This section concludes with the directly connection of bit depth and grey levels in digital images.

2.4.1 Fluorophore

Fluorescence is a spontaneous emission of light which occurs during the transition from an excited state back to a state of lower energy. A fluorophore is therefore a fluorescent chemical compound that emits fluorescent light after excitation with a corresponding wavelength due to its atom grouping that lends fluorescent properties to the chemical compound [18]. Selecting the right fluorophore is paramount for obtaining the best signal for the targeted application. When using a single labelling protocol, there are no constraints in terms of signal separation. The term “labelling” describes the attachment of the fluorophore to the area of interest. However, there are several details that must be considered, such as the chemical compatibility between the fluorophore and the polymer matrix to be labelled. Furthermore, the fluorophore should meet the requirements detailed below.

High Stokes Shift

The Stokes shift is the difference between the wavelength of impinging light and the wavelength of emitted light [19]. Each of the fluorophores has a specific Stokes shift. When the AOBS is turned to the desired radio frequency, the appropriate lines pass through the crystal (see Figure 2.7) to illuminate the specimen. The specimen in turn emits fluorescent light which is shifted by a few nanometers in wavelength. The fluorescent light also enters the crystal and exits unaltered towards the detector. An increasing difference in emission and excitation wavelength facilitates fluorescent light signal detection. In case of a reflective surface and a small Stokes Shift, it is possible that reflected emission light passes the detector and distorts the fluorescent image.

High Quantum Yield

The quantum yield is defined as the ratio of emitted photons to absorbed photons, and represents the probability of an excited fluorophore to produce an emitted photon [19]. In most imaging applications, a high quantum yield is advantageous because the higher the quantum yield of the fluorophore, the brighter the fluorescent signal will be.

Low Photo-Bleaching Rate

Due to external influences such as the utilization of intensive laser power for excitation, fluorophore molecules can undergo a permanent structural change that irreversibly destroys its ability to fluoresce [20], also called photo-bleaching. However, almost all fluorescent dyes fade during observation; some fluorophores even fade after a few nanoseconds, rendering them useless for CLSM analytical purposes. A fluorophore with a low photo-bleaching rate enables therefore an extended specimen observation time.

2.4.2 Microscope Objective

The objective is the first part of the microscope that collects the emitted light coming from the sample. Objectives are optical systems that feature a wide range of properties, including magnification, numerical aperture, and immersion media, among many others. The numerical aperture (NA) is defined as the ability of the objective lens to collect light and resolve it at a fixed distance from the specimen and through a specific media (air, water, or immersion oil).

NA can be described with the formula given in (2.1) below [21]:

$$\mathrm{NA} = \mathrm{n} \sin \mu \tag{2.1}$$

In this formula, μ is the half-angle of the light cone between the specimen and the objective lens, and n is the refractive index of the media between the specimen and the objective. Table 2.1 lists refractive indexes of some frequently-used media in confocal fluorescence microscopy. The higher the refractive index of the medium between the specimen and the objective, the more fluorescent light can be bundled and directed to the lens.

Table 2. 1: Refractive index of air, water and immersion oil.

	Refractive Index n
Air	1
Water	1.33
Immersion oil	1.51

The numerical aperture in particular determines the resolution, whilst the resolution is the smallest resolvable distance between two objects.

The relationship between the resolution and the NA can be explained with following equations (2.2, 2.3) [16]:

$$\mathrm{Resolution}_{\mathrm{x,y}} = 0.37 * \frac{\text{Excitation Laser Wavelength}}{\text{Numerical Aperture}} \tag{2.2}$$

$$\mathrm{Resolution}_{\mathrm{z}} = \frac{0.64 * \text{Excitation Laser Wavelength}}{\mathrm{n} - \sqrt{\mathrm{n}^2 - (\text{Numerical Aperture})^2}} \tag{2.3}$$

These equations are giving the best value that can be expected for fluorescence imaging, whereby the pinhole is infinitely close to zero (pinhole < 0.25 of Airy unit[2]). The Airy unit is the calculated pinhole size that gives the best signal to noise ratio, depending on the objective in use. In general, the axial resolution is higher than the lateral resolution, which means that lateral imaging is sharper than the axial. The axial resolution can be improved by decreasing the excitation wavelength, increasing the NA, or using an immersion medium with a larger refractive index.

2.4.3 Pinhole

Collection of all the emission light makes the structural resolution of the specimen impossible. In order to decrease the amount of light created as a result of laser excitation of the fluorophore, a pinhole aperture is used in a CLSM. With the application of appropriate settings, the pinhole aperture enables the recording of sharp and high-resolution images. The pinhole is by default set to a value of 1 Airy unit, which corresponds to an opening diameter of approximately 60 µm for the equipment used in this thesis. The smallest pinhole diameter measures 20 µm, which can be increased up to a maximum of 500 µm in µm step size.

2.4.4 Detector

Two principle types of detectors are used in the confocal microscopy: the photomultiplier tube (PMT) (Figure 2.9a), and the improved hybrid detector (HyD) (Figure 2.9b). Both detector types use a planar light-sensitive photocathode that converts emitted light photons that hit the detector to photoelectrons. The photoelectrons are amplified on the way to the detection anode. On the anode, an electrical (analogue) signal is created, digitized to a grey level

---

[2] 1 Airy unit is defined as Airy disc diameter multiplied by the magnification of lens. The Airy disc diameter in turn is approximately $1.22 \times {}^{\lambda}/_{NA}$. λ is the emission wavelength and NA the numerical aperture.

(described in greater detail in section 2.4.5), and stored as information with a precise x, y location for the focal point.

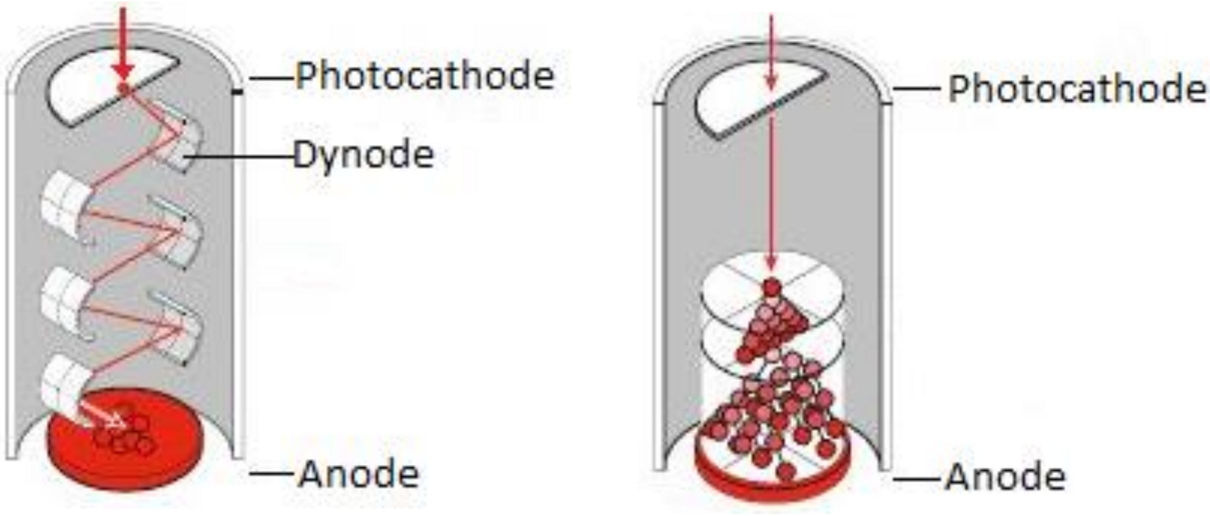

Figure 2. 9: Schematic image of the photomultiplier tube (a) and hybrid detector (b) setup. [17]

The PMTs use multiple dynodes as electron multipliers that amplify not only the signal, but also the noise. Since only small percentage of the photons that hit the photosensitive photocathode is detected, this detector type is less sensitive. However, PMTs can capture a one-megapixel (1024x1024) image in approximately one second [22]. The photoelectrons inside a HyD are created in a vacuum and accelerated in a strong electrical field, passing an avalanche-diode. This enhancement generates less noise and higher sensitivity. In contrast to PMTs, HyDs are capable of photo counting, which allows for quantitative imaging. Because of the high sensitivity provided by HyDs, excitation laser power can be reduced, which in turn reduces photobleaching of the fluorophores.

2.4.5 Software (Data Evaluation)

Nearly every parameter, including laser power, filter choice, focus control, mirror speed, pinhole size, and detector voltage, among others, is controlled and recorded by computers. The detector measures the electron signals that are converted from analogue to digital, and simultaneously creates an image of the scanned sample pixel by pixel. The pixel size is determined by the bit depth, which can be set manually. With increasing bit depth, the number of grey levels increases, leading to smoother-appearing transitions from black to white in the digital image. However, the Nyquist criterion states that the smallest detail that can be resolved by the optics should be represented by 2.3 pixels [23]. The image is oversampled when smaller pixel size is selected, resulting in higher bleaching and increased noise while no extra spatial information is produced. Using pixels larger than the optimal size will result in lower axial resolution than is given by the optics. The following schematic picture (Figure 2.10) illustrates the correlation between bit depth and the number of grey levels in digital images. Level 0 represents black, while the top level represents white, and each intermediate level is a different shade of grey [24]. Therefore, a high bit depth provides a correspondingly high number of shades per pixel, increasing the intensity of the resulting image.

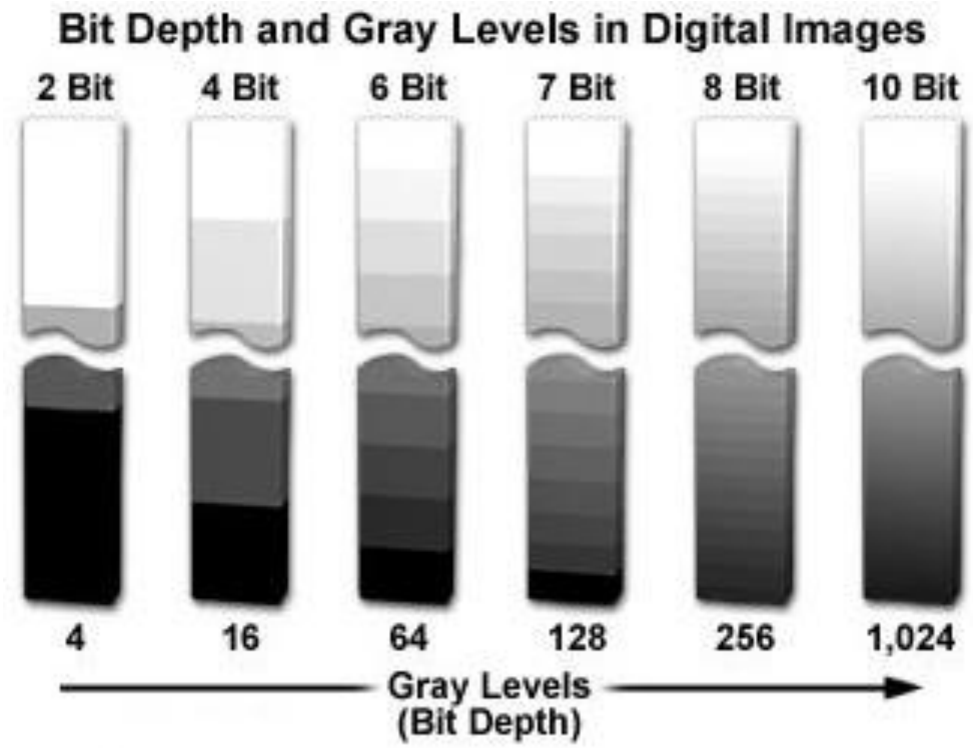

Figure 2. 10: Bit depth and grey levels in digital images. [24]

The pixel size has a direct effect on the quality of the fluorescent image. Pixels that are too large can merge several fluorescent spots into one larger spot, resulting in a reduction of the image resolution. For example, a bit depth of 12 provides a pixel value between 0 and 4095. Every detected signal is assigned one of these numbers according to the signal's intensity, as can be observed in the example in Figure 2.11. Each number illustrated in Figure 2.11a corresponds to a defined pixel, as depicted in Figure 2.11b.

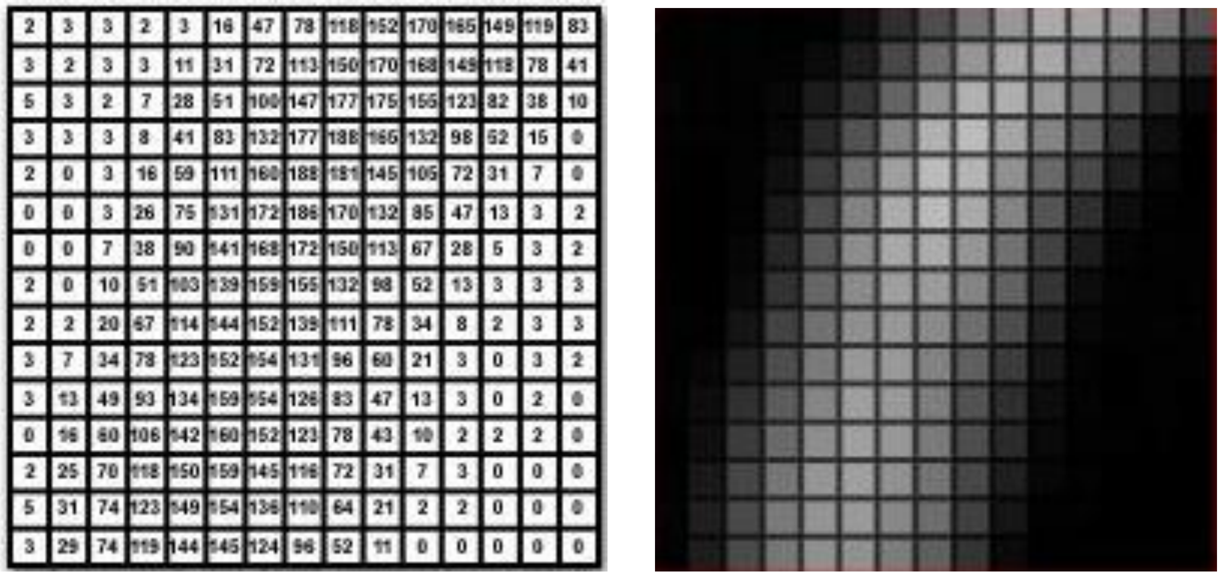

2	3	3	2	3	16	47	78	118	152	170	165	149	119	83
3	2	3	3	11	31	72	113	150	170	168	149	118	78	41
5	3	2	7	28	51	100	147	177	175	155	123	82	38	10
3	3	3	8	41	83	132	177	188	166	132	98	52	15	0
2	0	3	16	59	111	160	188	181	145	105	72	31	7	0
0	0	3	26	75	131	172	186	170	132	85	47	13	3	2
0	0	7	38	90	141	168	172	150	113	67	28	5	3	2
2	0	10	51	103	139	159	155	132	98	52	13	3	3	3
2	2	20	67	114	144	152	139	111	78	34	8	2	3	3
3	7	34	78	123	152	154	131	96	60	21	3	0	3	2
3	13	49	93	134	159	154	126	83	47	13	3	0	2	0
0	16	60	106	142	160	152	123	78	43	10	2	2	2	0
2	25	70	118	150	159	145	116	72	31	7	3	0	0	0
5	31	74	123	149	154	136	110	64	21	2	2	0	0	0
3	29	74	119	144	145	124	96	52	11	0	0	0	0	0

(a) (b)

Figure 2. 11: Analogue (a) to digital image (b) translation. [24]

2.4.6 3D Reconstruction

A cube representing a segment of the specimen volume is dimensioned by selecting the start and end points or plane of the vertical stack. After focusing on one level, the microscope begins to capture images in defined intervals from the bottom to the top of the stack, or vice versa. From the complete set of images of the Z-stack, the software generates a 3D data set. The maximum intensity projection enables detection of the level of maximal fluorescent intensity (highest concentration of labelled substance) in the recorded Z-stack.

2.5 TSV and Polymer Residue Formation

As mentioned in Chapter 1, TSV post-etch residue stripping is the second focus of this thesis. The following sections introduce more details regarding the TSV sidewall polymer formation and the state-of-the-art stripping of these residue.

To prevent remaining polymer residue, a number of intermediate cleaning steps are performed throughout the entire TSV fabrication process. After a process characterization by means of fluorophore pressure impregnation (FPI), the post through silicon-oxide-spacer etching (TSE) cleaning sequence is optimized. In the following section, the TSV formation and the TSE procedure are described in detail.

2.5.1 DRIE for TSV Formation

It was the “Bosch process”, invented by Robert Bosch GmbH in the 1990s, that enabled today’s TSV technology [25]. For the first time, it became possible to etch deep trenches in silicon by using DRIE, a process which involves a repeating sequence of etching and passivating. Prior to etching, the exact positions of the TSVs on the wafer must be defined via photolithography, using an infrared alignment-capable exposure tool. Either the photoresist itself or a structured underlying silicon dioxide can act as a masking layer for the DRIE process. The wafer with the exposed TSV positions is placed in a plasma chamber on a negatively grounded holder. A silicon etching gas is introduced into the plasma chamber. This gas dissociates energized plasma in an RF into electrons, positive ions, and radicals. The positive ions are attracted to the cathode or, in this case, the biased wafer. The ions hit the wafer and molecule layers are uniformly removed by sputtering. As a result, ions are responsible for the physical etching while the free radicals are responsible for dry chemical etching. Free radicals are atoms or molecules that have at least one unpaired electron and are therefore unstable and highly reactive.

The etch gas sulfur hexafluoride provides fluorine radicals, depositing them on the silicon surface (reaction 2.4). The free radicals react with the surface, creating volatile reaction products that are released from the surface and then removed from the chamber (reaction 2.5) [26].

$$\mathrm{SF_6} + \mathrm{e^-} \rightarrow \mathrm{SF_n} + (6 - \mathrm{n}) * \mathrm{F^*} + \mathrm{e^-} \text{ with } \mathrm{n} = 0,..5 \tag{2.4}$$

$$\mathrm{Si} + 4\mathrm{F^*} \rightarrow \mathrm{SiF_4} \uparrow \tag{2.5}$$

Increased feed of SF_6 leads to increased erosion of silicon on the trench sidewalls, resulting in an isotropic etching profile. To inhibit lateral etching inside the trench, a protection layer must be deposited. Therefore, a C_4F_8 precursor is usually introduced into the plasma chamber; this precursor splits into smaller fragments (e.g., CF_x) and, due to plasma energy, into radicals and ions (reaction 2.6). These radicals are deposited on the substrate surface and polymerize to a polytetrafluoroethylene (PTFE)-like polymer (reaction 2.7). The adhesion of these radicals to the generated polymer and a polymer-free silicon surface is assumed to be equal.

$$\mathrm{CF_4} + \mathrm{e^-} \rightarrow \mathrm{CF_x^+} + \mathrm{CF_x^{\cdot}} + \mathrm{F^{\cdot}} + 2\mathrm{e^-} \tag{2.6}$$

$$\mathrm{nCF_x^{\cdot}} \rightarrow \mathrm{nCF_{2(adsorption)}} \rightarrow \mathrm{nCF_{2(polymerization)}} \tag{2.7}$$

The protective polymer is then removed from the TSV bottom by directed sputtering with the etching gas ions. Therefore, every etch cycle underetches the polymer and forms a ribbed structure also known as a scallop [27] (Figure 2.12). Depending on the etching and passivating cycle times, the scallops can be more or less pronounced. With longer etching cycles, the sidewall roughness increases. The polymer deposition must be precisely controlled as well, since the polymer thickness is of crucial importance in determining the TSV diameter and its taper. Thin polymer layers, resulting from too short deposition cycles or too low C_4F_8 flow rates, can be permeated by fluorine radicals generating etch defects on the silicone sidewalls. An additional effect of excessive thin sidewall polymers is a negative TSV profile. In contrast, excessive thick polymer layers, resulting from long deposition times and high C_4F_8 flow rates, are able to cause a reduction of the TSV diameter. However, multiple etching and passivation cycles are performed, while the sidewalls of the trench remain covered by the fluorocarbon polymer.

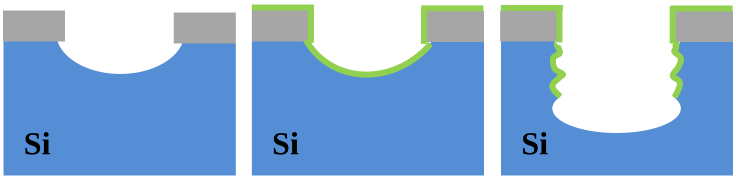

Figure 2. 12: Schematic picture of first steps in DRIE.

The Bosch process is therefore beneficial, because high-aspect-ratio trenches can be etched straight down, independent of the crystal orientation. Applications predominantly benefiting from DRIE can be found in MEMS, power electronics, microfluidic devices, and micro-optics.

2.5.2 Through Silicon-Oxide-Spacer Etch (TSE)

TSE is a dry etching process used for removal of SiO_2 on the TSV bottom after isolation deposition.

$$C_4F_6 + e^- \rightarrow CF_x^+ + CF_x^{\cdot} + e^- \tag{2.8}$$

$$Ar + e^- \rightarrow Ar^+ + 2e^- \tag{2.9}$$

$$O_2 + e^- \rightarrow O_2^{\cdot} + 2e^- \tag{2.10}$$

$$SiO_2 + CF_x + \text{"damage"} \rightarrow SiF_4 + (CO, CO_2, COF_2, \text{etc.}) \tag{2.11}$$

During the TSE step, hexafluoro-1, 3-butadiene (C_4F_6) dissociates, producing neutral fluorine radicals (reaction 2.8), which chemisorb on the SiO_2 surface and react under formation of volatile compounds. In addition to the C_4F_6 etching gas, oxygen and argon are added to the plasma chamber. The ionized argon atoms (reaction 2.9) are accelerated towards the biased wafer surface, inducing an ion bombardment. Although the SiO_2 etching rate is lower for C_4F_6-Ar, than for C_4F_8-Ar gas combination, the etching selectivity of SiO_2 compared to photoresist and silicon are higher for C_4F_6-Ar than for C_4F_8-Ar [28]. The primary etching species is atomic fluorine [29]. CF_2 and CF_3 are absorbed on the SiO_2 surface but do not dissociate or react with the surface without ion bombardment. The necessary surface damage occurs during impact of Ar^+ ions. After the Si-O bonds are broken and oxygen is released, fluorine starts to etch the silicon. The released oxygen reacts further with carbon and fluorocarbon radicals, forming CO, CO_2 and COF_2. The low etch rate for SiO_2 compared to Si can be increased by damaging the surface via ion bombardment (reaction 2.11). Additionally, oxygen is added for removal of emerging polymer layers on the surface (reaction 2.10). This gas combination results in a relative high CF_x deposition rate, leading to a high polymer thickness. Besides increasing the polymer thickness, the Ar^+ ion bombardment also reduces the fluorine content in the polymer.

Although no sidewall passivation polymer is used in TSE, residue remain on TSV sidewalls. According to literature [30], during etching of silicon, the addition of small amounts of oxygen (< 5 %) to a CF_4 plasma increases the fluorine-atom density dramatically, and thus the silicon etch rate. Unsaturated CFx species are consumed by oxygen, suppressing polymer formation on the surface. At higher O_2 content (> 7.5 %), a passivating inorganic $Si_xO_yF_z$ film is formed on the Si surface.

During TSE, the metal contacts are exposed. Figure 2.13 depicts a schematic picture of a grinded CMOS wafer bonded to a handling wafer. The first and second images display three TSVs before and after TSE. The oxide layer is removed and the metal contacts on the bottom of the TSV are revealed.

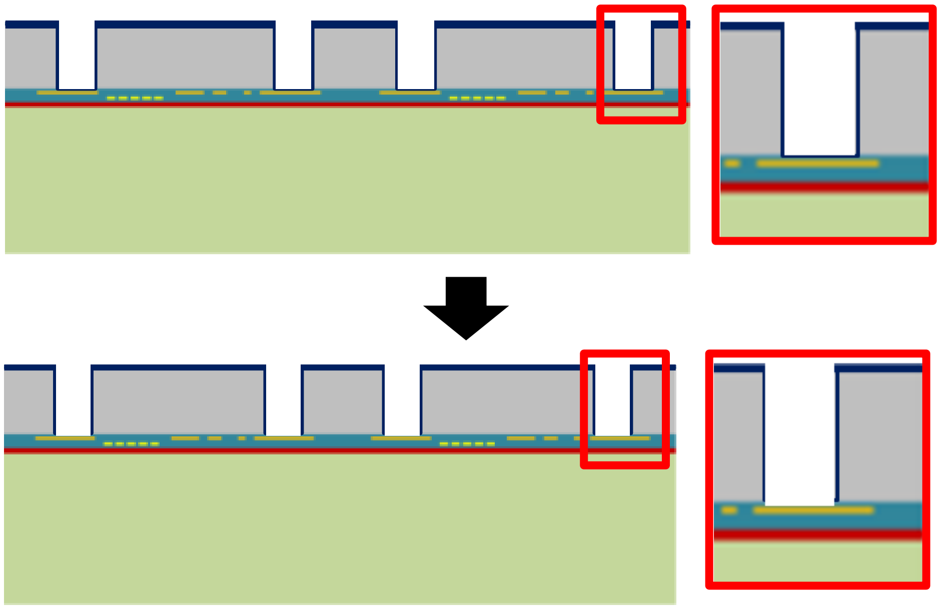

Figure 2. 13: Schematic picture of a CMOS wafer bonded to a handling wafer, before and after TSE. [Images provided by *ams AG*]

As mentioned earlier, precursor gases are used for both dry etching options.

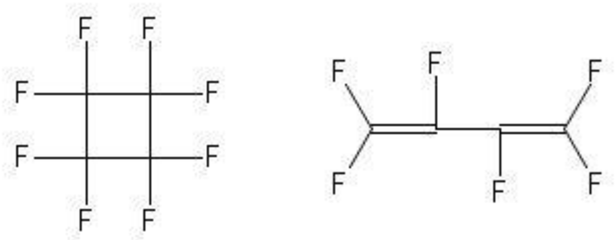

C_4F_8 **C_4F_6**

Figure 2. 14: Chemical structures of octafluorocyclobutane (C_4F_8) and hexafluoro-1, 3-butadiene (C_4F_6) gases.

Figure 2.14 illustrates the structural formula of the precursor gases used for DRIE (left molecule) and TSE (right molecule). C_4F_8 consists of single bonds while C_4F_6 contains C-F single bonds and C-C double bonds, thereby every node represents a carbon atom. The activation energy for the dissociation of the C=C (double) bond is five times lower than that of the C–C (single) bond. The double bond will break first and react with other components in the chamber, which in turn leads to more cross-linked connections.

2.5.3 Polymer Formation during TSE

Depending on the conditions in the plasma chamber, different kinds of deposition structures are possible [31]. The polymer surface structure affects the surface energy of the polymer, and therefore its wettability and the cleanability. High chain stiffness lowers the surface energy of an n[CF_2] polymer, while the same molecules in a cross-linked order have a higher surface energy, resulting in a better wettability.

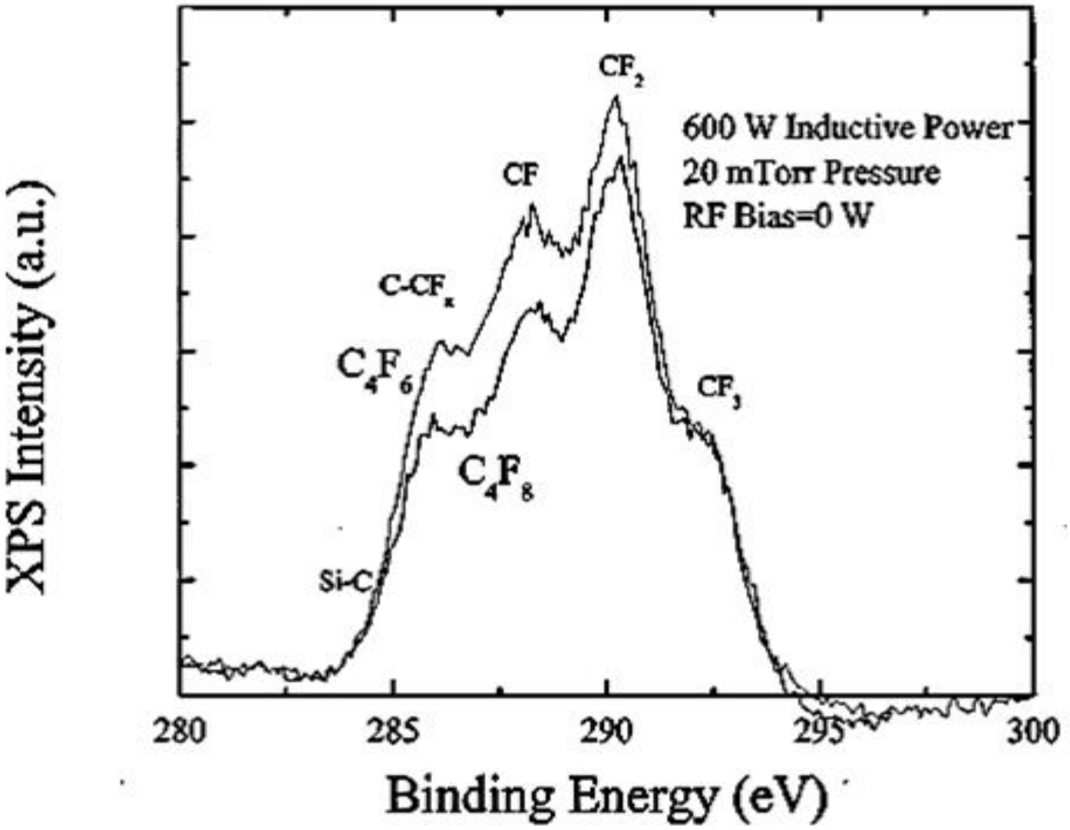

Figure 2. 15: X-ray-induced C(1s) photoelectron emission spectra obtained with passively-deposited fluorocarbon layers. The electrons were collected at 90 °. The samples were processed in 600 W inductive power, 20 mTorr pressure discharges fed with 40 sccm C_4F_8 and C_4F_6. [28]

In addition to affecting the structure of the polymer matrix, materials exposed to the plasma environment can be removed and embedded into the polymer matrix, thereby changing its wetting behaviour. During TSE, metal interconnects are exposed to the chamber environment. Released metal compounds can bind to the fluorocarbon polymer and create an organometallic compound. The main component of the remaining sidewall polymers after DRIE and TSE is CF_2 (Figure 2.15). This fluorocarbon polymer can be treated like a polytetrafluoroethylene (PTFE) polymer.

PTFE is a semi-crystalline polymer. It contains highly structured crystalline parts which are connected to each other via amorphous regions. Fluorocarbon polymers, like small-molecule fluorocarbons, exhibit increased thermal stability, hydrophobicity, lipophobicity, improved chemical resistance, and decreased intermolecular attractive forces. These properties are derived from the fundamental atomic properties of fluorine, which are high ionization potential, low polarizability, and high electronegativity.

Due to a very high electronegativity, C–F bonds are always strongly polarized. The strength of the C–F bond is high due to its ionic character, which accounts for the thermal stability of fluorocarbons. The high ionization potential of fluorocarbons, combined with their low polarizability, lead to weak intermolecular interactions, which in turn results in low surface energy and refractive indices. The low intermolecular forces in fluorinated polymers cause high contact angles with liquids. Water makes a contact angle of up to 112 ° with a fluorocarbon polymer surface [32], leading to non-wetting behaviour.

2.6 Residue Stripping

2.6.1 Polymer Wet Stripping Mechanism

The common polymer residue stripping process is explained using the example of a photoresist-removing procedure. The stripping process is similar to the developing process except that a much stronger alkaline medium must be used, due to the additional cross-linking that occurs under UV exposure. Typical resist strippers are based on either hydroxide or amine bases [33].

Photoresist films typically contain carboxylic acid groups (-COOH), which are converted to carboxylate ions (-COO-) by hydroxides (or amine). These ions are neutralized during the stripping processes.

Both reactions (2.12) and (2.13) follow the same general steps:

$$\mathrm{Na^+OH^- + R^1COOH \rightarrow R^1COO^-Na^+ + H_2O} \tag{2.12}$$

$$\mathrm{RNH_2 + R^1COOH \rightarrow R^1COO^- + RNH_3^+} \tag{2.13}$$

According to literature [33], the resist stripping mechanism follows four stages:

Diffusion/Swelling– Chemical Reaction

The alkaline stripping agent diffuses into the photoresist layer. This is the rate-determining step of the stripping reaction. The diffusion can be slowed by the hydrophobic surface or "crust" generated on the residue surface. The film begins to swell as it absorbs liquid.

Neutralization – Chemical Reaction

Carboxylic acid groups within the binding agents are neutralized to form soluble polar salts (see reaction 2.12 and 2.13), which further accelerate the diffusion of the solution into the film. Swelling is greatly enhanced due to the increased diffusion. Using an amine-based stripper, a nucleophilic reaction occurs, while the amine breaks the polymer into smaller, more soluble species.

Rupture – Mechanical Reaction

The presence of polar salts and water within the photoresist lead to an increase of internal stress and the film begins to physically rip itself apart. At this point the film begins to particulate and strip. The stress created by swelling causes rupture of the resist.

Lifting – Mechanical Reaction

The solution continues to penetrate the film as it ruptures, and also begins to attack the interface between the photoresist and the substrate surface. At this point the film lifts and becomes "stripped".

Although the chemical structure of the sidewall polymer differs from the photoresist, the four basic steps of the stripping mechanism can be used for the theoretical explanation of the post-TWE wet-cleaning process as well.

The removal of residue formed during the through silicon-oxide-spacer etching step takes almost twice as long as polymer residue stripping after DRIE. As mentioned previously, post-TWE and -TSE polymer residue stripping can be explained with the general four-step mechanism of the photoresist wet-stripping process. In both cases, the fluoropolymer residue is removed during a combined wet- and dry-cleaning process sequence. For the wet-cleaning part, an amine-based stripping agent comprised of monoethanolamine (MEA), hydroxylamine, pyrocatechol, and water is used. The main component with 50.0 – 60.0 % by weight is MEA, which generates hydroxides (OH^-) during reaction with water. Pyrocatechol is used to inhibit metal corrosion.

Monoethanolamine ($H_2N\text{-}CH_2\text{-}CH_2\text{-}OH$) is a weak amine, and therefore the content of hydroxides is low in aqueous solution. However, the equilibrium can be shifted to the right reaction side by subtracting the hydroxide (reaction 2.14).

$$\mathrm{R-NH_2 + H_2O \leftrightarrow R-NH_3^+ + OH^-} \qquad (2.14)$$

Besides delivering hydroxide ions, the monoethanolamine solution provides the corresponding ammonium ion, which supports complex formation of dissolved metal ions. Hydroxide ions created in reaction 2.14 reduce the hydroxylamine (NH_2OH) to its anion (reaction 2.15). The anion NH_2O^- is a strong nucleophile which can attack the carbonyl groups.

$$\mathrm{NH_2OH + OH^- \leftrightarrow NH_2O^- + H_2O} \qquad (2.15)$$

The result is an increased solubility of the reacted product (oxime) in an alkaline medium [34]. The anion also reduces metal-based residue such as organometallic species.

Pyrocatechol ($C_6H_6O_2$) is an aromatic 1, 2 diol which is used as a chelating agent, especially in basic conditions. Furthermore, it has a protecting function of metals used, particularly titanium. Nevertheless, there exists the possibility of corrosive occurring reactions between ionized water – caused by amine groups – and aluminium during the post through silicon-oxide-spacer etching clean.

The stripping agent displays a contact angle of 9.70 ° on a silicon wafer surface, which is similar to isopropyl alcohol (IPA). The contact angle has been determined using a Dataphysics OCA series contact angle measurement system. It should be considered that the water content during the measurement has not been determined. Adding water to the cleaning agent will likely increase the contact angle.
The dry-cleaning process is based on an oxygen plasma treatment. The plasma ash using oxygen is processed in a plasma chamber, where oxygen dissociates into ions and radicals as described in reaction equation 2.16.

$$O_2 + e^- \rightarrow O^+ + O^{\cdot} + 2e^- \qquad (2.16)$$

Oxygen radicals oxidize the hydrocarbon compounds on the surface, which leads to CO_x and H_2O formation. Oxidation of fluorocarbon generates compounds such as CO_x, COF_x and F_x. Consequently, the polymer is partially removed from the surface by oxidation. Additionally, the PTFE-like film layer is oxidized by replacing fluorine with oxygen in best case; as a result, the resist stripping agent is able to interact with the polymer surface.

The cleaning efficiency is not only determined by chemical reactions; fluid dynamics also significantly affect the cleaning process performance. According to literature, not all cleaning agents can successfully clean high-aspect-ratio submicron trenches. Infiltration in deep trenches depends on the surface properties of both the substrate and cleaning agent. Furthermore, parameters such as temperature and mechanical agitation are highly significant as well. These influencing factors are described in more detail in chapter 3.

TSV geometry, material properties, and the interface must be considered in order to improve the removal of the sidewall polymers after TSE.

2.6.2 Polymer Stripping by CO_2

Whether solid, gas, liquid, or above its critical point, the CO_2 found its way into the IC cleaning division. Beginning with solid CO_2 snow cleaning is able to remove particles of all sizes, from visible particles down to the 30-40-nanometre range. At the same time, this method removes thin films of surface organic contaminants (< 10 nm thick) [35], [36]. For particles larger than about 50 µm, CO_2 gas can be used, while a high-velocity CO_2 flow is guided over the contaminated specimen [37].

In addition to particle removal, CO_2 is also able to replace the conventional drying methods such as Marangoni drying [38] with isopropanol or acetone. CO_2 is capable of drying wafer surfaces as well as high-aspect ratio structures on the wafer [39]. Due to the capillary force of water-based cleaning agents, sensitive structures can collapse. Therefore, during the drying process, CO_2 in its supercritical state is used to displace water without causing, for example, the collapse of photoresist patterns [40].

Over the last decade, $scCO_2$ has been discussed more frequently as a wafer-surface cleaning agent in the advanced semiconductor industry [41]. $ScCO_2$ is capable of removing residue and submicron particle contaminants remaining on wafer surfaces with nanometre-sized features [42], [43].

As the feature size of integrated circuits decreases, transport of cleaning agents into and out of the vias and trenches becomes more difficult. Reasons for this include the relatively high surface tension of conventional water-based cleaning agents and the wetting problems on polymeric residue that build up a high contact angle, among other reasons. These difficulties make a solvent like $scCO_{2,}$ with a surface tension of nearly zero that enables it to penetrate every arbitrarily small-sized structure, even more attractive as an alternative for certain wet-cleaning processes. Several patents were applied for on the subject of photoresist stripping and residue removal from the wafer substrate. $ScCO_2$ function as a transport medium for such co-solvents as fluorinated solvents, alcohols, hydrocarbons, ethers, ketones, and amines, among others [44]. There are methods described for cleaning procedures that use only the CO_2 in liquid and supercritical states. Depending on the contamination, pressure and temperature in the chamber are variated and additional agitation in the form of a magnetically coupled paddle stirrer is used [45].

2.7 Cleaning Tools

A number of cleaning tool types are suitable for TSV cleaning. Single-wafer cleaner and batch cleaner differ in features such as throughput, cleaning time, results in cleanliness and volume of cleaning agent.

Single-wafer cleaners dispense the cleaning agent on the wafer using a nozzle. A heating step follows, which can be supported by megasonic agitation. The stripping time depends on the stripping agent and the process temperature, among other parameters. To illustrate, an amine-based 70-80 °C warm solvent needs more than half an hour for resist stripping. After the resist polymer is stripped, a deionized water (DIW) rinsing is performed to remove stripped residue from the wafer surface and trenches. This step is usually done while the wafer is rotating, which leads to a spin-off effect of the dispensed DIW plus stripped residue. The last step is the drying of the wafer surface. This can be done by heating or dispensing highly volatile agents such as IPA. The latter agent makes use of its surface tension characteristic. The fluid with the smaller surface tension displaces the fluid with higher surface tension, a process also known as Marangoni effect. The remaining fluid dissipates from the surface because of its high vapour pressure.

Batch cleaning is another more common method of cleaning applied in the semiconductor industry. The advantage of this process is a relatively large throughput. A cassette with about 25 wafers is fully submerged in the heated (depending on the cleaning agent) stripping agent. At this step, cleaning efficiency can be mechanically supported by megasonic agitation. The cleaning is complete after a DIW and drying step.

Chapter 3 Theoretical Principles

This chapter is divided in sections 3.1 and 3.2. Section 3.1 covers an introduction in the newly-developed TSV inspection method, basic CO_2 properties, behaviour of CO_2 as a solvent, and a transport and diffusion medium. Furthermore, polymer swelling on the basis of CO_2 diffusion inside the polymer matrix is explained and illustrated with an example. Moreover, the fluorophore ATTO 647N is introduced as the selected fluorophore and its solubility in CO_2 is discussed. Using this fluorophore, the settings for the confocal laser scanning microscope (CLSM) are defined. Section 3.2 covers an introduction in the wetting behaviour of smooth and rough surfaces and the corresponding models and assumptions due to trapped air in trenches causing an infiltration inhibition. In addition, this chapter includes a description of the newly-developed infiltration evaluation method for liquids with different surface tensions and hydrophilic and hydrophobic trench surfaces with different aspect ratios. This chapter ends with a discussion about the effects of hydrofluoric acid on the polymer-trench-sidewall interface.

3.1 Development of an Innovative TSV Inspection Method

To circumvent the drawbacks of destructive analysis methods and to provide an efficient and reproducible procedure to detect polymer residue on the wafer-level, a novel optical detection method was developed. The diagram below (Figure 3.1) represents the general process flow of sample preparation for subsequent inspection under a CLSM. First, a fluorophore is dissolved in supercritical CO_2 ($scCO_2$). Under pressure, the polymer residue is impregnated with this fluorophore/$scCO_2$ mixture. After depressurizing, the carbon dioxide escapes, while the fluorophore remains inside the polymer matrix. These steps are explained in detail in the following sections.

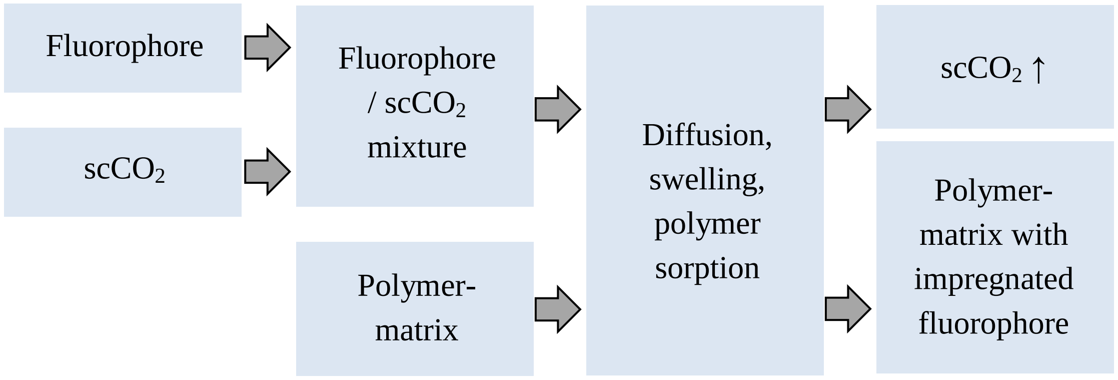

Figure 3. 1: Sample preparation process flow.

After labelling, the fluorophore-impregnated polymer matrix is observed under the CLSM. During observation, the polymer matrix with the incorporated fluorophore is excited by a laser beam. The fluorophore emits fluorescent light which can be detected by the microscope, generating an image of the scanned sample surface. Figure 3.2 depicts a back-grinded CMOS wafer bonded to a handling wafer, comprised of four TSVs; polymer residue is implied inside one of these TSVs. The red cone represents the excitation of the fluorophores inside the polymer by a laser beam. The excitation parameters as well as proper settings for detection are described in detail following this chapter.

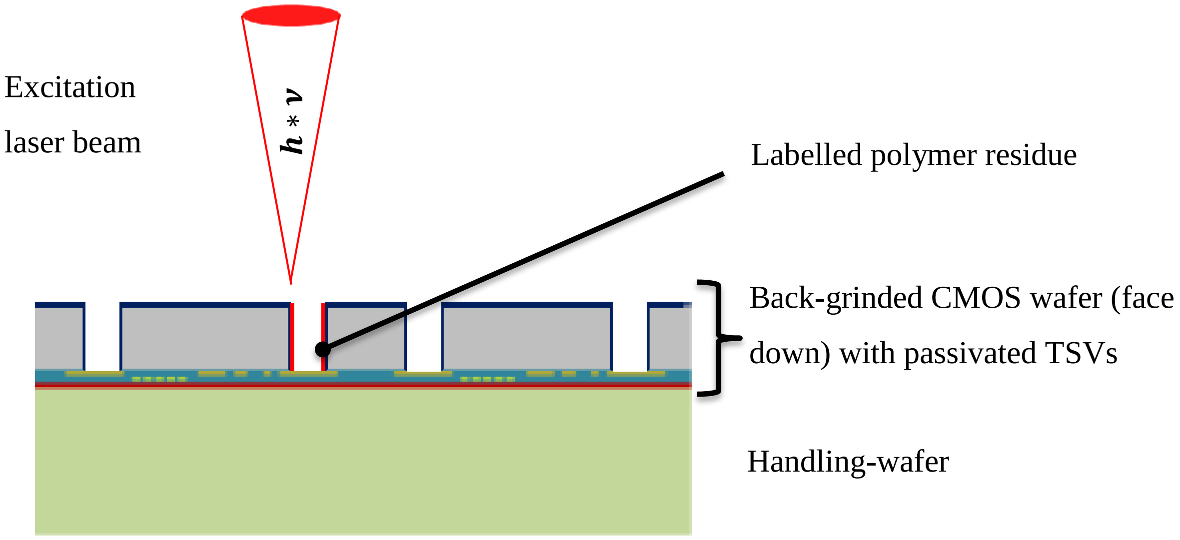

Figure 3. 2: Schematic representation of labelled polymer during excitation. [CMOS image provided by *ams AG*]

Since this labelling method is based on impregnation of a polymer matrix using fluorophores, a transport medium for the fluorophore is needed. The transport medium in this case should fulfil the following requirements:

- Dissolve the fluorophore
- Diffuse into the polymer matrix
- Maintain chemical inert status.

CO_2 meets these requirements and demonstrates certain additional benefits for the impregnation procedure. Because of its extraordinary solvent properties, CO_2 (in its supercritical state) has been applied in extraction and fractionation processes, such as decaffeination of coffee and tea [46], polymerization of polymers [47], and cleaning in semiconductor manufacturing technology [48]. As already mentioned in chapter 2, CO_2 is applied for certain wafer-cleaning process steps such as wafer drying and particle removal.

During the extraction process, $scCO_2$ diffuses into the solid matrix, solvates the organic substance, and removes it from the matrix. From a technological point of view, the impregnation process is basically the inverse process of an extraction. In general, the impregnation procedure involves three steps. First, the fluorophore is blended with the transport medium CO_2. The second step involves the transportation of the fluorophore-CO_2 mixture to the polymer surface; this second step is followed by the third, in which the mixture is diffused into the sidewall polymer. After decompression CO_2 escapes, while the fluorophore is captured in the polymer matrix. This fluorophore can then be detected with a fluorescence microscope. For a successful impregnation, material properties and interactions between the used components and the sample substrate must be considered and optimized.

3.1.1 CO_2 Properties and Carrier Abilities

CO_2 is a nontoxic, odourless, colourless, non-flammable, non-corrosive, chemically inert and recyclable gas. According to these properties, chemical reactions with the substrates can be excluded. CO_2 is available on the market in different degrees of purity; its molecule is inert in most environments and has no dipole moment. However, it is a Lewis acid and reacts with strong bases.

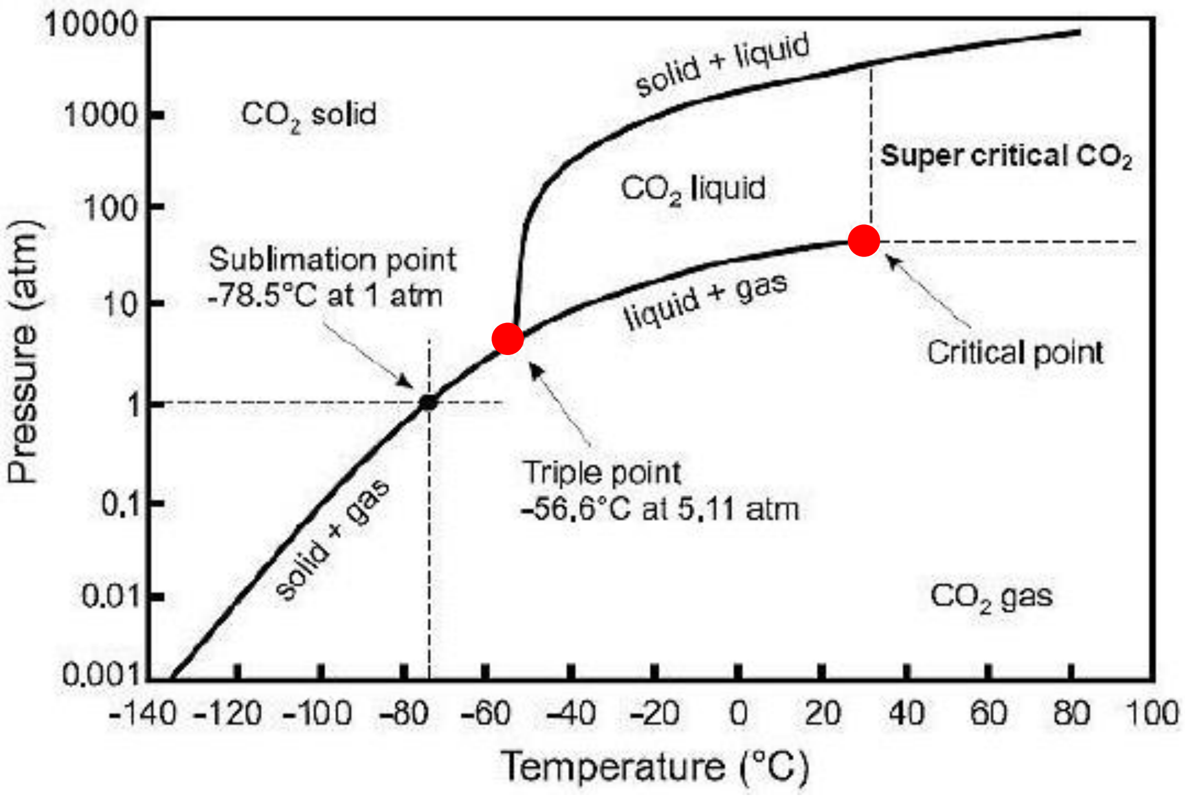

Figure 3. 3: CO_2 phase diagram showing areas of solid, liquid, gaseous, and supercritical CO_2. Red points highlight the triple point and critical point. [49]

Figure 3.3 depicts the phase diagram of CO_2 [49]. The two most important points with respect to the change in phase, i.e., the triple point and the critical point, are highlighted with red circles. The triple point resembles the point at which all three phase boundaries meet. At this temperature and pressure, all three phases – solid, liquid and gaseous – are in equilibrium. The physical appearance of CO_2 at this point can be observed in Figure 3.4a. Even more important is the critical point, representing the highest temperature and pressure at which the substance can exist as a vapour and liquid in equilibrium.

This phenomenon can be observed when the boundary layer between liquid and gas is disappearing, which can be seen in Figure 3.4b, where a foggy line in the middle of the chamber cylinder is dividing liquid and gaseous CO_2. Near its ambient critical temperature Tc (Tc of 30.98 °C), CO_2 has a low viscosity and high diffusivity compared to liquids [50]. Above this point, CO_2 turns into a supercritical fluid.

CO_2 transforms into its supercritical state at a relatively low pressure and temperature compared to other supercritical fluids (such as supercritical water), with a critical point at a temperature of 374 °C and a pressure of 218 bar. Above the critical point, CO_2 displays highly beneficial physico-chemical properties with regards to its application in extraction and impregnation processes. One of these beneficial properties is the density, which is comparable to those of conventional solvents, but which has increased dissolving capacity for many organic substances.

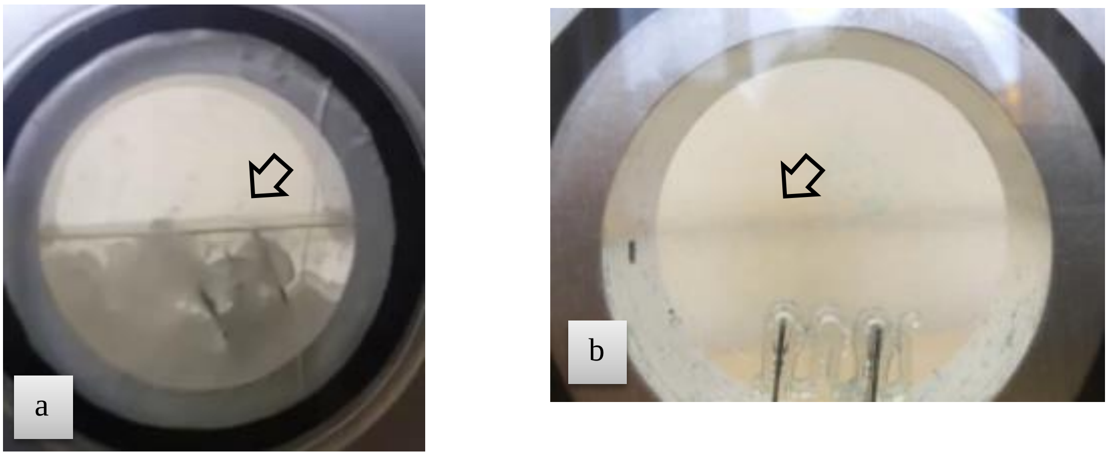

Figure 3. 4: CO_2 near the triple point with solid, liquid and gaseous phase coexisting in equilibrium (a) and near the super critical state with a disappearing phase boarder between liquid and gaseous phase (b).

In Table 3.1, properties of different physical states of CO_2 are listed [51]. In its supercritical state, CO_2 exhibits a liquid-like density and gas-like viscosity and diffusivity. The diffusivity of $scCO_2$ is about 10 - 100 times higher than that of liquid CO_2; the viscosity of a $scCO_2$ is also comparable to that of a gaseous CO_2. Lower viscosity and density make circulation of the dye solution easier, and considerably increase the solvating power. Because of the absence of surface tension and the miscibility of air with CO_2 under pressure, the solution will infiltrate any arbitrarily small trench very fast. Besides a negligibly small surface tension, $scCO_2$ demonstrates lipophilic solvent behaviour, which enables it to dissolve nonpolar substances. Moreover, $scCO_2$ has the advantage that its solvating power is adjustable and can be set to values ranging from gas-like to liquid-like.

Table 3. 1: Physical properties comparison of CO_2 at three different aggregate states. [51]

Aggregate state	**Density [kgm^{-3}]**	**Diffusivity [mm^{2}s^{-1}]**	**Viscosity [µPas]**
Gases	1	1-10	10
Liquids	1000	0.001	500-1000
Supercritical Fluids	100-1000	0.01-0.1	50-100

Two impregnation rate determining steps are related to the CO_2 properties:

- Dissolving capacity in relation to the fluorophore
- Diffusivity regarding the polymer matrix.

3.1.2 CO_2 Solvation and Transport Properties

For a successful impregnation, the fluorophore must firstly be sufficiently soluble in the supercritical fluid. In general, liquid as well as $scCO_2$ can dissolve a number of low molecular compounds and small aromatic hydrocarbons. CO_2 as a solvent follows the general principle “similia similibus solvuntur” [52] (similar is solved by similar), thus proving to be a good solvent for many non-polar dyes. However, water-soluble polar dyes such as acidic dyes and reactive dyes do not dissolve in nonpolar $scCO_2$. Since dissolving power is directly related to the density of the solvent, it can be increased by raising pressure. This can be explained with enhanced interaction forces between molecules of the solute and the solvent. Therefore, solubility of all type of dyes increases with the increasing pressure of CO_2. As a result, the solubility behaviour is mainly governed by the physical interactions between CO_2 and the dye molecules. In addition to impregnation, CO_2 is also used as a solvent in fibre-dyeing processes and polymerization (also fluoropolymers) [53].

3.1.3 CO_2 Diffusion Properties

After the fluorophore solution reaches the polymer, the solute must diffuse into the matrix. As mentioned in chapter 2, the polymer matrix consists of a semi-crystalline fluoropolymer. Semi-crystalline polymers are composed of long molecular chains, which display a short-range order, while in adjacent regions the polymer chains are irregularly tangled and possess no order at all. Thus, these polymers simultaneously have both crystalline and amorphous areas. It has been determined that certain amorphous fluoropolymers and silicones display good solubility in pure CO_2, since CO_2 can easily penetrate the amorphous domains of the polymer. Especially fluorinated polymers have affinity to CO_2 [54]. The diffusion coefficient increases with increasing CO_2 pressure, which can be attributed to the swelling of the polymer.

3.1.4 Polymer Swelling

Studies on CO_2-induced swelling of PTFE and amorphous-based sorption exhibit a direct dependency between the degree of swelling and the CO_2 pressure. Table 3.2 presents swelling data as a percentage for PTFE, measured as a function of temperature and CO_2 pressure [55]. As can be observed in this figure, the swelling is less than 8 % for all temperature and pressure combinations, which is a consequence of the high polymer crystallinity. High crystallinity reduces the mobility of the solvent molecules, which is amplified by a high molecular weight of the polymer.

Table 3. 2: Experimental values of CO_2-induced swelling of PTFE at different temperatures. [55]

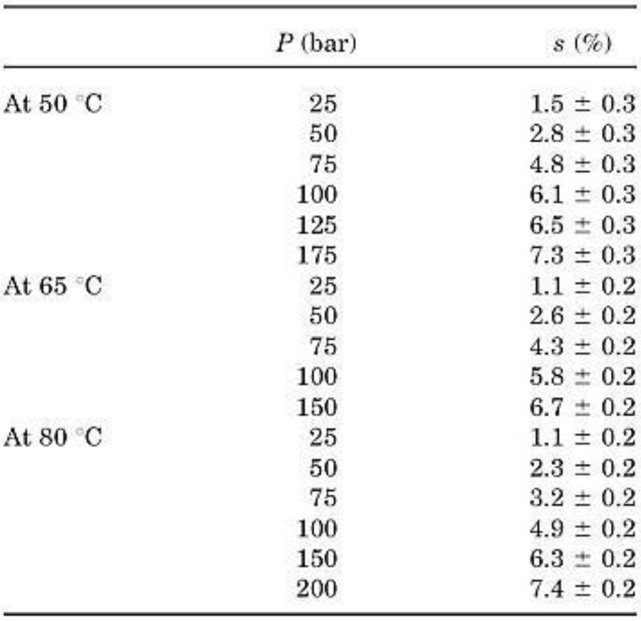

	P (bar)	s (%)
At 50 °C	25	1.5 ± 0.3
	50	2.8 ± 0.3
	75	4.8 ± 0.3
	100	6.1 ± 0.3
	125	6.5 ± 0.3
	175	7.3 ± 0.3
At 65 °C	25	1.1 ± 0.2
	50	2.6 ± 0.2
	75	4.3 ± 0.2
	100	5.8 ± 0.2
	150	6.7 ± 0.2
At 80 °C	25	1.1 ± 0.2
	50	2.3 ± 0.2
	75	3.2 ± 0.2
	100	4.9 ± 0.2
	150	6.3 ± 0.2
	200	7.4 ± 0.2

In their study, Jiménez et al. determined the weight change of different polymer types after treatment with CO_2 followed by degassing (Figure 3.5). The results presented in Figure 3.5 confirm that amorphous polymers are more inclined to absorb CO_2 than polymers with high crystallinity, because their small molecular orientation provides free volume content in their inter-molecular space [55]. Absorption of CO_2 by the polymer causes it to swell slightly, leading to faster diffusion within the polymer.

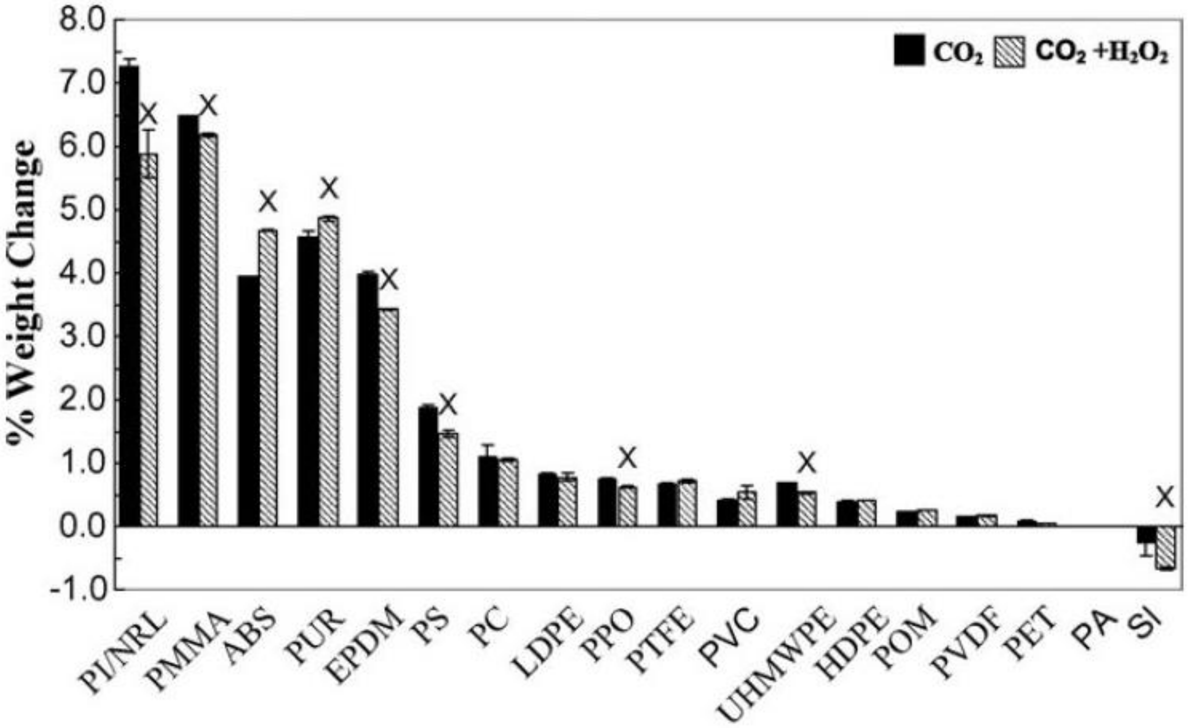

Figure 3. 5: Weight change due to uptake of CO_2 in the specimens. PTFE weight change of approximately 1% after CO_2 absorption is depicted as the black bar. [55]

3.1.5 Photoresist after CO_2 Treatment

In preliminary experiments, the effects of liquid and scCO_2 treatment of samples covered with photoresist are examined. Optical microscope images depicted in Figure 3.6 indicate a deformation of the photoresist layer after treatment with supercritical and liquid CO_2, respectively.

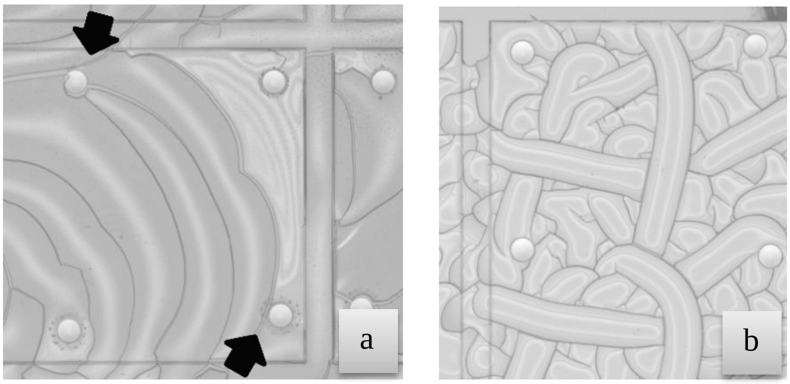

Figure 3. 6: Liquid CO_2 treated photoresist (a) and scCO_2 treated photoresist (b).

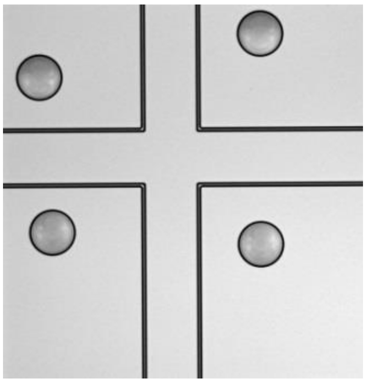

Figure 3. 7: Wafer specimen with a photoresist layer on the surface.

When comparing an untreated wafer specimen covered with photoresist as illustrated in Figure 3.7 with a CO_2-treated surface (Figure 3.6), it can be easily recognized that the photoresist has changed optically. With scCO_2, the photoresist forms bead-like structures (as illustrated in Figure 3.6b), whereas with liquid CO_2, the photoresist seems to crack into arcuate curves (see Figure 3.6a). The material tension is responsible for these formations. The tension in the photoresist polymer can be explained by the diffusion of CO_2 into the polymer matrix, causing the material to swell and hence initiating cracks and bulges. The sample treated with CO_2 in its liquid phase also demonstrates that the resist prefers to crack in certain areas, especially around particular TSVs (marked with black arrows).

3.1.6 Fluorophore-CO_2 Solubility

For the new polymer detection method presented in this thesis, a fluorophore must be dissolved in CO_2, as explained in chapter 1. It is therefore important to choose a fluorophore which is soluble in CO_2 and possesses good fluorescence characteristics. The fluorophore used in this work (ATTO 647N) is functionalized with carboxyl groups (–COOH), making it lipophilic, hydrophobic, and partially water soluble. The fluorophore molecule contains several combined non-polar aromatic groups, which are responsible for the fluorescence of the molecule. As mentioned in the previous sections, non-polar components are soluble in liquid and $scCO_2$; therefore, the first requirement of the labelling process (dissolving the fluorophore) is fulfilled. Before being blended in $scCO_2$, ATTO 647N is dissolved in deionized water. Since CO_2 has a small mutual solubility in water, CO_2 will dissolve the fluorophore stepwise. The convection inside the DIW-ATTO 647N drop transports the fluorophore particles at the interface, maintaining permanent contact to CO_2.

3.1.7 CLSM Settings

As mentioned at the beginning of this chapter, the image is formed by area-scanning of the focused laser beam. A helium-neon laser excites the fluorophore in a red spectral area of 633 nm. Photobleaching is an effect which occurs when the intensity of the excitation source is set too high; therefore, in the beginning of the analysis, the laser power is set to 15 % to avoid fast photobleaching. The matching fluorophore for this laser is a fluorophore with the trade name ATTO 647N with an absorption wavelength of 647 nm.

The ATTO 647N fluorophore emits fluorescent light in the red spectral region at a wavelength of 669 nm. Further characteristic features of ATTO 647N include strong absorption behaviour (extinction coefficient of 1.5×10^5), a high-fluorescence quantum yield, and high thermal- and photo-stability. The relatively high quantum yield η_{fl} of 65 % (Table 3.3) enables the detection of fluorescence intensity even at low concentrations of the dye. This makes the fluorophore particularly suitable for high resolution microscopy, allowing for single-molecule detection. The Stokes shift of 22 nm enables an appropriate differentiation between possible reflected emission light from the sample and the emitted fluorescent light.

Table 3. 3: Optical properties ATTO 647N with absorption wavelength λ_{abs}, emission wavelength λ_{fl}, extinction coefficient ε_{max}, quantum yield η_{fl} and fluorescence lifetime τ_{fl}.

<table>
<tr><th colspan="3">ATTO 647N</th><td rowspan="7">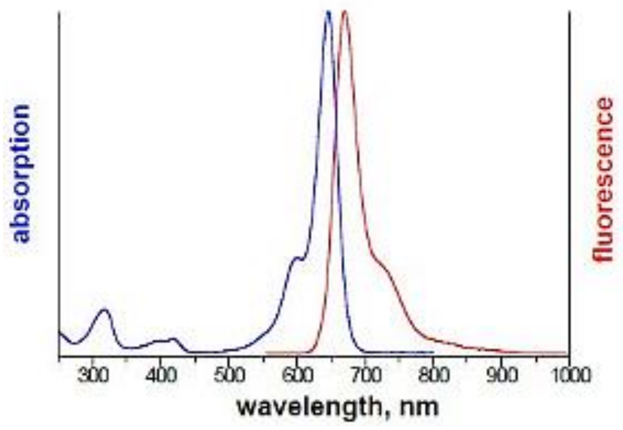
</td></tr>
<tr><td>Formula weight</td><td>[g/mol]</td><td>746</td></tr>
<tr><td>λ_{abs}</td><td>[nm]</td><td>646</td></tr>
<tr><td>ε_{max}</td><td>[l/mol cm]</td><td>1.5 E5</td></tr>
<tr><td>λ_{fl}</td><td>[nm]</td><td>664</td></tr>
<tr><td>η_{fl}</td><td>[%]</td><td>65</td></tr>
<tr><td>τ_{fl}</td><td>[ns]</td><td>3.5</td></tr>
</table>

A precise detection of the labelled polymer on the TSV sidewall is dependent on a high spatial resolution of the microscope. As mentioned in the beginning of this chapter, the resolution can be increased by a number of settings. Beginning with the objective, in this case either a dry objective or an objective immersed in oil can be used. Oil as an immersion medium has a similar refractive index to PTFE (n_{PTFE} of 1.38 [56]), which closely resembles the molecular composition of the embedding matrix (sidewall polymer). Equal refractive indices of the matrix and the immersion medium reduce the diffraction of the light, leading to a higher amount of light collected by the objective.

Table 3.4 compares the NA of a dry objective and the NA of the same objective when using oil as an imaging medium. With the application of the immersion technique, the NA of the objective can be increased from 0.3 to 1.44, thereby increasing the resolution.

Table 3. 4: Numerical aperture (NA) of dry and oil objectives.

Dry objective	**Oil objective**
$\mathrm{NA}_{\mathrm{max}} = 0.3$	$\mathrm{NA}_{\mathrm{max}} = 1.44$

It is necessary to ensure that the excitation and the emission wavelength range, which pass the AOBS in detector direction, do not overlap; otherwise, the excitation light will be counted as fluorescence and the detector will be overloaded.

One of the most important CLSM settings is the pinhole size, as it enables a vertical imaging of the sample. In the beginning of the sample inspection under the CLSM, the pinhole aperture size should be set to a wider value (e.g., half of the total possible diameter size of the pinhole), to allow as much fluorescent light as possible to pass through. It is advisable to increase the pinhole size until fluorescent spots are detected. In parallel to the pinhole size, the smart gain is increased until a signal can be seen on the screen. To set proper acquisition parameters, the *Quick Look Up Table* (QLUT) support (provided by the CLSM corresponding Software) is selected, which helps adjust the optimum brightness. The live image generated in this mode displays pixel intensity, scaling at bit depth setting 12 (on a scale ranging from 0 to 4065). Varying only in their shades of grey, pixels can also be displayed in blue (saturation) and green (zero). Blue pixels are an indication of overexposure of the sample, whereas green pixels imply underexposure.

The *smart gain* control wheel regulates the brightness of the image. Depending on the strength of the signal the gain ranges between 700 and 1100 V. Adjusting the *smart gain* (not available for HyD detectors) until there are very few blue pixels in the image and reducing the pinhole size to the default setting of 1 Airy unit increases the resolution in the vertical axis, due to a reduction of out-of-focus light. Subsequently, the focus is set using the z-position knob.

If the signal intensity is very low, it can be increased by adjusting the gain settings or increasing the laser power. Higher gain settings will brighten the image without photobleaching the specimen but also generate more noise. This can be compensated by signal averaging, while application of high laser energy is prone to cause increased bleaching of the fluorophore. Not only a direct change in illumination power will enhance the photobleaching, however; with increasing zoom factors, the same laser energy exposes a raster of smaller area.

For fluorescence signal detection in the red spectral region, the HyD4 detector is selected. This detector can be used in standard mode, brightR mode, and photon-counting mode. The standard mode is suitable for most applications and was used for most of the inspection experiments of this thesis as well. It also can be used for poorly-dyed samples. This mode is usually used for image acquisition.

If samples have a large dynamic range, which means that very bright and very faint areas are present on the same image, the brightR mode enhances the lower-intensity pixels without affecting the higher-intensity pixels. Enhancing the signal of the lower-intensity pixels generates better image quality, but cannot be applied on images used for quantitative analysis. For quantitative analysis, the photon-counting mode is employed. This mode counts all the photons that hit the detector in a particular location as a function of time, and creates an image by accumulation of the photon counts. Every photon of the fluorescence emission will be detected and counted without signal amplification. Because of the low fluorescence signal intensities and the fact that the detector is counting the photo-electron and not amplifying it, the image contrast is very low and appears very dim. The low background noise of the HyD photon-counting allows as much information as needed to be accumulated for any statistical analysis. For high bit depths (12 bit; 4096 photons forming one pixel), an enormous dynamic range with very low statistical per-pixel variance is available. The photon numbers are displayed via a look-up-table (LUT) on the screen. In this case, the physical equivalent to the colours are the photons.

The resolution of an optical microscope is defined as the shortest distance between two points that can still be distinguished by the observer. Table 3.5 lists the calculated resolutions of a dry and an oil immersion objective used in this thesis. As the table indicates, the oil immersion objective offers much better lateral and axial resolutions in comparison to the dry objective.

Table 3. 5: Comparison of dry and oil objective and the corresponding calculated lateral and axial resolution.

Dry objective	**Oil objective**
$\text{Resolution}_{\text{lateral}} \approx 780\text{ nm}$	$\text{Resolution}_{\text{lateral}} \approx 162\text{ nm}$
$\text{Resolution}_{\text{axial}} \approx 8795\text{ nm}$	$\text{Resolution}_{\text{axial}} \approx 384\text{ nm}$

There are several possibilities to increase the resolution of a 512x512 (9 bit) image. Increasing the digitizer resolution to 1024x1024 (10 bit) is a common method, but with the increased resolution, image recording time also increases. Usually the image quality will be enhanced, but it also becomes somewhat grainy. To compensate for the image noise, line averaging can be implemented. During line averaging, a previously-set number of scans are taken from the same line, before proceeding with the next line scan. This is repeated for all lines in a frame. The image becomes less noisy and pixilation effects are eliminated. In live imaging mode, 4 - 8 line averages can be selected, which results in sufficient image quality for first adjustments. A low number of line averages avoids fast bleaching of the sample and offers screen refresh rates that are fast enough to display setting changes made while recording. After setting optimization in live image view, the line averaging is changed to higher value, which will result in a higher image quality. For qualitative analysis, image capturing at an averaging number of 32 - 96 is recommended.

Using frame average instead of line average mode speeds up the image processing, but also generates higher noise. With respect to the image quality, an averaging setting of 8 has been determined as the optimum value for images in 512x512 or 1024x1024 format recorded at 400 Hz scanning speed. However, a higher resolution image in combination with higher scanning speed requires more averaging iterations; this increase in turn will induce severe bleaching with additional noise. In certain situations, it is difficult to adjust the image so that it has a sufficient resolution while it simultaneously avoids bleaching too quickly; in this case, the line average and frame accumulation can be combined. This combination reduces noise, increases signal intensity, increases signal-to-noise ratio, and improves image quality. However, the additional frame-accumulation step consumes extra inspection time. The following table (Table 3.6) summarizes how different parameters affect the intensity and the spatial resolution of the image. If the parameter is set higher, the intensity and spatial resolution will increase (+) or decrease (-).

Table 3. 6: Parameter settings and their corresponding influence on signal intensity and spatial resolution.

Parameter	Intensity	Spatial resolution	Comment
Pinhole size	+	-	
Zoom	+	+	
Scan Rate	-	-	Temporal resolution
Objective NA	+	+	
Laser Power	+	+	Photo-bleaching

3.2 Wet Cleaning

The first step towards the development of a new cleaning method is to closely examine the physico-chemical properties, such as the wetting behaviour of the specimen material. The development of innovative technologies and processes (ever-decreasing TSV sizes and -increasing TSV aspect ratios) resulting in added properties of the material behaviour leads to new challenges for the cleaning procedure. Therefore, more adapted surface characterisation methods such as the infiltration evaluation method must first be developed.

3.2.1 Wetting Behaviour

TSV formation via DRIE makes use of fluoropolymer deposition to generate deep features with exceptional anisotropy and high etch rates. Polymer residue remaining on via sidewalls potentially cause an inhibition or delamination of subsequently deposited layers, increasing thermal stress and resulting in a reduced device yield. Consequently, it is of paramount importance to guarantee a complete removal of the polymer residue. Typically, post-DRIE residue stripping processes consist of a plasma ash and a wet-cleaning sequence.

An incomplete removal of the polymer remnants can have manifold reasons:

- Cleaning solvent or stripping agent incompatibility
- Disadvantageous cleaning process parameters or cleaning sequence (temperature, agitation, and time, among others)
- TSV structure size

Fundamentally, for a successful wet cleaning, the stripping agent has to wet the polymer residue completely. Lack of infiltration and incomplete wetting of the surface to be cleaned can be a reason for residue remaining on the sidewalls. The wetting behaviour of a polymer is depending on the properties of the polymer material itself and the cleaning agent used, as well as the interaction between them.

The most common way to characterize the wetting behaviour of a surface is to measure the contact angle θ. As indicated in Figure 3.8, wetting can be divided in three categories: good wetting behaviour with a contact angle of less than 90 °, poor wetting with a contact angle of approximately 90 °, and no wetting with a contact angle of greater than 90 ° [57].

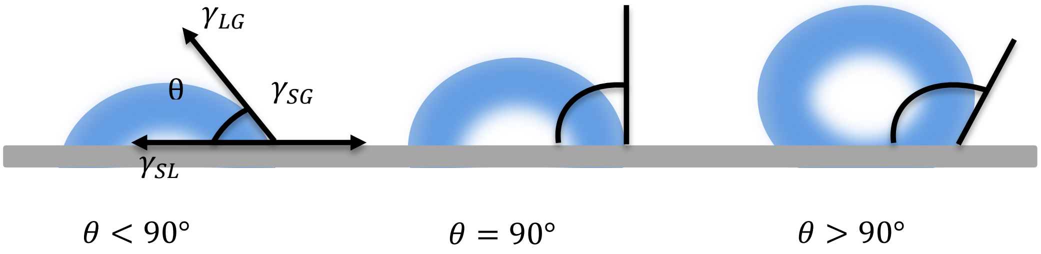

Figure 3. 8: Contact angle with corresponding wetting properties. [57]

The contact angle can be calculated by different models and equations. The simplest equation, i.e., the Young equation (3.1) [57], describes wetting of an ideal smooth, solid, and chemically homogeneous surface.

$$\cos \theta_{\gamma} = \frac{\gamma_{SG} - \gamma_{SL}}{\gamma_{LG}} \tag{3.1}$$

$\gamma_{SG}, \gamma_{SL}, \gamma_{LG},$ stand for the surface energies at the following corresponding interfaces: solid and gas, solid and liquid, liquid and gas and θ_{γ} the intrinsic (ideal) contact angle. The equation is valid only for three-phase systems of ideal solids and pure liquids in their thermodynamic equilibrium. All models for determination of the surface free energy of solids by means of contact angle measurements are based on this equation. In contrast to ideal surfaces, real surfaces are not perfectly smooth and chemically homogenous.

The relationship between non-ideal, rough surfaces and their wettability was described by Wenzel (3.2). The Wenzel model extends Young's equation and introduces the influence of the surface roughness by adding the roughness ratio r_W (ratio between the actual and projected solid surface area) [57]. Therefore the contact angle on rough surfaces θ_W is calculated as follows:

$$\cos \theta_W = r_W \cos \theta_Y. \tag{3.2}$$

In cases where not all grooves will be penetrated by the liquid, this model will not apply. In order to describe the additional influence of various materials on the apparent change of the contact angle, a further extension of the Wenzel model is needed.

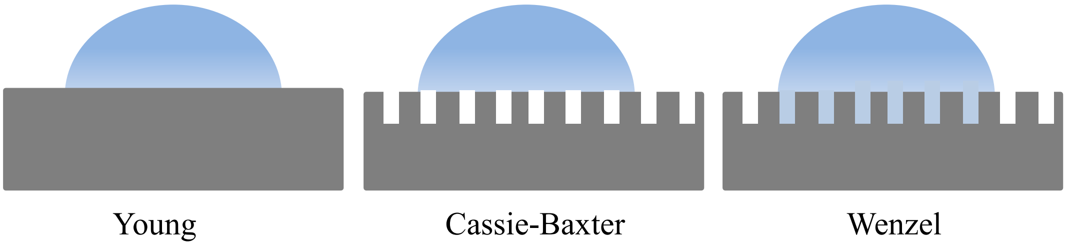

Figure 3. 9: Schematic illustration of different wetting regimes: Young's model, Wenzel model, and Cassie-Baxter model [Wikipedia].

This additional extension by Cassie-Baxter describes the wetting behaviour of a rough, chemically-heterogeneous surface. Figure 3.9 schematically illustrates the different wetting regimes according to Young (smooth surface), Wenzel (rough surface), and Cassie-Baxter (super hydrophobic surface).

Table 3. 7: Contact angle θ of water on smooth and rough surfaces.

Test Liquid	**Surface**	**Θ [°]** **Smooth surface**	**Θ [°]** **Rough surface**
Water	PTFE	128[3] [58]	151[4] [58]
Water	SiO_2	52[5] [59]	<5 [60]

---

[3] Smooth surface; RMS surface roughness of 5.6 µm

[4] Rough surface; RMS roughness of 16.3 µm

[5] Smooth surface; RMS surface roughness of 0.17 nm

Most polymers exhibit poor wetting behaviour by aqueous solutions, especially PTFE, which forms a water contact angle of approximately 120 °. The different surface properties of PTFE and SiO_2 are depicted in Table 3.7, indicating that a drop of water will spread to a thin film on a SiO_2 surface, while on a PTFE surface it will maintain its spherical shape. Furthermore, the data highlights the effect that the surface roughness has on the hydrophobicity (as can be seen for PTFE) and hydrophilicity of a surface. Surfaces forming a water contact angle above 150 ° are referred to as super hydrophobic.

3.2.2 Trapped Air in Trenches

Roughening or structuring leads to an increased surface area; this increase enhances the hydrophilicity or hydrophobicity. However, the air trapped inside the structure has a significant effect on the wettability of a substrate surface.

Firstly, complete wetting of a high-aspect-ratio structure (trenches or holes) is directly related to the replacement of trapped air in the total volume of the structural element. Secondly, the wetting is affected by the surface tension of the materials used. Hydrophilic surfaces tend to be wetted easier by polar liquids than hydrophobic ones. On the one hand, roughness of hydrophilic surfaces facilitates spreading of polar liquids, because of the increased surface; on the other hand, the liquid will have to flow along the sidewalls, undercutting the trapped air. During undercutting, a new surface between the fluid and the vapour is formed. If the surface of a liquid needs to be increased, a certain quantity of work (W) is required. This amount of work depends on the TSV area (A) and the surface tension (σ) of the liquid used (3.3). In this case, the adhesive power between SiO_2 and water must be higher than 0.88×10^{-8}J to wet one TSV.

$$\sigma_{\mathrm{Water}}^{20^\circ\mathrm{C}} = \frac{\mathrm{dW}}{\mathrm{dA}} \tag{3.3}$$

$$\mathrm{W} = 72.75\ \frac{\mathrm{mN}}{\mathrm{m}} * (2\mathrm{r}\pi\mathrm{h} + \pi\mathrm{r}^2) = 0.88 \times 10^{-8}\ \mathrm{J}$$

In contrast to hydrophilic surfaces which attract water, the hydrophobic surfaces act water-repellent. As a consequence, the quantity of work for increasing the surface of the liquid must be supported with additional force; this increase in force can be accomplished, for example, by increasing pressure.

However, it is possible to transition from the Cassie-Baxter wetting state into the Wenzel state. It is assumed that a drop is placed on a structured surface filled with air. If the captured air is not thermodynamically stable, liquid will nucleate from the centre of the drop. For destabilization of the trapped air, the influence of parameters like temperature and agitation (e.g., ultrasonic agitation to disrupt the adhesion between the air bubble and the trench surface) is investigated.

3.2.3 Infiltration Evaluation

For verification of the wettability of real surfaces, a new method was developed.

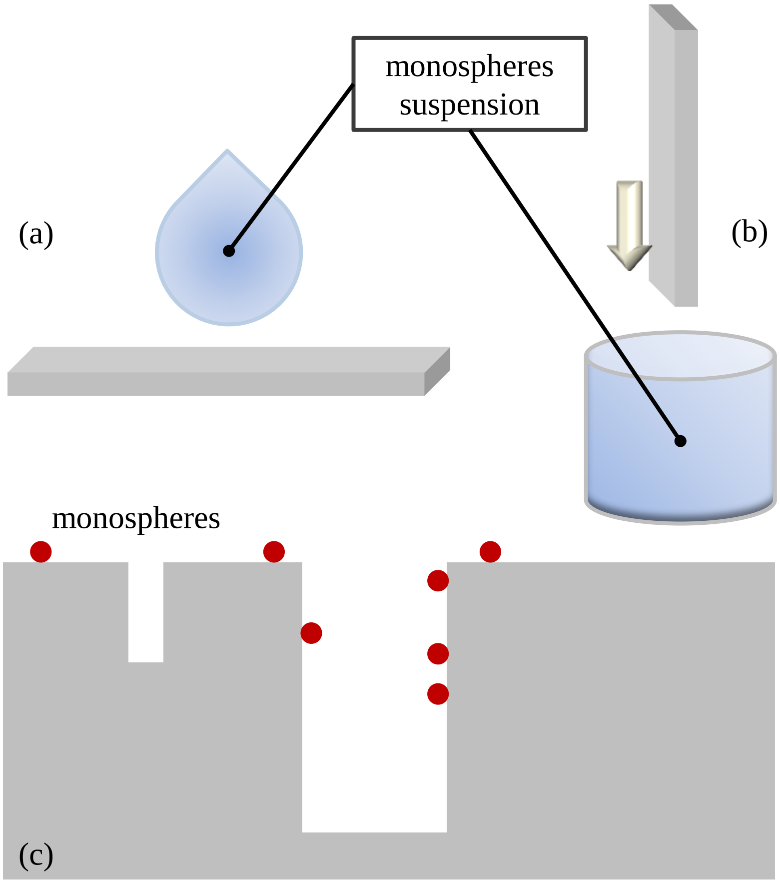

Figure 3. 10: Schematic images of the operating principle of the infiltration evaluation method. Application of the monospheres' suspension via dispensing (a) or dipping (b) with a possible monosphere distribution over a TSV after evaporation of the liquid part in cross-sectional view (c).

Instead of measuring the contact angle, the surface is covered with a test suspension. The solid part of the suspension consists of SiO_2 monospheres, whereas the liquid part is a solvent of known surface tension. Samples of any size can either be dipped into the suspension (Figure 3.10(b)), or the suspension can be dispensed on top of the sample surface (Figure 3.10(a)). After distribution of the suspension, the liquid part evaporates under ambient conditions, leaving the SiO_2 monospheres behind (Figure 10(c)). The monospheres act as tracers, providing information about the wetting of the trench structure depending on the penetrating properties of the suspension.

In order to perform exact measurements inside the trench, cross-sections of TSVs with different surface energies (hydrophobic and hydrophilic) are examined under an SEM after sample immersion and drying. Figure 3.11 illustrates the test plan of the experiment. For the liquid part of the suspension, two test liquids have been selected to create a high surface tension suspension of 72.75 mN/m, and a low surface tension suspension of 23.00 mN/m. Since wetting behaviour is also influenced by trench geometry, two different aspect ratios are taken into account: aspect ratio 1 to 5, and aspect ratio 1 to 2.5.

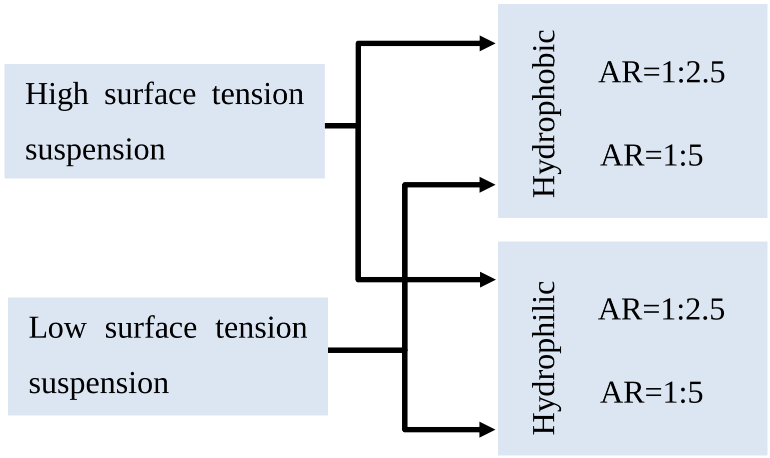

Figure 3. 11: Block diagram of the wetting experiment test plan. A high surface tension and a low surface tension suspension are spread over a specimen surface; each suspension has hydrophilic and hydrophobic properties, while the surfaces are TSVs of different aspect ratios.

Conventional aqueous cleaning processes apply a rinsing and drying sequence using water-based chemistries and IPA (drying based on Marangoni effect). The predominant application of DIW and IPA in wet-cleaning processes renders them perfect candidates as test liquids for the wetting experiments.

3.2.4 Polymer Undercut

As mentioned earlier, the TSV sidewall is isolated by SiO_2. Therefore, dilute hydrogen fluoride (HF) can be used to underetch or undercut the polymer residue by removing a small part of the interfacial SiO_2 layer.

The following SEM images demonstrate delamination of the sidewall polymer in a TSV after an HF treatment. Figure 3.12a depicts the upper part of a cross-sectional view on a delaminated sidewall polymer. As can be observed in the image, the polymer is shaped like the scalloped SiO_2 surface. In areas near the TSV bottom, the scallops are less pronounced and the polymer starts to wrinkle (Figure 3.12b).

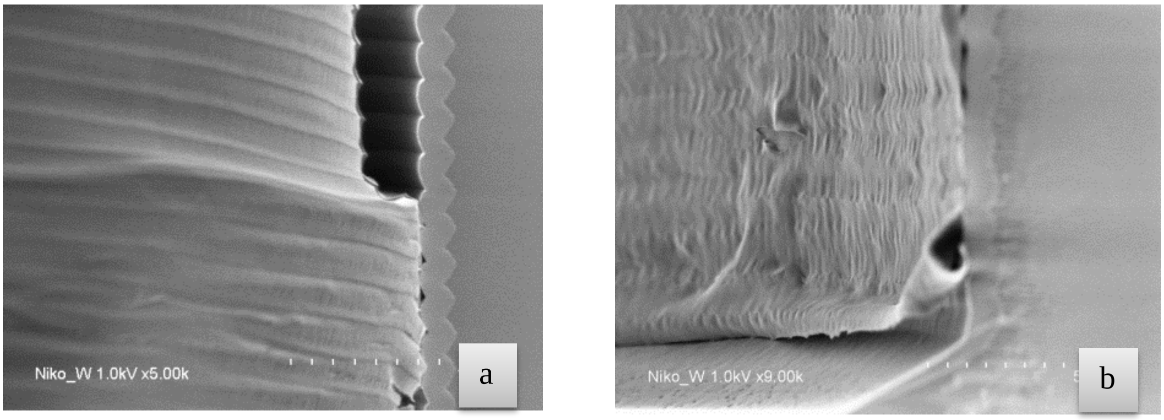

Figure 3. 12: Sidewall polymer delamination after hydrofluoric acid treatment. [Image provided by *ams AG*]

Since, metal contacts are exposed at the bottom of the TSV following through silicon-oxide-spacer etching (TSE) step a treatment with hydrofluoric acid (HF) is unfavourable. However, the direct contact of HF with the metallization at the bottom of the TSV can be avoided by a precise control of the penetration depth by tailoring of the acidic solution's surface tension. The penetration depth of a highly dilute HF is primarily determined by the water content of the solution. The surface tension of pure HF at 0 °C ($\sigma_{HF}^{0\,^{\circ}C}$) is 10.2 mN/m [61]. The surface tension of a DIW-HF mixture changes depending on the HF concentration. Starting with the surface tension of pure water (71.87 mN/m), the tension can be slowly decreased by increasing HF concentration.

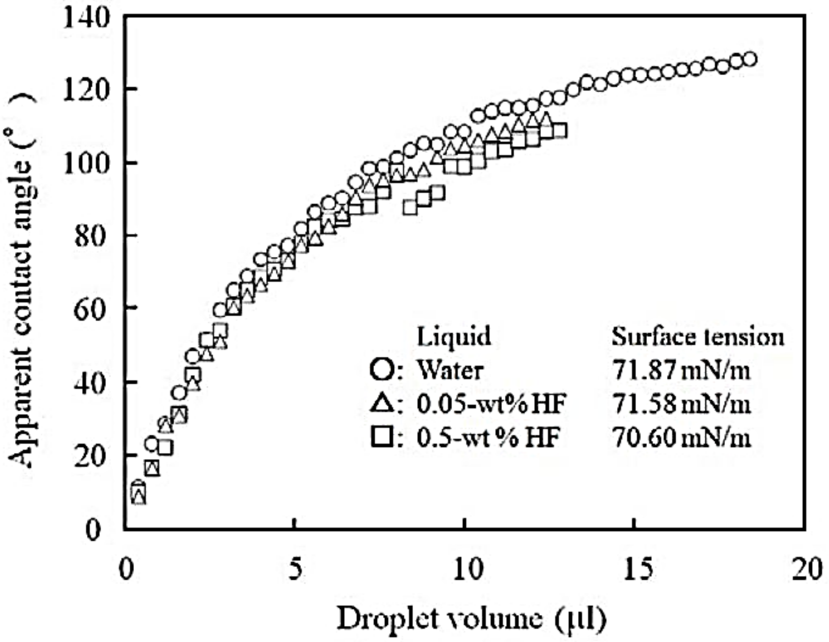

Figure 3. 13: Surface tension of diluted HF. Negligible changes in surface tension of water at low HF concentrations. [62]

For wafer cleaning, an HF treatment can be performed to remove a thin layer of SiO_2. For this step, also called HF-dip, an HF concentration in the range of 1- 2-wt% is usually selected. As demonstrated in Figure 3.13 [62], the surface tension decreases with increasing concentration. However, an HF content up to 2-wt% will lower the surface tension to approximately 70 mN/m. Consequently, an aqueous HF solution in this concentration range should not differ significantly in its infiltration behaviour from pure water with a surface tension of 71.87 mN/m. This approach enables the use of the underetching effect of diluted HF for polymer residue delamination without directly subjecting open metal areas to a corrosive environment.

Chapter 4 Experimental Results and Discussion

On the basis of TSVs with different aspect ratios, a new inspection and cleaning methodology has been developed. Two laboratory autoclaves for different specimen sizes have been designed and have been tested on the polymer residue labelling ability, whereas the evaluation was performed with a confocal laser scanning microscope (CLSM). In order to prove the theory of fluorophore pressure impregnation (FPI), a simplified version of a laboratory autoclave was designed for small specimens. After successful experiments, an autoclave scale-up to 200 mm wafer specimen with all necessary connections and measurement equipment was undertaken. The laboratory autoclaves were also integrated into the TSV polymer residue cleaning process in the form of a dry pre-cleaning step, which has proven to be highly effective as a preliminary step before wet cleaning.

4.1 Fluorophore Pressure Impregnation Autoclave

For validation of the FPI method, an experimental laboratory autoclave is designed. Design descriptions, used measuring apparatus, parameter settings and detailed experiment procedure are listed in 4.1.1 of this section. Section 4.1.2 presents the scaled-up laboratory autoclave. A detailed description of the FPI procedure is included in form of a basic flow sheet and a process flow chart. Additional engineering drawings provide particular information about the laboratory autoclave layout. Images of the complete equipment setup, parameter settings, and detailed experiment procedure complete this section.

4.1.1 Experimental Laboratory Autoclave

For labelling of sidewall polymer residue with a fluorophore - CO_2 mixture at critical point and above, a laboratory autoclave was developed. The autoclave consists of two 30-mm-thick transparent acrylic glass (trade name: Plexiglas) discs (identified as 6 in Figure 4.1) and one 30-mm-thick aluminium disc (identified as 5 in Figure 4.1). The process chamber has a capacity of approximately 85 ml.

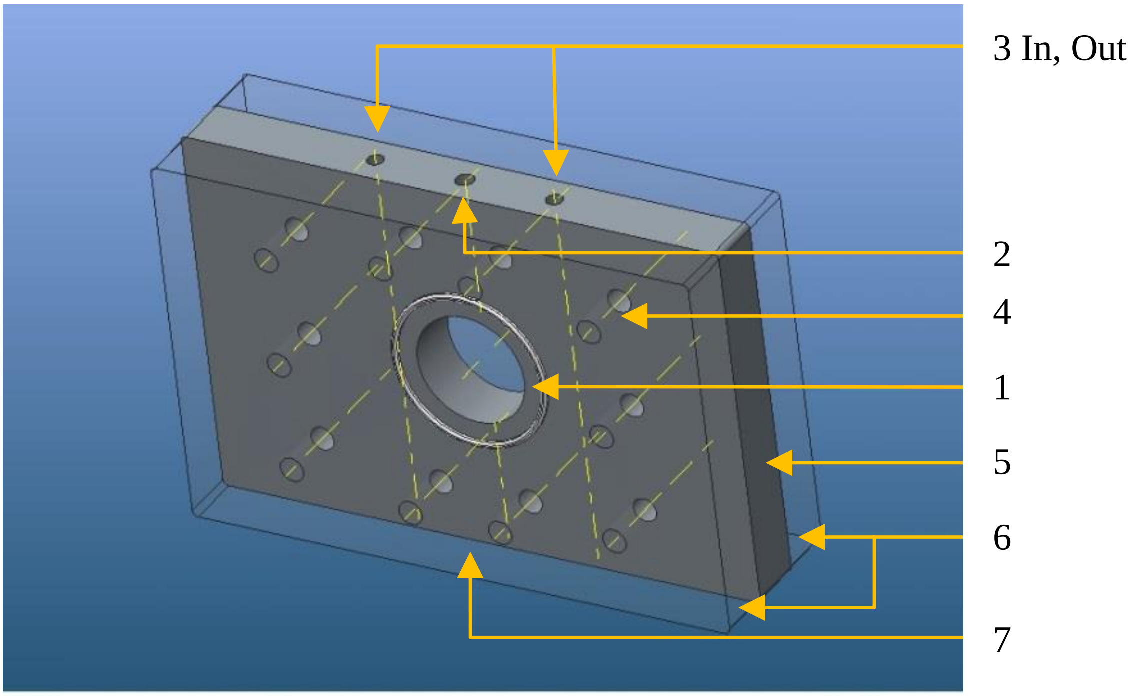

Figure 4. 1: Schematic picture of the 85-ml autoclave designed with PTC Creo 2.0. 1: drilling for the specimen and the dry ice with a diameter of 60 mm; 2: drilling for the pressure reducer and pressure gauge; 3: In and Out drillings for the filament; 4: drillings for the M12 bolts; 5: aluminium plate; 6: acrylic glass plates; 7: drilling for the temperature sensor.

Starting with the pressure on the contact surface, the force on one of the acrylic glass discs can be calculated using following relationship:

$$F = p * A \tag{4.1}$$

Thus, a force F of approximately 28.3 kN or rounded 2.9 tons are working against one disc, for a working pressure of 100 bar. Therefore, the three plates are fixed with 10 of M12 bolts (identified as 4 in Figure 4.1). The pressure monitoring takes place via a pressure reducer placed at drilling number 2. The pressure inside the autoclave is measured at the content pressure gauge. The pressure reducer in turn enables simultaneous decompression of the autoclave. The temperature inside the autoclave is adjusted with a filament, which is passed through the drilling “3 In”, travels around the autoclave, and leaves the aluminium plate at “3 Out”. The temperature sensor is placed opposite of the drilling number 2. Since aluminium is a good heat conductor (thermal conductivity of 235 W/ [m K]), measuring the temperature can be performed with negligibly small time delay.

The autoclave is designed for operation up to 100 bar pressure at temperatures up to 40 °C. The pressure is set with the initial CO_2 weight and the temperature controller. The cylinder opening 1 is sealed with two O-ring seals on each side. As CO_2 diffuses into the material after a certain time, resulting in a swelling and deformation of the sealing, it is recommended to use PTFE O-rings.

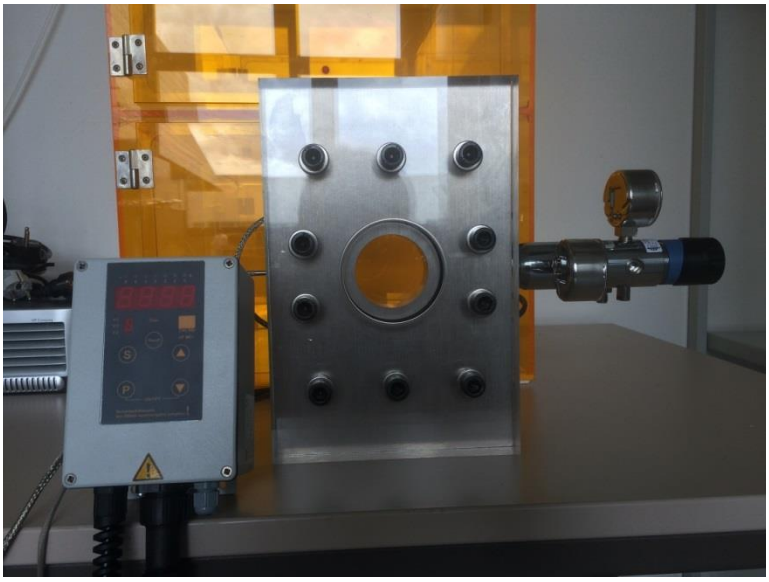

Figure 4. 2: Setup image of the autoclave with temperature controller and pressure reducer.

Figure 4.2 depicts the setup front including the temperature controller (Microprocessor Temperature Regulator HT MC1; distributed by *horst*) on the left and the pressure reducer on the right side. The temperature controller is connected to the filament and the temperature sensor, both placed inside the drillings number “3 In and Out” and 7 (Figure 4.1). The pressure reducer is screwed into drilling number 2, which, in contrast to the rest of the drillings, is directly connected to the chamber.

In the beginning of the FPI in the experimental laboratory autoclave, 20x20 mm-small specimen pieces are placed with a diluted fluorophore droplet inside the chamber. CO_2 is introduced into the chamber as dry ice nuggets, which are tightly packed around the specimen. During the bolting of the two acrylic glasses to the aluminium plate, the pressure-reducing valve remains open, preventing a too-quick pressure built-up inside the autoclave and therefore a premature melting of the ice. As soon as the screws are tightened, the pressure-reducing valve is closed and the heating filament is switched on.

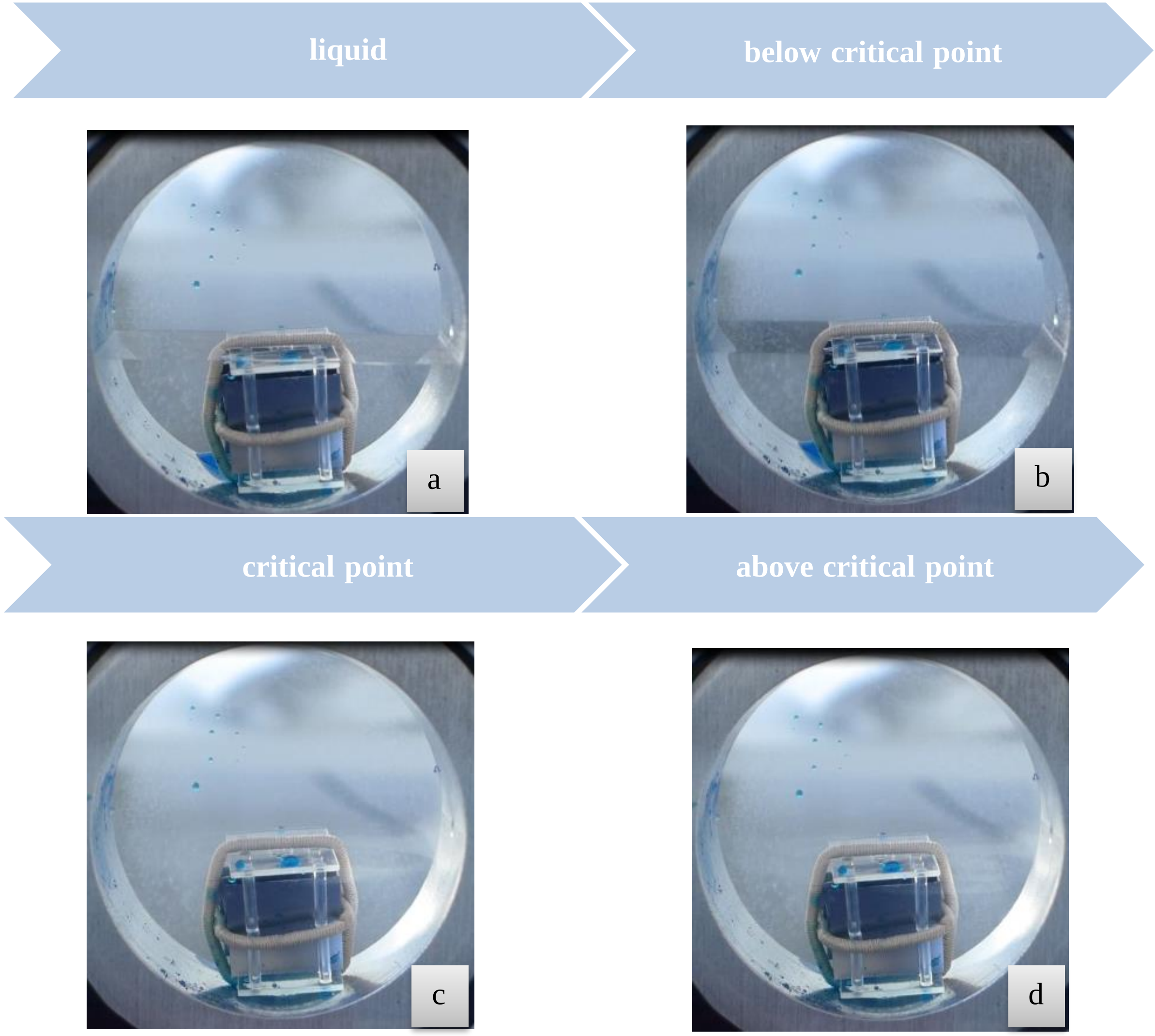

Figure 4. 3: Images of specimen holder, including the specimen and the blue-colored fluorophore, in different phases of CO_2 from liquid to supercritical.

With increasing pressure and temperature, the dry ice first begins to melt, building up a boundary layer between the CO_2 gas and the CO_2 liquid. Furthermore, heating causes dissolution of the boundary layer, turning it to a supercritical aggregate state. Figure 4.3 contains pictures taken of CO_2 phase transitions from liquid to supercritical and specimens (four 20x20 mm pieces in a specimen holder) placed inside the chamber. The blue droplets are the fluorophore dissolved in DIW. Clearly recognizable is the boundary layer between the gaseous CO_2 and the liquid CO_2 in the first two images (Figure 4.3 a, b) of liquid CO_2 and

CO_2 just below the critical point. The disappearing boundary layer is clearly recognizable in the last two stages which are CO_2 at the critical point and above (Figure 4.3 c, d).

At the end of the impregnation time, the pressure-reduction valve can be gradually opened for chamber decompression. Once ambient pressure inside the autoclave has been reached, the bolts can be unscrewed and the dry, labelled specimen pieces can be removed. This autoclave is particularly suitable for investigation of fluorophore impregnation for different specimens and different fluorophores. Additionally, a variation of process parameters is possible within the maximum pressure and temperature which are defined for this experimental laboratory autoclave. This type of autoclave can be easily reproduced and its simple operation allows quick experimental procedures. By consistently filling the autoclave with the same quantity of dry ice, the experimental conditions and thus the experimental results are reproducible. Since the 85-ml autoclave is designed exclusively for small pieces, an autoclave scale-up has been performed, which is described in the following section.

4.1.2 Laboratory Autoclave Scale-Up

For a complete wafer (e.g., 200-mm wafer) investigation, a scale-up of the experimental laboratory autoclave has been designed. In addition, the autoclave is filled with liquid CO_2 instead of dry ice and the fluorophore is dissolved in $scCO_2$ prior to entering the autoclave. The underlying process of the presented FPI procedure is diffusion. The term “diffusion” is understood to be the movement of a gas, fluid, or solid substance down a concentration gradient.

The process target of the procedure depicted in the block diagram (Figure 4.4) is to impregnate fluorophores into a polymer using CO_2 as transport medium. The major process steps the fluorophore is going through are as follows:

1 Compression → **2** Dissolution → **3** Impregnation → **4** Decompression → **5** Filtering

The process starts with compression (**1**) of liquid CO_2 blended with the fluorophore. CO_2 is taken from a bottle which has approximately 57 bar at room temperature. CO_2 and the fluorophore are compressed to approximately 100 bar. When the process pressure is reached, the fluorophore is dissolved (**2**) in the mixing unit, while the fluorophore solvation takes place under $scCO_2$ state conditions. After dissolution, the fluorophore-CO_2 mixture is released into the autoclave where FPI (**3**) at approximately 100 bar and 40 °C takes place. The fluorophore is impregnated into the polymer residue of the wafer placed inside the autoclave. At the end of the impregnation, the autoclave is decompressed (**4**) to ambient pressure. The exhaust gas containing CO_2 and the unused fluorophore pass through a filter (**5**) towards exhaust air. After complete decompression, the wafer with now-labelled polymer residue is removed from the chamber.

In parallel to the fluorophore-CO_2 strand, CO_2 is simultaneously released into the autoclave and compressed to supercritical state. This volume is necessary to cover the wafer completely and dilute the fluorophore-CO_2 mixture coming from the mixing unit.

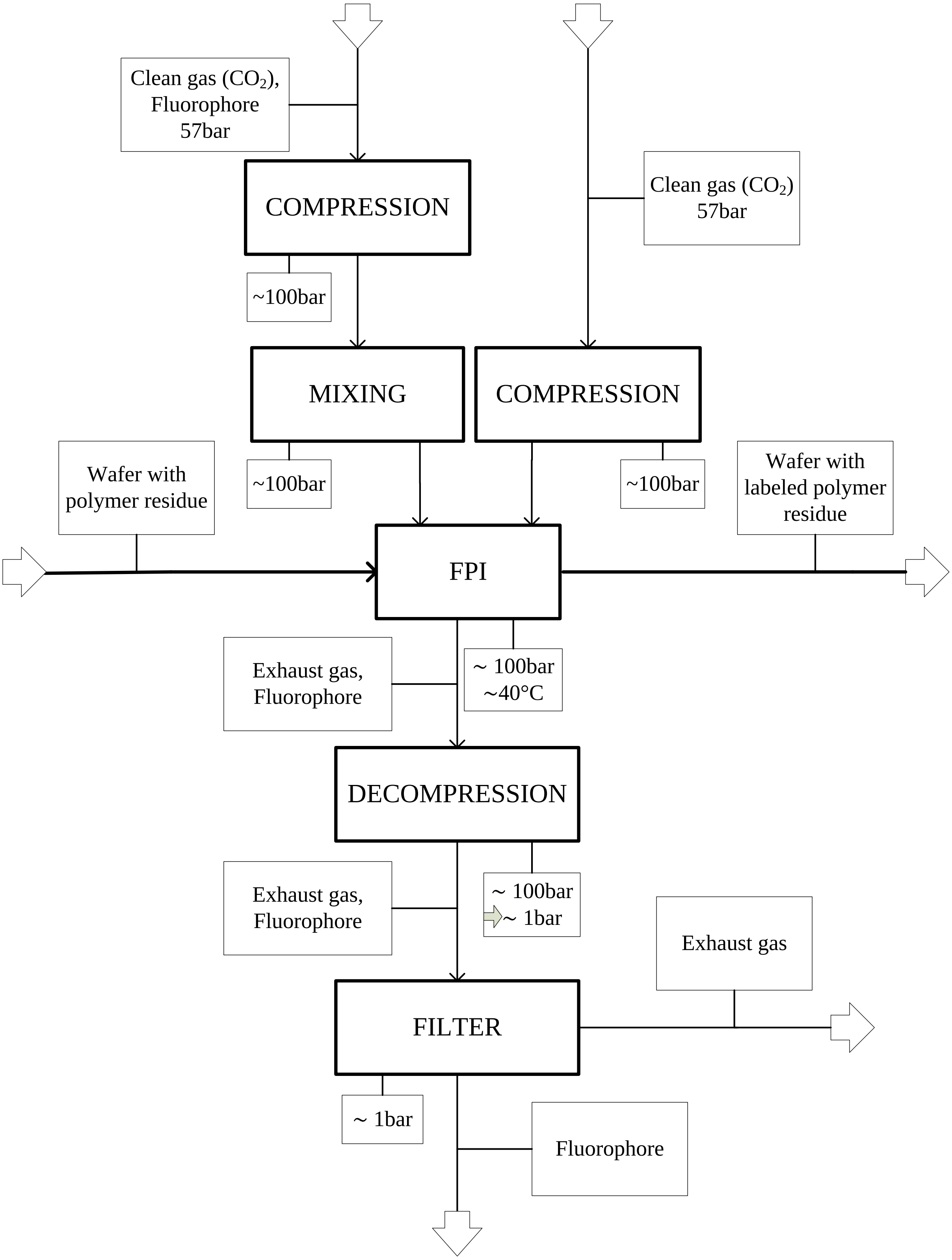

Figure 4. 4: Basic flow sheet to the FPI setup sharing the sequence of the FPI process.

Process sequence

The process flow diagram depicted in Figure 4.5 illustrates the procedure for fluorophore pressure impregnation in polymer residue on wafer specimen. Additionally, the accessories list provides information about the valves and instruments used, as well as the corresponding suppliers selected for the scale-up construction.

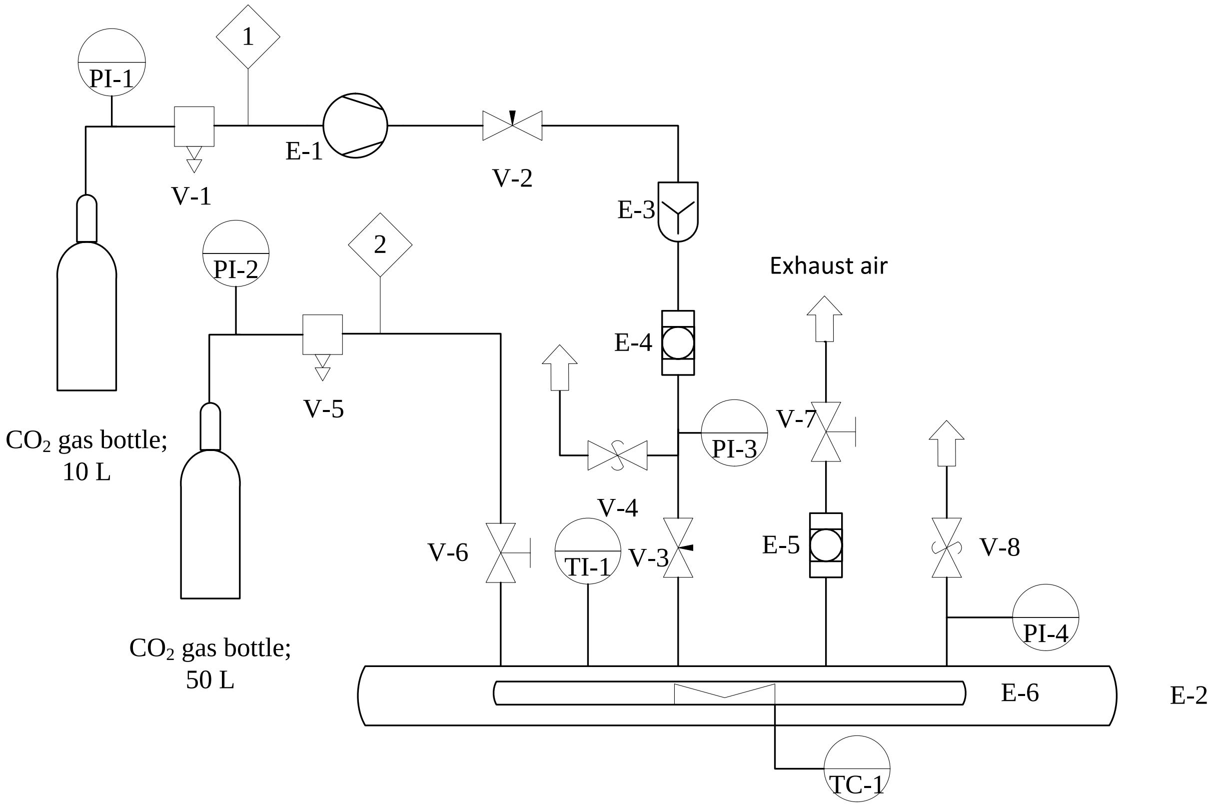

Accessories	
Text displayed	**Specification**
E-1	CO2 syringe pump SFC-24 [sunchrom]
E-2	Laboratory autoclave [kempe]
E-3	Fluorophor mixing unit
E-4, E-5	Inline Filter; 0.5µm [swagelok]
E-6	Heating plate
V-1, V-5	Venting valve [rinnert]
V-2, V-3	Needlevalve; 10,000psi [HIP]
V-4, V-8	Rupturedisc; 1,740psi [swagelok]
V-6, V-7	Stopvalve [swagelok]
TI-1	Temperature controller SCTSD [parker]
TC-1	Microprocessor Temperature Regulator HT MC1 [horst]
PI-4	Pressure controller SCPSD [parker]
PI- 1-3	Manometer analogue

Figure 4. 5: Process flow chart of the FPI process and the related list of accessories.

Pipeline 1 (marked with a rhombus) represents the pipes and equipment that the fluorophore-CO_2 mixture passes until it enters the autoclave E-2. Liquid CO_2 comes from a 10 L CO_2 gas bottle with a dip tube. The analogue manometer PI-1 displays the pressure in the pipe between the gas bottle and the syringe pump E-1. The venting valve V-1 is used to vent the pipe section up to the syringe pump. Between the two needle valves V-2 and V-3, a mixing unit E-3 and an online filter are placed. Additionally, an analogue monometer PI-3 and a rupture disc V-4 are installed. The fluorophore-CO_2 mixture is released into the atmosphere if the rupture disc breaks.

Pipeline 2 (marked with a rhombus) represents the pipes and equipment CO_2 passes before it enters the autoclave. Liquid CO_2 comes from a 50 L CO_2 gas bottle with a dip tube. The analogue manometer PI-2 displays the pressure in the pipe between the gas bottle and the stop valve V-6, while the stop valve releases the liquid CO_2 into the autoclave.

The wafer specimen is placed on the heating plate E-6, which is heated by the microprocessor temperature regulator TC-1. To monitor the temperature and pressure inside the autoclave, a temperature controller TI-1 and a pressure controller PI-4 (integrated on the same pipe as the rupture disc V-8) are installed. The CO_2 mixture from the autoclave is released into the atmosphere if the rupture disc breaks.

During decompression, the CO_2 gas mixture passes through the online filter E-5 and the stop valve V-7 and is released through the exhaust into the air.

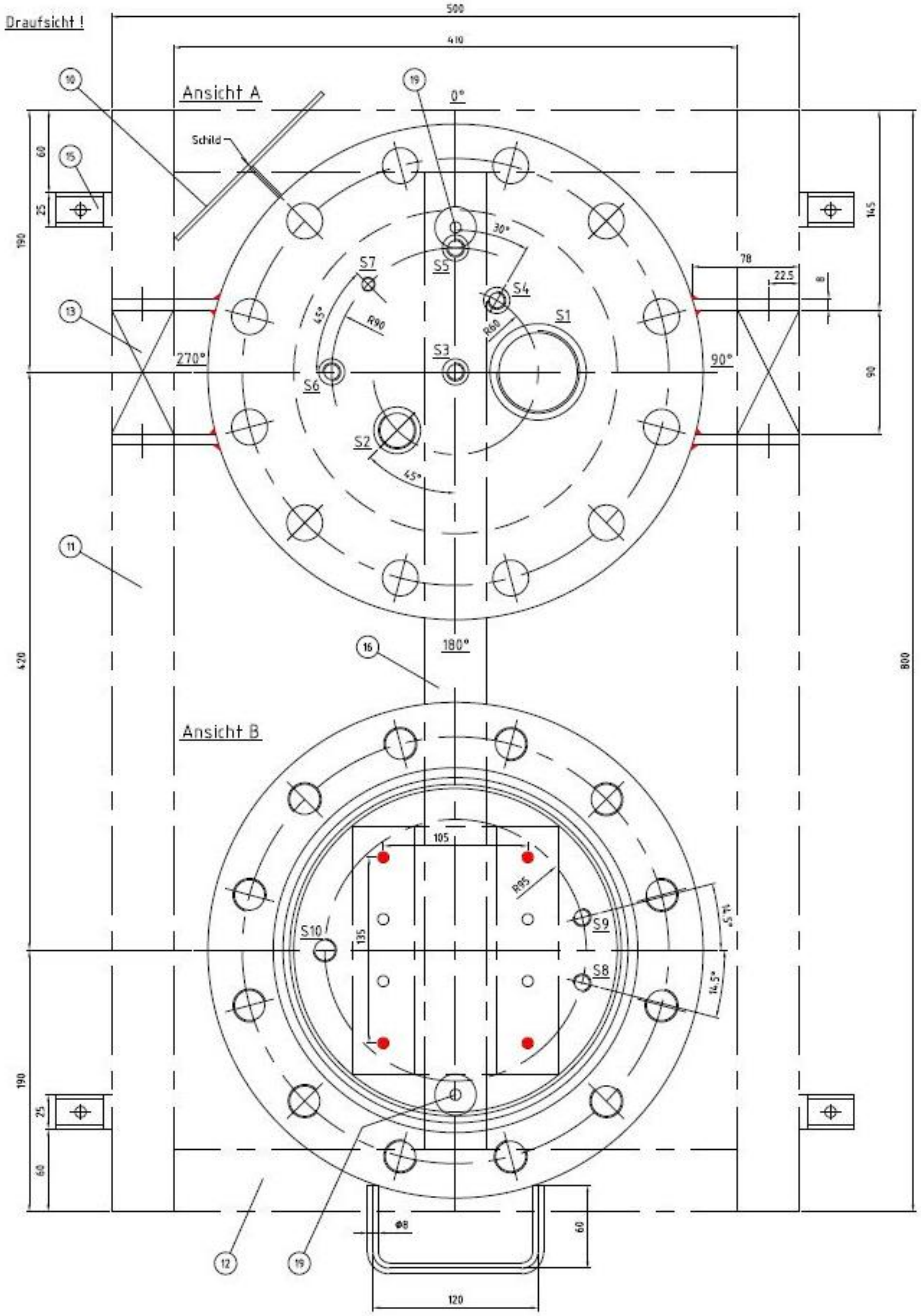

Figure 4. 6: Engineering drawing of the autoclave in the plan view. [Drawing delivered by *Siegfried Kempe GmbH*]

Figure 4.6 illustrates the engineering drawing of the autoclave in a plan view. The autoclave consists of two parts. View A (Ansicht A in Figure 4.6) represents the autoclave cover and view B (Ansicht B in Figure 4.6) the autoclave bottom, which are made of 1.4571 stainless steel. The sight glasses S1 and S2 are arranged in a radius of 60 mm, while S1 has a larger radius than S2. Both sight glasses are fused metal and therefore suitable for high pressure applications. For the temperature controller, a tapped hole S7 is placed in a radius of 90 mm. The tapped hole S4 is intended for the pressure controller – rupture disc construction. The fluorophore-CO_2 mixture enters the autoclave through the tapped hole S5, while the pure CO_2 enters through the tapped hole S6. During decompression, CO_2 and the remaining fluorophore exits the autoclave through the tapped hole S3. On the outer rim, 12 drilling holes are arranged for M24x115 bolts that go completely through the autoclave cover. For fixation, two holding devices are welded laterally to the autoclave.

Three tapped holes are considered for the autoclave bottom. S10 is intended for the cabled infeed necessary for the heating plate, or rather for the connection of temperature controller. S8 and S9 are designed for the cooling coil pipe, which passes a cooling plate. The heating and cooling plates are designed and manufactured separately, and are described at the end of this section. For the Viton O-ring sealing, a round milling groove of 240x5 mm is realized. The autoclave bottom can be pulled using the welded handle. Just like the autoclave cover, the bottom has 12 tapped holes for M24x115 bolts.

Figure 4.7 contains the engineering drawing of the autoclave in cross-sectional view. The cover has a thickness of 68 mm. This view provides cross-sections of the Metaglas sight glasses S1 and S2 and the tapped holes for the temperature controller S7 and outlet pipe S3. The autoclave bottom has a thickness of 100 mm and a round milling groove with a depth of 50 mm. The deepening has a radius of 237 mm in the first 35 mm and a precise radius of $235_{\pm 0.05}$ mm in the last 15 mm. The deepening and the heating plate, which are explained in the following section, build the processing volume. The tapped holes S10 for the temperature microprocessor and S8 and S9 for the cooling coil are arranged in the outer radius of the deepening (hereafter referred to as the chamber). During the removing of the 12 bolts, the autoclave bottom is lowered and sits on four pins which are part of the guideway (for detailed description see next section). These pins are illustrated in Figure 4.6 and in Figure 4.7 at the autoclave bottom. The cover and the bottom are fixed together, while only the autoclave bottom has 12 tapped holes for the bolts.

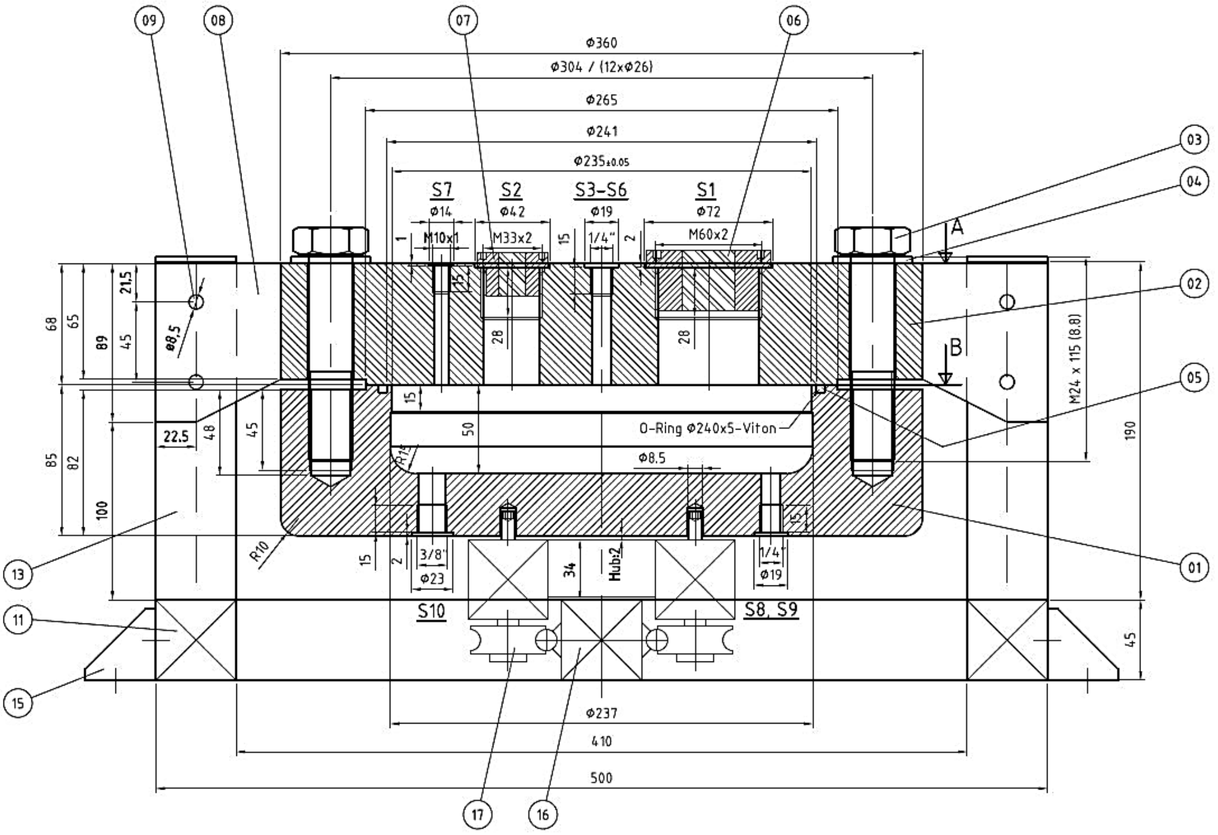

Figure 4. 7: Engineering drawing of the autoclave in cross-sectional view. [Drawing delivered by *Siegfried Kempe GmbH*]

Figure 4.8a-d displays engineering drawings of the heating plate in complete and cross-sectional views. The heating plate is 25 mm thick and is realized for the upper part of the autoclave chamber. View (a) depicts the complete aluminium heating plate for a wafer of up to 200 mm, which is placed face-up on four pins (marked with a red number 2). Placing and picking of a wafer is performed by a vacuum gripper placed in the recess (marked with a red number 1). The plate is lowered into the chamber using two eyebolts screwed into the drilling holes (marked with a red number 3). An axial sectional view (b) presents the positions of the two heating elements (marked with a red number 5) and the temperature sensor (marked with a red number 6). These positions are also presented in a lateral sectional view in Figure 4.8d. A milling groove (marked with a red number 4) hermetically seals the chamber to the chamber bottom, when the tapped holes S10, S8, and S9 (Figure 4.7) are open. The cylindrical bore holes are designed for two heating elements with a diameter of 8 mm and a length of 130 mm (Figure 4.8c), and one sensor with a thickness of 4 mm and a length of 50 mm.

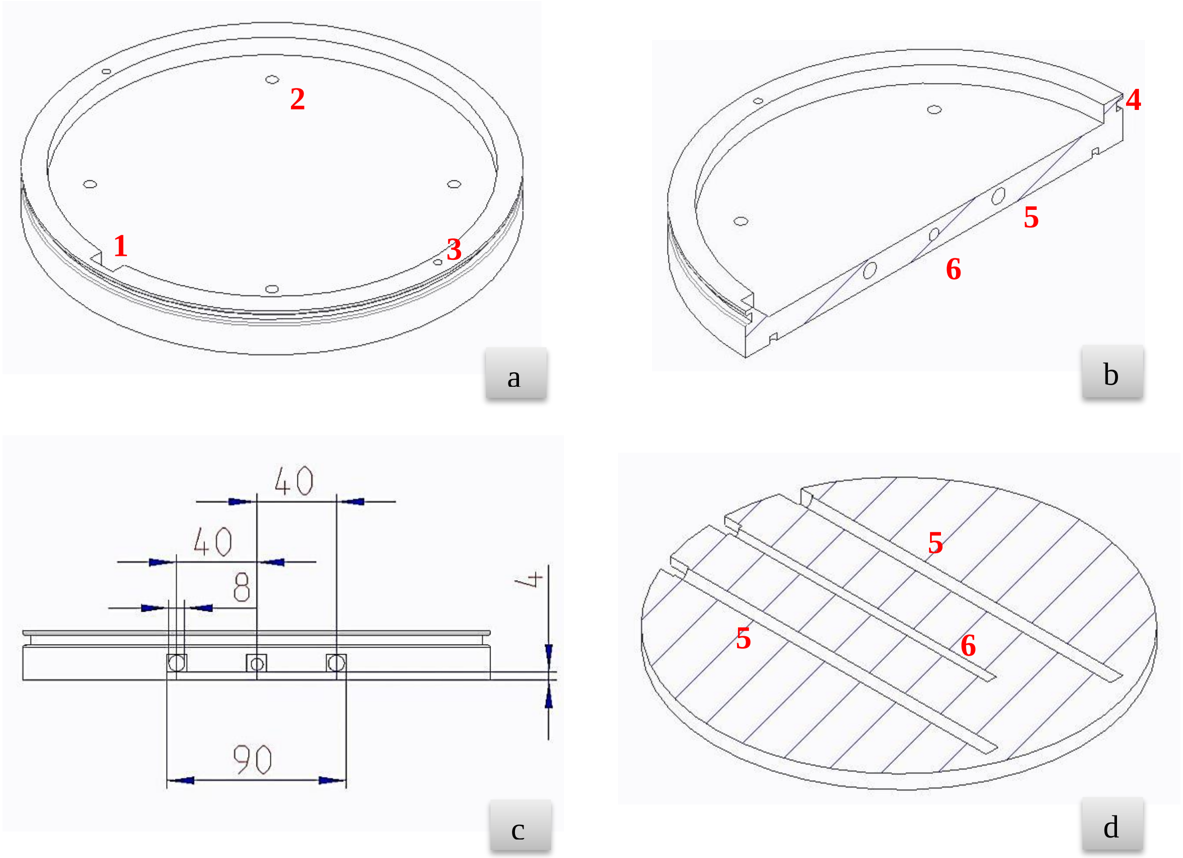

Figure 4. 8: Engineering drawing of the heating plate to be inserted into the autoclave.

Figure 4.9a, b presents engineering drawings of the cooling plate. This plate is placed in the chamber bottom. The cooling coil (which is intended to be a stainless-steel tube) is passed through the bore hole in the plate (marked with a green number 1) from bottom to top. The tube is bent into a circle and placed in the milling groove (Figure 4.9b, marked with a green number 1) and leaves the plate through the second bore hole (Figure 4.9a, marked with a green number 1). The heating plate cable passes through the bore hole (marked with a green number 2), which is positioned congruent to S10 (Figure 4.7). The plate is lowered into the chamber using two eyebolts screwed into the drilling holes (marked with a green number 3). Afterwards, the eyebolts are removed and positioning pins are screwed in to align the heating and cooling plates.

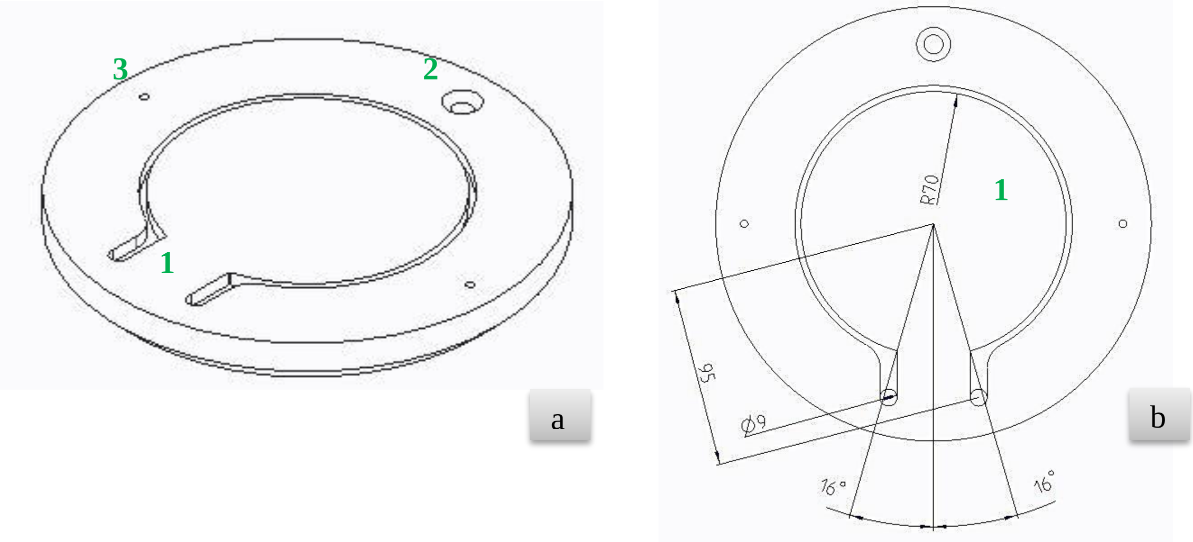

Figure 4. 9: Cooling plate to be inserted into the autoclave.

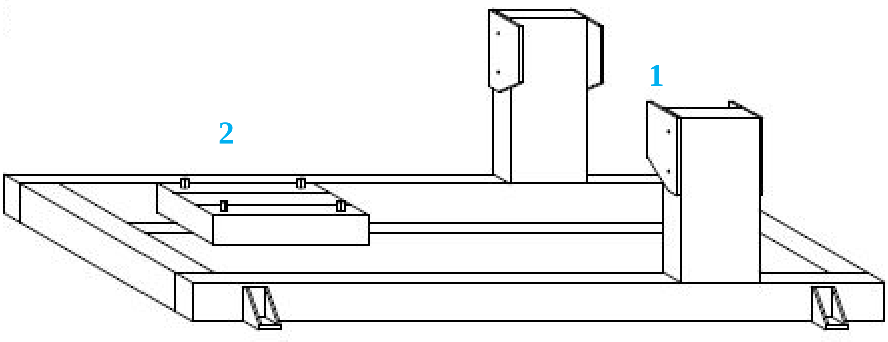

Figure 4 10: Framework without the autoclave. [Drawing delivered by *Siegfried Kempe GmbH*]

Figure 4.10 demonstrates the framework without the autoclave. The position of the cover is fixed by aluminium profiles (marked with a blue number 1), whereas the autoclave bottom can be moved along the guide way sitting on the plate with four pins (marked with a blue number 2). In this way, the wafer can be placed in or removed from the autoclave.

The chamber depicted in Figure 4.7 has a volume of 2.2 L. Introducing the heating and cooling plates inside the chamber, the volume is reduced to approximately 0.4 L. The finished autoclave has a weight of approximately 125 kg and is completely made of 1.4571 stainless steel. The maximum allowable pressure is +160 bar and the minimum and maximum allowable temperatures are -10 °C and +60 °C, respectively. The sight glasses are designed for process pressures up to 200 bar (Figure 4.7 S1) and 400 bar (S2). The autoclave cover is sealed with 12 M24 bolts, using a tightening torque of 128 Nm.

Figure 4.11 illustrates the closed autoclave with the connected fluorophore-CO_2 mixture pipe inlet (Inlet I), the pure CO_2 pipe (Inlet II) and the gas outlet that releases exhaust into the air (Outlet). In addition, the pressure controller measuring 19 bar and the temperature controller measuring 25.3 °C can be observed.

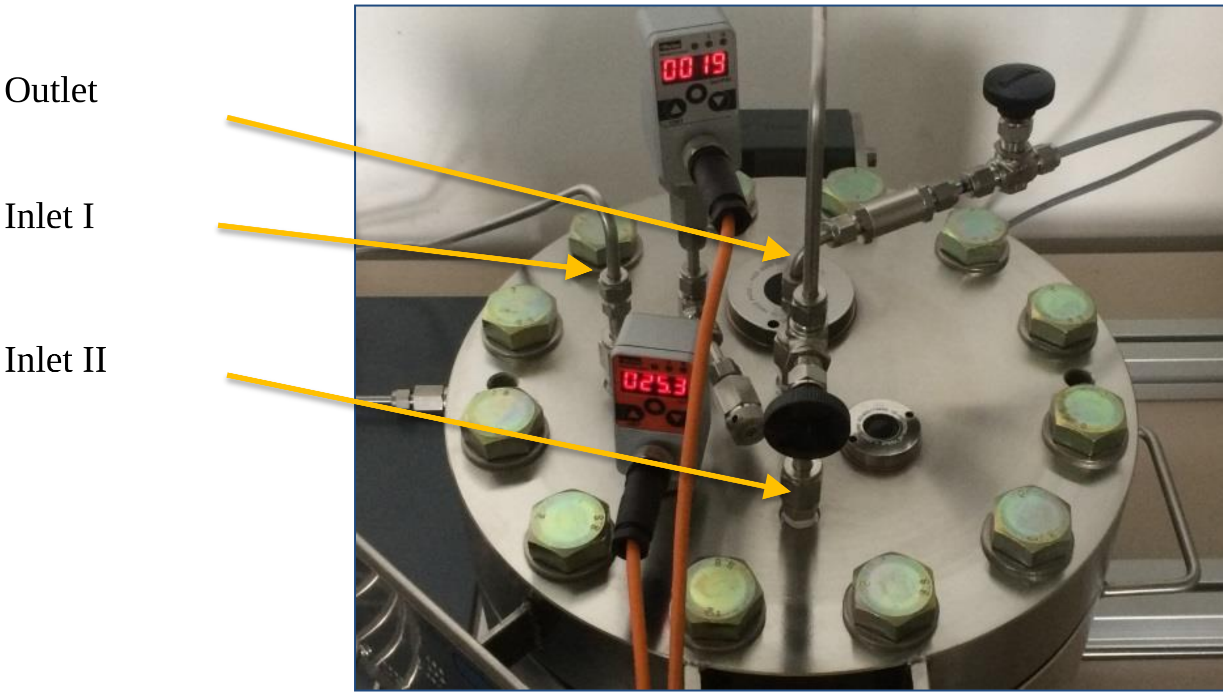

Figure 4. 11: Closed autoclave with inlet and outlet pipes, and temperature and pressure controllers.

The complete construction depicted in Figure 4.12 illustrates from left to right a syringe pump for $scCO_2$ with a maximum flow rate of 24 ml/min and a maximum pressure of 10,000 psi (equivalent to around 690 bar). Two pump heads inside the syringe pump enable a constant pressure mode and thus a selectable pressure set point. Since the supercritical pump can be operated only with liquid CO_2, it is connected directly to a 10 L CO_2 bottle with a dip tube. A pressure reducer is not installed between the bottle and the pump.

Once the CO_2 is compressed to the supercritical state, it enters the mixing unit. The task of the mixing unit is to dissolve the fluorophore in CO_2. Next, the CO_2-fluorophore mixture enters the autoclave (open autoclave in this picture) with the wafer which already is filled with liquid CO_2 by a second 50 L CO_2 bottle with a dip tube.

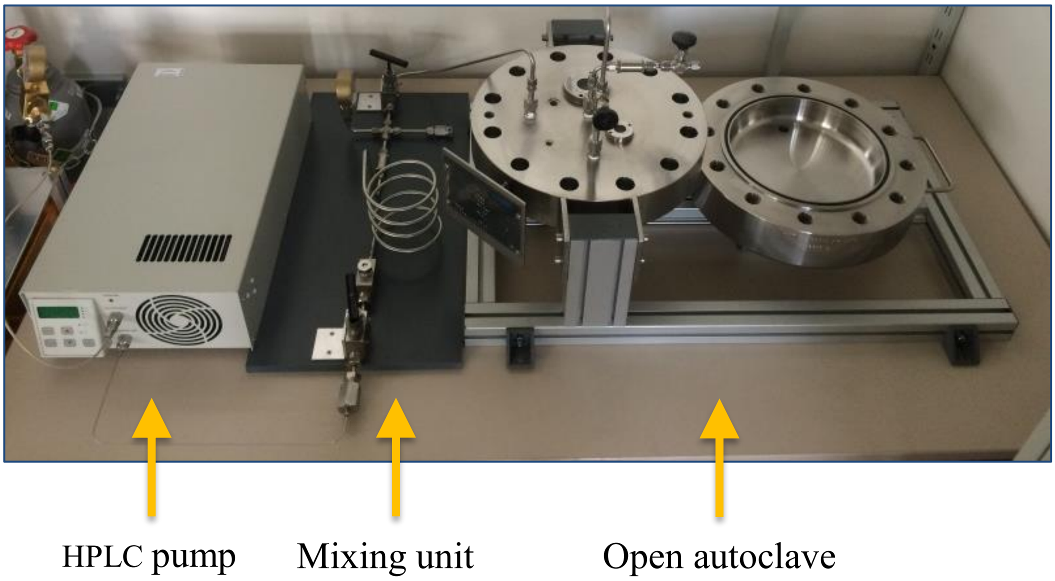

Figure 4. 12: Complete equipment setup (excluding the measuring apparatus) for the FPI process.

The mixing unit (Figure 4.13) is employed as follows: first, the fluorophore-water dispersion is pipetted into the injection chamber; next, a small flow (~2 ml/min) of CO_2 is passed through the mixing unit to remove the air and humidity in the pipes. As a result, both needle valves are opened. For compression of the CO_2 to supercritical state, valve V3 is closed. The syringe pump delivers continuous CO_2 until the set pressure value is reached. The mixing unit is designed for pressures up to 690 bar. However, a rupture disc for a maximum pressure of 160 bar is installed between the valves to avoid an uncontrolled increase in pressure. An inline filter of 0.5 µm pore size is installed to prevent unsolved fluorophore fragments from entering the autoclave. The mixing spiral provides additional volume for the dissolving process.

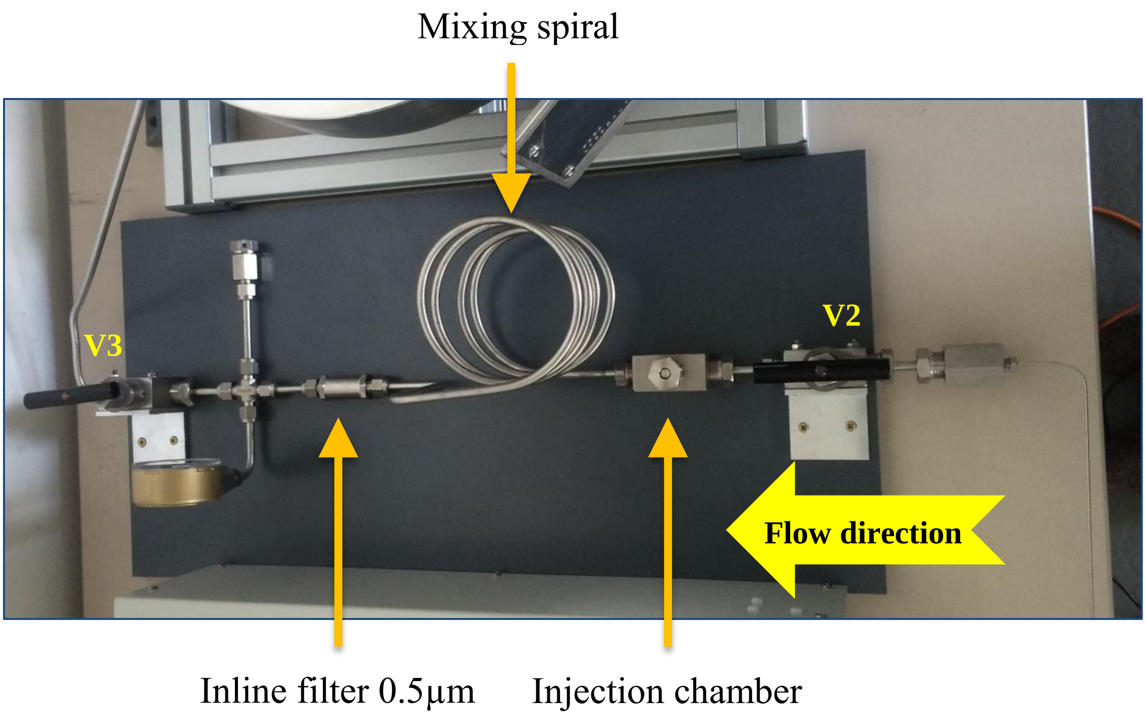

Figure 4. 13: Mixing unit for the fluorophore pressure impregnation setup.

Before starting the FPI, the autoclave and the pipe lines must first be purged with CO_2 gas while all valves are open and the wafer specimen has already been placed on the heating plate inside the autoclave. To displace air and humidity, the syringe pump must be purged with CO_2 at low flow rates (~2 ml/min) for approximately 20 minutes. Purging also cools down the pipes and the heat exchanger of the pump. Cooled equipment improves the constant liquid and $scCO_2$ flow, avoiding turbulence due to temperature fluctuations. At the beginning of purging, icing of pipe lines and valves can be observed. This process can be explained by the Joule-

Thomson effect, which is discussed below. In addition to the icing effect, the CO_2 density is lowered at low temperatures; therefore, a larger quantity of liquid CO_2 can be used to fill the cooled autoclave, which provides higher pressures during heating of the CO_2.

The fluorophore solution is pipetted into the injection chamber. The mixing unit is purged again and valve V3 is closed. The flow rate is now increased and the final pressure is set to 120 bar. As soon as the required pressure is reached, the pump is turned off and valve V2 is closed. The fluorophore is dissolved by the scCO_2 over time. In the meantime, the autoclave is filled with liquid $CO_{2,}$ with an initial pressure of 58 bar and a temperature of approximately 20 °C. During the autoclave filling process, valves V7 and V3 are closed and V6 is open. When the pressure controller measures 58 bar, V6 is closed and the fluorophore-CO_2 mixture can be injected by closing valve V2 and opening valve V3. Valves V1 and V5 are opened to avoid a further pressure increase in the pipes. As long as the mixing unit is put under a higher internal pressure than the autoclave, there will be no CO_2 streaming against the flow direction. After impregnation has finished the chamber is decompressed, the bolts are loosened, and the wafer with labelled polymer residue is removed.

Joule Thomson effect

As mentioned in the previous section, pipes and valves that cool down rapidly build up an ice layer. The reason for the icing relates to the Joule-Thomson effect, which describes the change in temperature of a real gas during an isenthalpic pressure reducer. An isenthalpic process means that the enthalpy of the fluid is constant during the process. During decompression, CO_2 which is a real gas can expand its volume. Throttling of real gases provides rapid cooling of the gas by conversion of kinetic energy to potential energy. The velocity of the gas molecules reduces with the consequence that the gas temperature decreases. This decrease can lead to undesired blockages when residual humidity is left inside equipment such as valves.

4.2 Fluorophore Pressure-Impregnated Polymer Residue in Trenches

This section discusses the CLSM images of fluorophore pressure-impregnated sidewall polymers in TSVs and various dry etched trenches.

After FPI, the wafer sample is cleaved into 20x20 mm sized specimen. For inspection, the specimen is fixed on a microscope slide with transparent nitrocellulose lacquer and placed face-down under the CLSM.

A helium-neon laser is used to excite the fluorescent electrons of the ATTO 647N dye. The emitted fluorescent light passing a dry objective is recorded by a HyD detector. For a proof of concept, wafer samples with a high degree of polymer contamination directly after a through silicon-oxide-spacer etching step have been used. In order to confirm the presence of polymer residue inside the TSV, an SEM cross-section analysis of the TSVs was performed.

The SEM image (Figure 4.14a) depicts the upper part of the TSV, with a clearly visible, partially-delaminated polymer film. The rest of the TSV sidewall is continuously covered by the polymer. The same wafer samples are inspected under the CLSM with the following results: Figure 4.14b) shows a fluorescence image captured in a top-down view of one TSV. The fluorescent light is displayed in the false-colour red. The partially-delaminated sidewall polymer is clearly visible inside the TSV. The polymer sections which are in the focal plane are coloured in an intensive red, while the out-of-focus (impregnated) layers are dim.

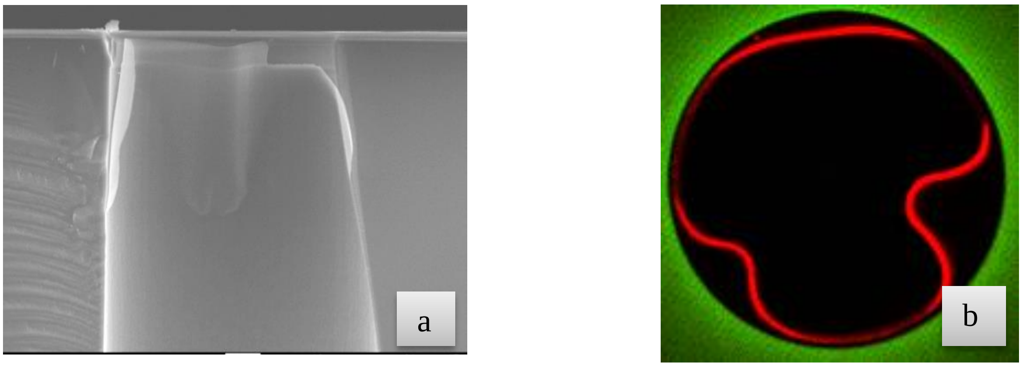

Figure 4. 14: SEM image (a), confocal laser scanned image with dry objective (b) of a TSV in cross-sectional and top down view after TSE process, AR 1:2.5.

The background inside the TSV appears black in the images, because all extra light produced by laser excitation is eliminated by the pinhole. The sample surface is also illuminated with a diode pumped solid state DPSS 561 nm laser, which emits in the yellow-green region of the spectrum. The laser light is reflected on the sample surface and detected by PMT3 set in reflection mode, producing a green image background whose better contrast facilitates the search for fluorescent spots.

Application of low-magnification objectives enables a simultaneous observation of multiple TSVs at once (Figure 4.15). All inspected TSVs display labelled sidewall polymers, which can be clearly detected at this magnification level. This magnification level can be used for a first screening of the wafer sample.

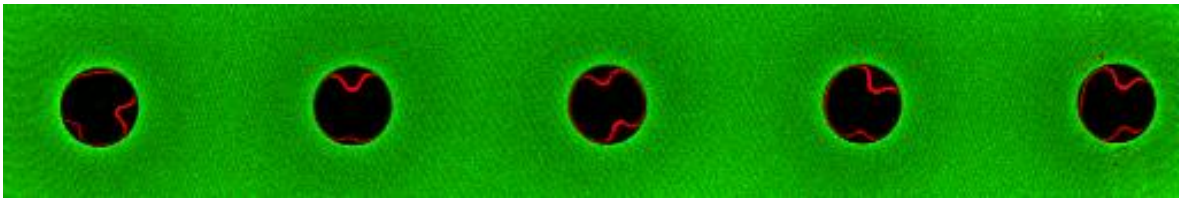

Figure 4. 15: Confocal laser scanned image of five labelled TSVs in top view after TSE step, AR 1:2.5.

The following images (Figure 4.16) compare two fluorophore pressure-impregnated TSV polymer residue after an impregnation time of 15 and 30 minutes, respectively. The impregnation pressure is between 80 and 95 bar with an according temperature of 31 °C. In both TSVs, the polymer residue are delaminated from the sidewall at the top of the TSV. Besides this delamination, the polymer residue (Figure 4.16a) appears to have partly collapsed, since it is out of observation focus. Comparing the fluorescence intensities after 15 and 30 minutes of impregnation, it is clear that the intensity of the latter adjustment is several levels higher. However, the polymer residue in the case of 15-minute impregnation are still clearly visible.

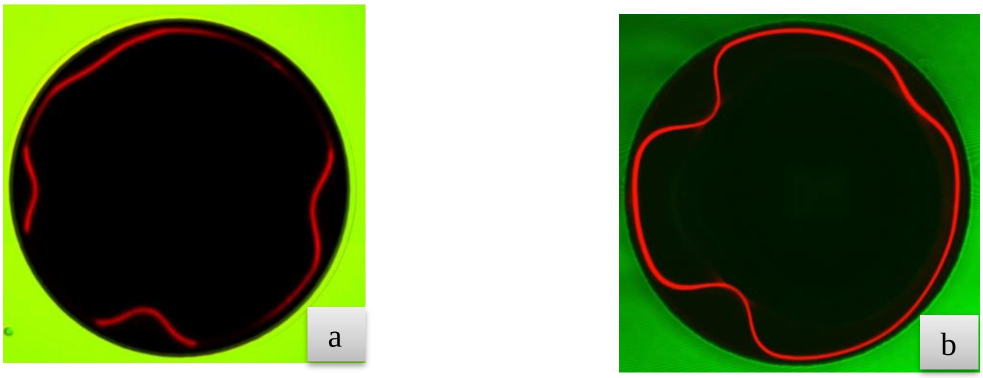

Figure 4. 16: Images of TSVs top views with the green reflecting wafer surface, the red fluorescent polymer. TSV polymer residue after 15 min impregnation time (a), 30 min impregnation time (b), AR 1:2.5.

Since polymer residue in TSVs of AR1:2.5 can be successfully detected using the FPI, the new method is examined on a smaller diameter size (AR 1:5).

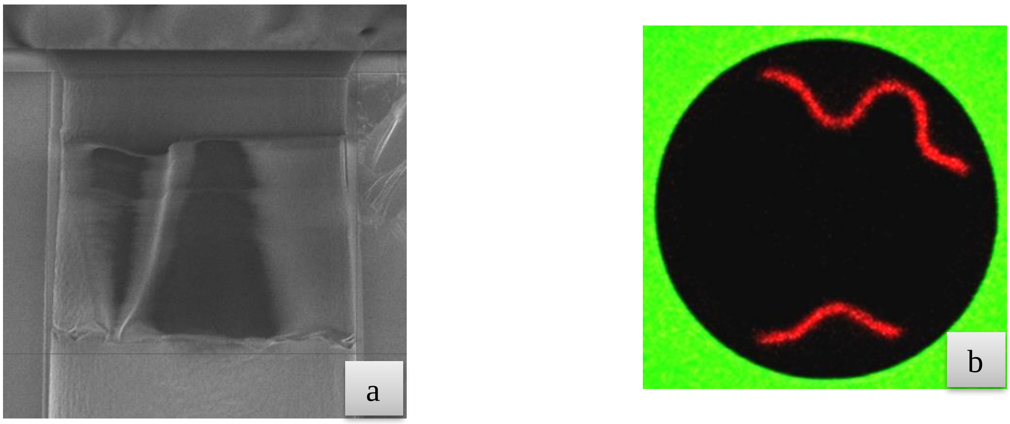

Figure 4. 17: SEM image (a), confocal laser scanned image with dry objective (b) of a TSV in cross-sectional and top down view after TSE process, AR 1:5.

Figure 4.17a depicts the upper part of a TSV, with a clearly visible partially-delaminated polymer film. Additionally, the polymer collapsed and created folds, beneath which the polymer once more appears to cover the TSV sidewall continuously. The same wafer samples are inspected under the CLSM with the following results: Figure 4.17b illustrates a fluorescence image captured in a top-down view of one TSV with an AR 1:5; the partially-delaminated sidewall polymer is clearly visible inside the TSV. The polymer sections which are in the focal plane are coloured in an intensive red, while the out-of-focus (impregnated) layers are dim.

A zoom-out on the TSV (Figure 4.17b) to an exposed area of approximately 500x500 µm demonstrates that simultaneous observation of multiple TSVs (Figure 4.18) is possible for smaller TSV diameter sizes as well. All inspected TSVs show labelled sidewall polymers, which can be clearly detected at this magnification level.

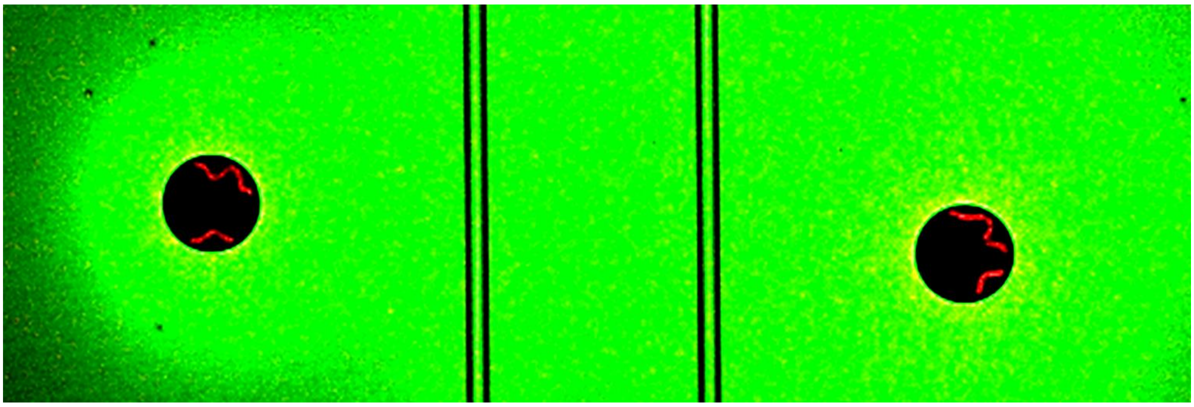

Figure 4. 18: Confocal laser scanned image of two labelled TSVs in top view after TSE step, AR 1:5.

Comparing the image captured with the CLSM using the dry objective (10x magnification; NA = 0.3, Figure 4.19b) with an image recorded using the oil immersion objective (10x magnification; NA = 1.44, see Figure 4.19b) reveals that the immersion oil objective produces sharper fluorescence images. However, the fluorescence intensity appears to be equally high for both the dry and oil objectives.

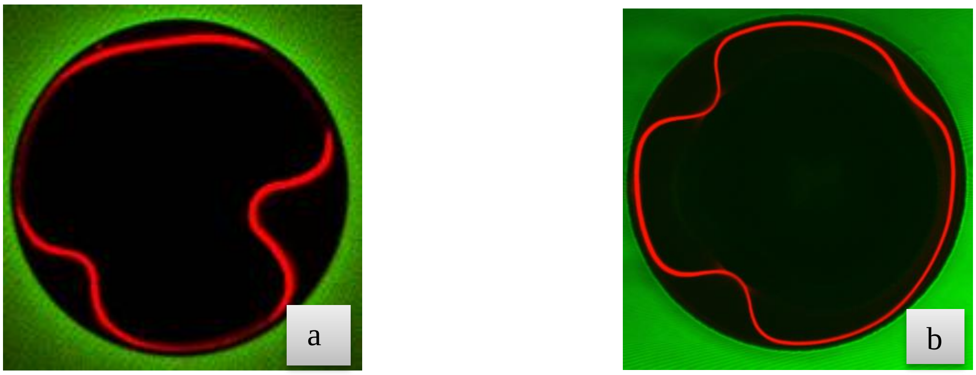

Figure 4. 19: Confocal laser scanned image with a dry (a) and an oil immersion objective (b).

In Figure 4.20 a sample with four TSVs containing labelled sidewall polymer residue is depicted. The polymer films are partially delaminated in the upper part of the TSV cylinder as the focus is set near the wafer surface. The lower part of the fluorescence image reveals polymer residue in the two right-angled trenches surrounding the TSVs. Opposite these images, the trenches above are completely dark (framed by a grey square in Figure 4.20). Notably, the labelled polymers display different fluorescence intensities (fluorescence intensity is higher in the left angled trench). This difference in intensity of the fluorescence signal can be used as indicator of the quantity of the polymer inside the trenches. The two red spots on the sample surface can be attributed to incompletely dissolved fluorophore agglomerates. In contrast to the images of the previous figures, this fluorescence image was recorded under the absence of DPSS 561 nm laser illumination.

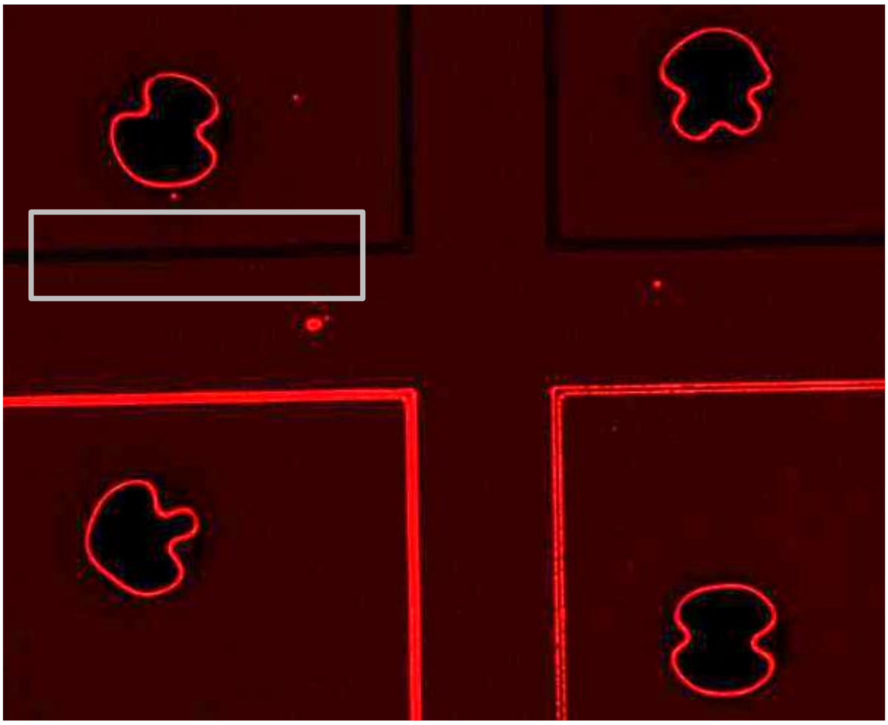

Figure 4. 20: Confocal laser scanned image of four labelled TSVs in top view after TSE step.

Figure 4.21a depicts four TSVs with labelled polymer residue. In the magnified view, one of the TSVs reveals that the polymer continuously delaminates from the TSV sidewall (Figure 4.21b). Compared to the TSVs examined so far, these polymer films are increasingly delaminating from the TSV sidewalls.

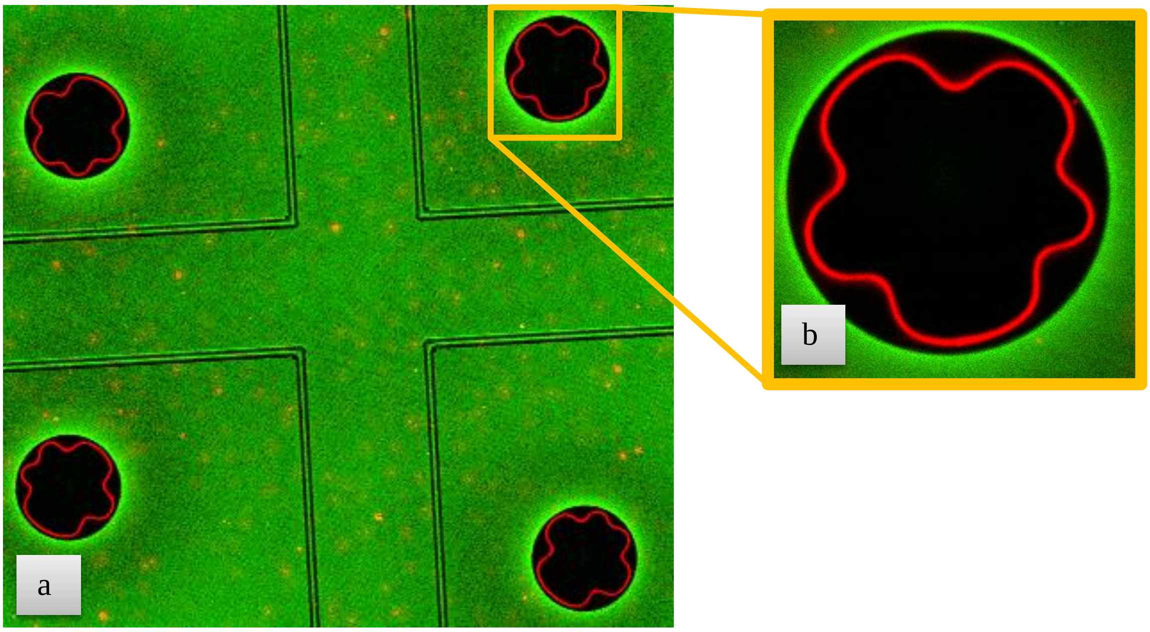

Figure 4. 21: Confocal laser scanned image of four labelled TSVs (a), magnified TSV (b) in top view after TSE process.

To give a better idea of the polymer shape and to characterize the polymer distribution inside the TSV, a cross-section of the sample has been prepared. As mentioned in chapter 2, with two pinhole apertures, the microscope has the ability to take optical thin-sections at successive focal planes, enabling a 3D reconstruction of the sample.

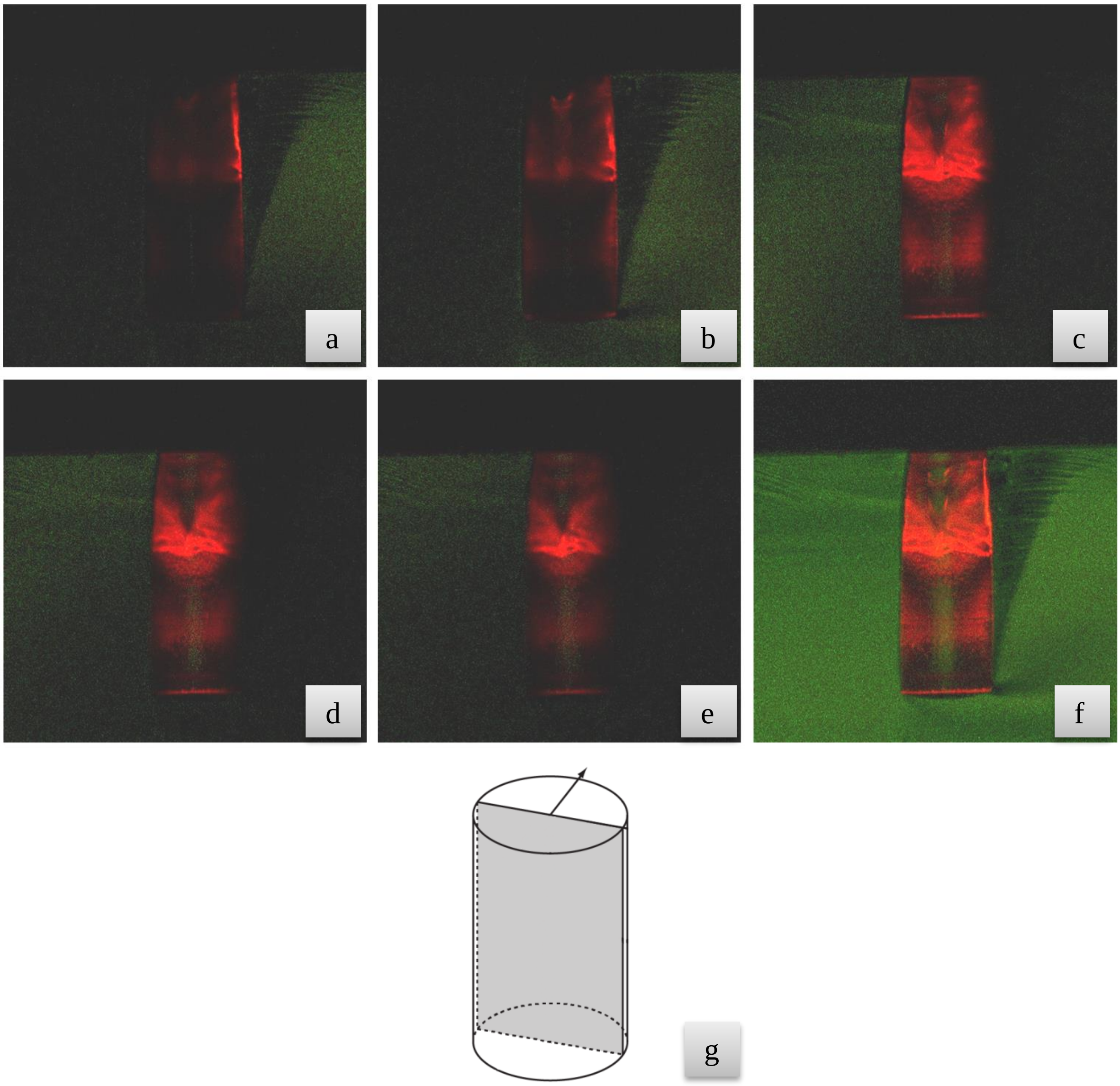

Figure 4. 22: Z-series of a TSV cross-section (a)-(f), and the scan direction (g).

Figure 4.22 depicts from a) to e) a series of images taken for a 3D reconstruction. Recording begins with the axial edge and continues focusing along the TSV sidewall to the deepest point of the TSV half-cylinder. For better understanding, Figure 4.22g represents a schematic picture of the TSV cylinder geometry and the direction of the taken optical sections. Finishing the Z-series (which are cross-sectional images of the TSV in Z-direction) recording, the software offers the possibility of choosing one of the images with the highest intensity, as can be observed in Figure 4.22f

Figure 4.22f also displays a delaminated film in the upper part of the TSV, which creates the curved-line appearance in the top-down view. The cross-sectional image can be divided into three areas. The largest accumulation of polymer appears to be in the upper third of the TSV. In this area, the polymer film collapsed, resulting in intensive red fluorescent lines. The second and the third areas are located in the lower third of the TSV. In these areas, the deposited polymers reveal a grain-like structure instead of a uniform polymer layer. The residue accumulation in the bottom exhibits a filament-like shape of the polymer. The fluorescence intensity distribution in the TSV cross-section allows for quantitative analysis of the polymer residue. A cross-sectional view enables a deeper insight into the polymer distribution and a better understanding of polymer deposition during the dry-etching process. If polymer distribution has a direct effect on the etch quality, these images will provide information for optimization of the etching process.

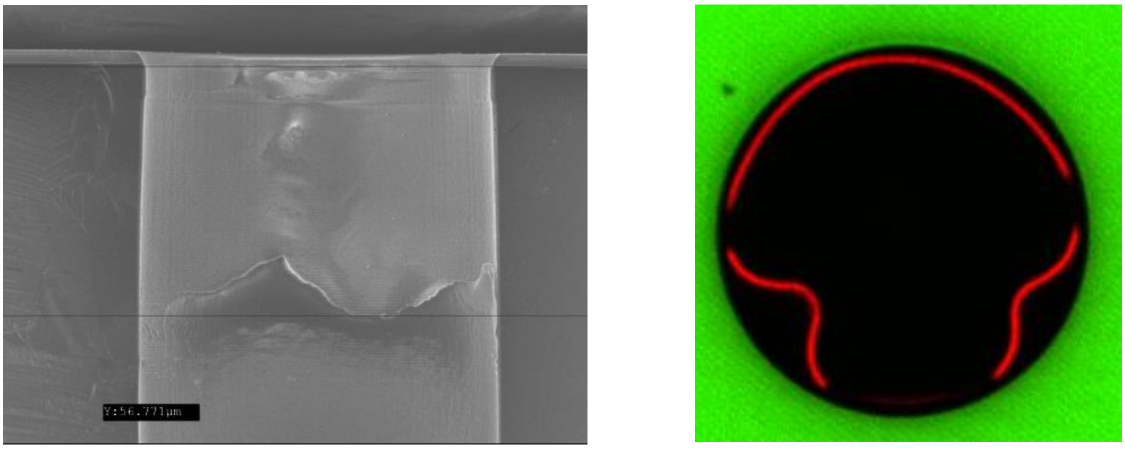

Figure 4. 23: SEM image (left) and confocal laser scanned image (right) of a twice fluorophore impregnated TSV.

Applying a second fluorophore pressure-impregnation procedure on the same sample causes a film rupture in the delaminated polymer (Figure 4.23, left image). In addition, the fluorescence images indicate a homogeneous distribution of the red colour. However, a double impregnation does not improve the fluorescence intensity (Figure 4.23, right image).

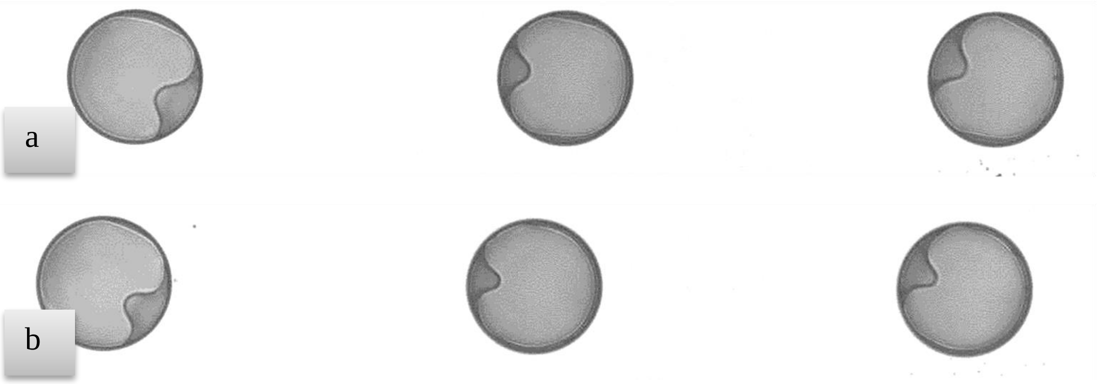

Figure 4. 24: Light microscope images of $scCO_2$ untreated (a) and treated (b) TSVs with no changes of the polymer shape and the surrounding material.

To ensure that the impregnation procedure does not change the shape of the polymer and the surrounding material, images are taken before and after the fluorophore pressure impregnation. Comparing the light microscope images where the delaminated polymer film can be observed as a curved line (Figure 4.24) before and after the impregnation, it can be observed that the polymer shape remains unchanged.

Independent variables such as impregnation duration, fluorophore concentration, and CO_2 phase states are tested for their influence on the labelling efficiency. Three solutions of high-, middle-, and low-fluorophore concentrations ($1 * 10^{-4}$ - $1 * 10^{-6}$ mol/L) have been tested in combination with CO_2 in its liquid-, critical-, and supercritical phase states. The impregnation time has been varied between 10 and 30 minutes. After impregnation in CO_2, the samples are inspected under a CLSM.

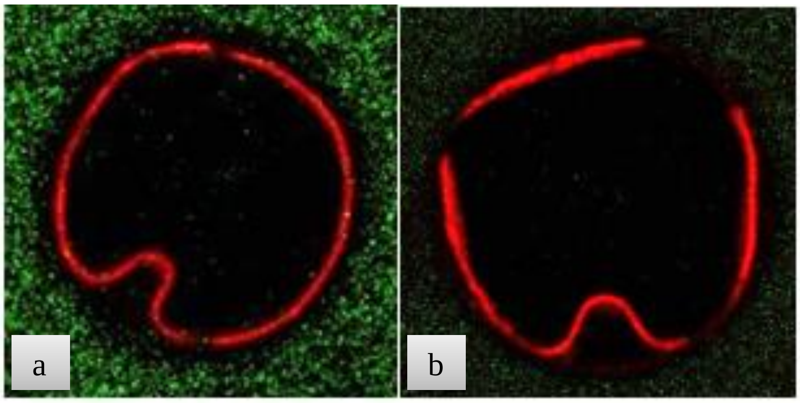

Figure 4. 25: Fluorescence images after fluorophore pressure impregnation in liquid (a) and $scCO_2$ (b).

In Figure 4.25, experimental results for the best case and worst case after a 10 minutes impregnation are depicted. The best case is assumed to be the impregnation in $scCO_2$ with a high fluorophore concentration. The worst case consequently is the impregnation in liquid CO_2 with the lowest fluorophore concentration. Image a) depicts the worst case. For this case, TSV polymer residue are fluorophore pressure-impregnated with liquid CO_2 and a low fluorophore concentration for 10 minutes. The polymer film is labelled mainly homogeneous and reveals reduced fluorescence intensity. Image b) illustrates polymer residue impregnated with $scCO_2$ and a high fluorophore concentration. The polymer film is labelled homogeneous and depicts relatively high fluorescence intensity. It can be observed that the polymer film has delaminated in several areas, so care has been taken to focus on the section with the highest amount of polymer.

Comparing the fluorescence intensities after 10 minutes indicates that the highest fluorescent signal intensities can be obtained with the combination of high fluorophore concentrations and CO_2 supercritical state conditions. Nevertheless, application of CO_2 in liquid state results in sufficiently-labelled polymer films for detection with the fluorescent microscope.

The impregnation time is extended to 20 minutes to examine how impregnation time influences the fluorescence intensity. Figure 4.26a depicts a fluorescence image taken after 20 minutes of impregnation in CO_2 at critical point (73.8bar and 31.1°C) and low fluorophore concentration. In comparison to Figure 4.26a, the fluorescence intensity increases after doubling the impregnation time and increased pressure. Figure 4.26b illustrates a labelled polymer film after 20 minutes of impregnation in liquid CO_2 with high fluorophore concentration. Comparing the intensities of image a) and image b), it can be observed that the intensity is slightly lower in case of impregnation with liquid CO_2.

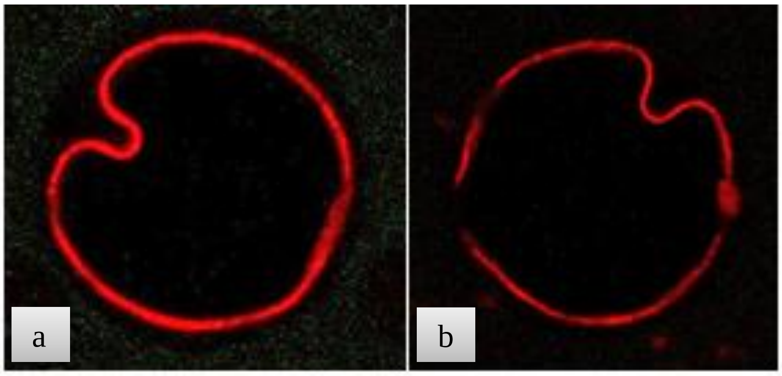

Figure 4. 26: Fluorescence images after FPI in CO_2 at the critical point (a) and in liquid CO_2 (b).

After positive evaluation of the polymer labelling and characterization method on uncleaned wafer samples, displaying a high degree of polymer residue concentration, the characterization method must be tested upon its detection limit on partially-cleaned samples. Therefore, samples with a lower degree of contamination are prepared and analysed. The semi-cleaned wafers are prepared by applying only a single wet-cleaning step subsequent to the through silicon-oxide-spacer etch (TSE) step. SEM cross-section analysis indicates that the continuous polymer film has been removed; leaving polymer remnants only in isolated spots near the TSV bottom (Figure 4.27, left). After impregnation, the partially-cleaned samples are analysed using a CLSM microscope. Zooming in on the TSV, a red spot indicates a labelled polymer residue (Figure 4.27, right).

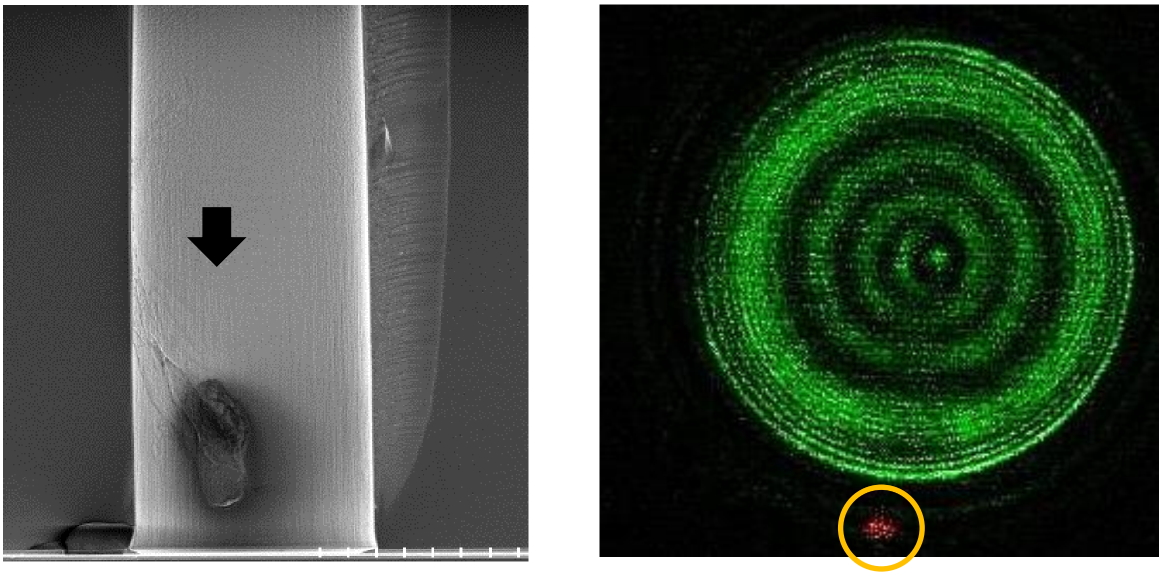

Figure 4. 27: SEM and fluorescence image of a TSV in cross-sectional (left) and top-down (right) view after TSE with a subsequent semi-cleaning step; point-shaped polymer residue.

Further partially-cleaned samples with polymer residue distributed over a larger area near the TSV bottom, as depicted in the SEM cross-section image (Figure 4.28, left image), are investigated after FPI in $scCO_2$. The yellow frame (Figure 4.28, right image) highlights the labelled polymer residue which can remain on the TSV sidewall after a partial cleaning. These two listed results successfully demonstrate that a determination of polymer residue in lower concentration can be performed using the FPI with subsequent observation under a CLSM.

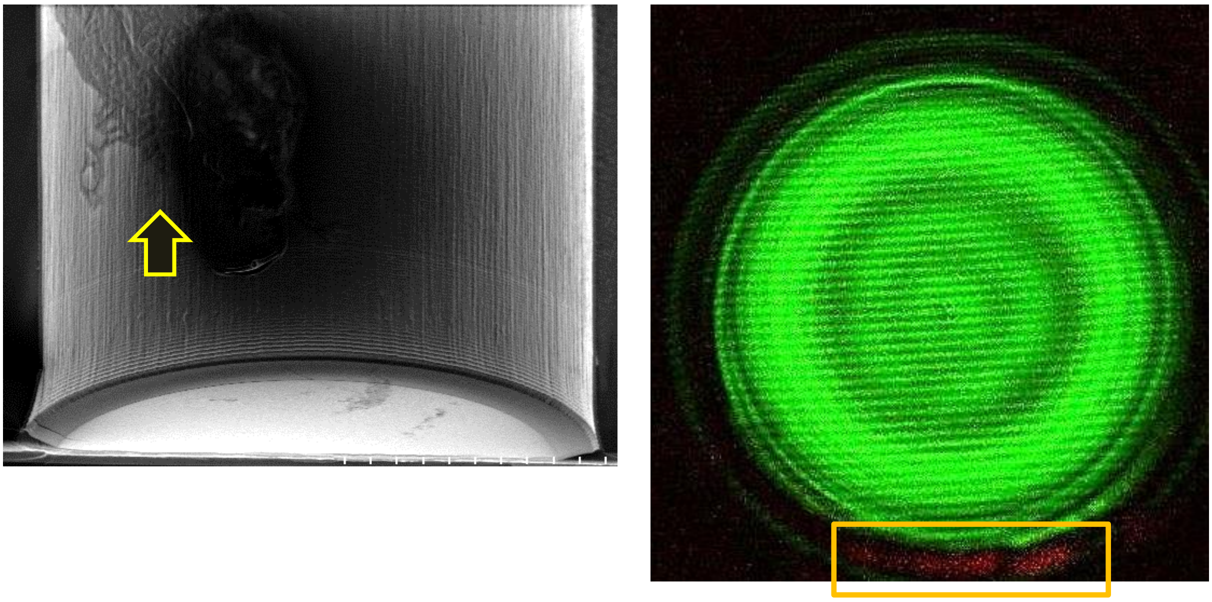

Figure 4. 28: SEM and fluorescence image of a TSV in cross-sectional and top-down view after TSE with subsequent semi-cleaning step; area-shaped polymer residue.

The following images (Figure 4.29) represent the results for FPI experiments performed in the 200-mm scale-up laboratory autoclave. The impregnation is done in liquid CO_2 at 57 bar and 25 °C, at a high fluorophore concentration. To ensure that the FPI is performed evenly over the entire wafer, two areas on the wafer have been examined under the CLSM. Images a) and b) illustrate TSVs with labelled polymers located at the edge and in the centre of the wafer as illustrated in the schematic drawing Figure 4.29 c). Comparing these two images demonstrates that the fluorescence intensities are equally high. The low fluorescence intensity results from the low impregnating pressure and low temperature. However, the polymer film is accurately represented and no fluorophores are impregnated in non-polymer material.

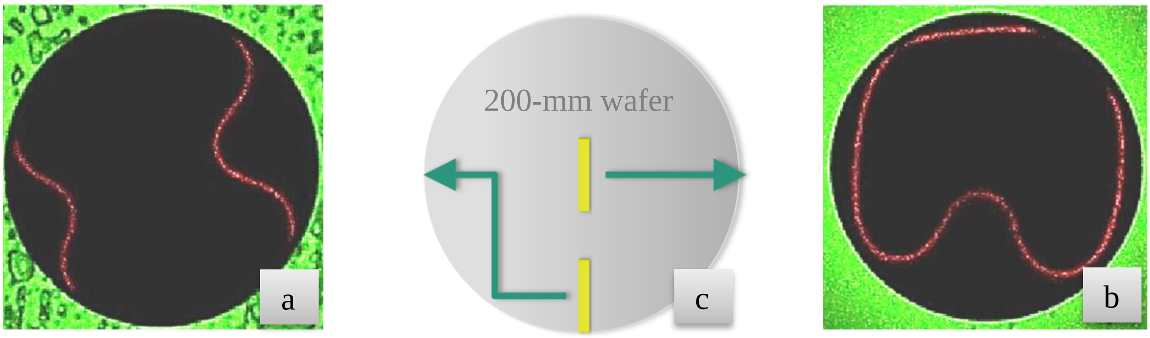

Figure 4. 29: Polymer residue after impregnation in liquid CO_2, performed in the scale-up laboratory autoclave. Image a) shows a TSV in top view located at the edge and image b) in the middle of the wafer under a CLSM, image c) depicts schematic image of a 200 mm wafer with measuring positions (marked by yellow).

Besides TSVs, different trenches with polymer residue are observed after fluorophore impregnation. After the DRIE, the wafer is cleaned in Caro´s acid (H_2SO_5). Afterwards, a passivation with a tetrafluoromethane (CF_4) precursor is performed in the dry-etching chamber. Figure 4.30 depicts the corresponding wafer mask with rectangular and cylindrical trenches with widths or respectively diameters from 5 to 150 µm.

Figure 4.31 illustrates various trenches following FPI. The deposited polymer layer is clearly visible on the wafer, particularly in areas with accumulated polymer. Since the polymer deposited after the DRIE process has a higher density, the developed FPI method can be applied to polymer labelling with high crystalline percentage.

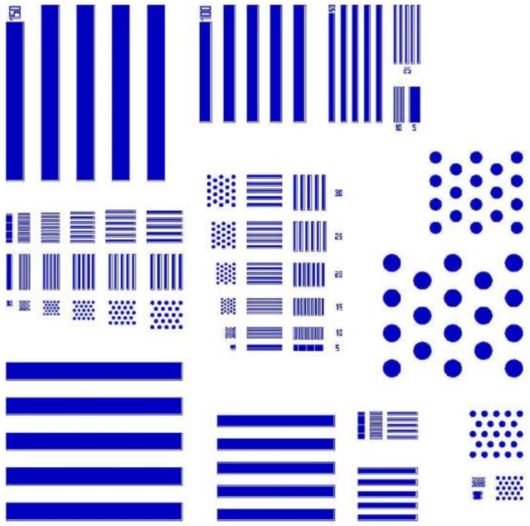

Figure 4. 30: Layout for fluorophore pressure impregnation experiments.

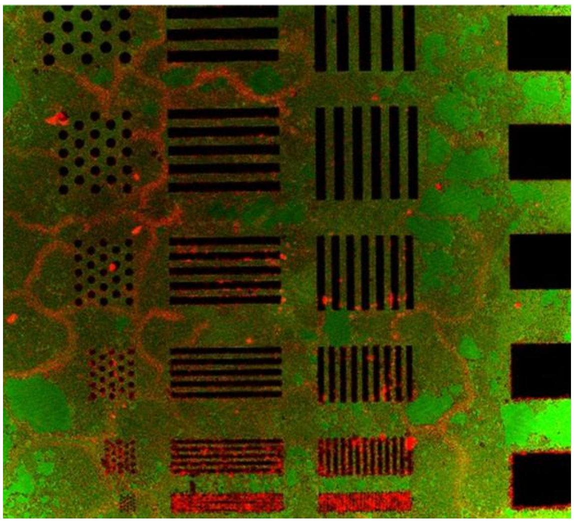

Figure 4. 31: Image of various dry-etched trenches in top view under a CLSM after FPI. Wafer background is measured in reflexion (green) and polymer residue are depicted in red.

Figure 4.32 represents a magnification of 50 µm diameter-sized cylindrical trenches in top view after FPI. As can be observed in this figure, the sidewall polymer is labelled similar to the previously demonstrated polymer residue inside the TSVs. Besides the polymer inside the TSVs, polymer fragments remaining on the wafer surface are labelled as well, as is demonstrated by the white arrow marked part.

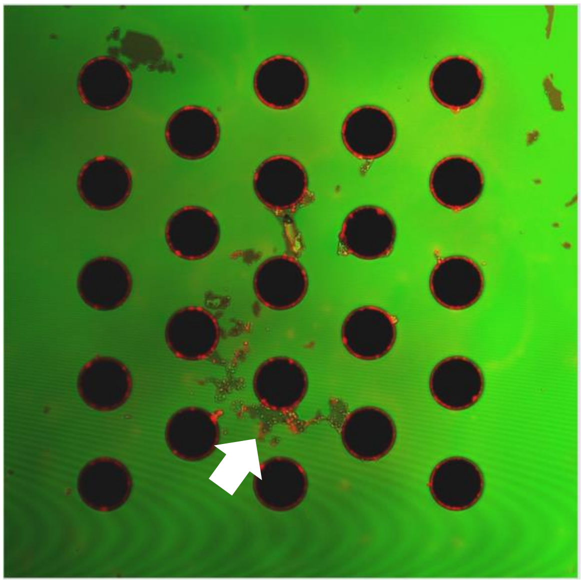

Figure 4. 32: 50 µm diameter sized TSVs in top view after FPI. Wafer background is measured in reflexion (green) and polymer residue are depicted in red.

4.3 TSV Wetting Behaviour

Different TSV sizes and TSV sidewall surface properties are tested on the wetting behaviour to improve the cleaning process, which is discussed in section 4.4. A novel method for testing surface wetting behaviour is introduced in this section. In addition, this section explores further potential reasons for non-wetting behaviour with a consequential lack of infiltration in the TSV trenches.

As mentioned in chapter 3 conventional aqueous cleaning processes apply a rinsing and drying sequence using water-based chemistries as well as IPA which make them perfect candidates as test liquids for the wetting experiments.

Table 4. 1: Contact angle measurements of DIW–SiO_2 suspension of different particle concentrations on a silicon wafer surface.

DIW-SiO_2 Suspension	
Concentration of SiO_2 particles in DIW [gr/ml]	**Contact angle [°]**
0	42.44
0.0059	44.53
0.00295	43.21

Table 4. 2: Contact angle measurements of IPA-SiO_2 suspensions of different particle concentrations on a silicon wafer surface.

IPA-SiO_2 Suspension	
Concentration of SiO_2 particles in IPA [gr/ml]	**Contact angle [°]**
0	7.26
0.00148	8.14

To eliminate possible influence on the surface tension, the contact angles of the dispersion containing DIW or IPA and SiO_2-particles with a diameter of 500nm (Monospher 500, Merck) are measured on a smooth silicon wafer. Tables 4.1 and 4.2 identify the particle concentrations in the suspension and the corresponding contact angles measured on a SiO_2 surface. For the final experiments with DIW-SiO_2, dispersion with a concentration of 0.00216 gr/ml is prepared, as this dispersion has enough monospheres for a homogeneous distribution and a contact angle with a negligibly small difference from pure DIW ($\theta_{DIW} = 42.44\,°$).

For experiments with IPA-SiO_2, a tracer concentration of 0.00216 gr/ml is selected. This concentration is also sufficient for a homogeneous distribution and differs just slightly in its surface tension from the pure IPA ($\theta_{IPA} = 7.26\,°$). Consequently, both (DIW- and IPA-based) dispersions will be considered pure liquids.

For comparison to deep TSVs, a rectangular trench with a relatively (to the TSVs) small depth is selected to demonstrate the distribution of the suspension. The SEM image (Figure 4.33) illustrates infiltration of DIW/SiO_2 monosphere dispersion in a 6-µm wide and 2-µm deep trench (AR = 3:1). Monospheres can be observed on the top and the bottom of the trench, which indicates a complete wetting of the trench.

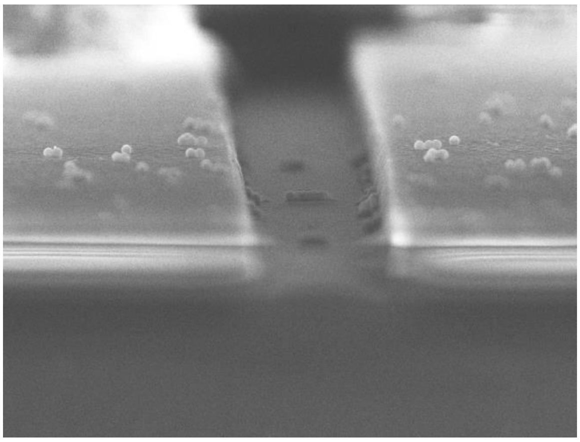

Figure 4. 33: SiO_2 monosphere dispersion on a TSE sample in 2 µm deep trench.

Besides the surface tension of the dispersions, the surface area and the contact angle between the dispersion and the surface are important. Therefore, different aspect ratios have been taken into account for the infiltration evaluation (described in section 3.2.3). The test suspensions contain DIW or IPA and 500-nm sized SiO_2 particles as dispersant.

The infiltration evaluation proceeds as follows: the wafer is immersed into the dispersion at 20 °C, and after 10 min of exposure the wafer is dried. To prevent particle contaminations, cross-section analyses of the TSVs are prepared under a cleanroom atmosphere (ISO class 4). After evaporation of the test liquid, the infiltration depth is determined by observing the remaining SiO_2 particles on the silicon sidewalls using SEM. Cross-section analyses are carried out on three locations of each wafer sample. At each site, three TSVs are examined.

The DIW-based suspension is mixed in a cleanroom plastic bag (8 L) with a tracer concentration of 0.00216 gr/ml. Two types of TSVs (Type I AR of 1:2.5; Type II AR of 1:5) of different aspect ratios and surface conditions (hydrophilic surface and hydrophobic surface) are tested. The wafers of TSV Type I are placed in a wafer holder and immersed in the test suspension. After 10 minutes of exposure, the wafers are dried under cleanroom conditions. In the second experiment, wafers of both TSV Type I and TSV Type II are placed in individual cleanroom bags filled with the IPA-based suspension (tracer concentration of 0.00216 gr/ml) for 10 minutes. In the third experiment, wafers of TSV Type I are placed in individual cleanroom bags filled with either a DIW- or IPA-based test suspension of higher tracer concentration of 0.006 gr/ml for 10 minutes.

Table 4. 3: Infiltration rate in % for DIW- and IPA-based suspensions in TSVs with AR 1:2.5 and 1:5 after selected process steps. Experimental results reveal no infiltration of DIW in TSVs with AR 1:2.5 and AR 1:5 and a hydrophobic sidewall, and incomplete infiltration in TSVs with a hydrophilic sidewall surface. Results also indicate incomplete infiltration of IPA in TSVs with AR 1:2.5 and AR 1:5.

Surface condition	**DIW**		**IPA**	
	AR 1:2.5	**AR 1:5**	**AR 1:2.5**	**AR 1:5**
hydrophobic	-	-	59	69
hydrophilic	63	41	64	66

The penetration depth is measured on three TSV cross-sections of each sample. After averaging, the value is normalized against the absolute TSV depth, which represents the infiltration rate of the suspension as a percent. In Table 4.3, the results of the infiltration evaluation are listed. A comparison between hydrophobic and hydrophilic TSV surfaces reveals a higher infiltration rate for the hydrophilic surface, except for the rate for Type II immersed in the IPA dispersion. Fluids, or in this case dispersions, have a larger contact angle on hydrophobic surfaces than on hydrophilic. Consequently, the wetting behaviour of hydrophobic surfaces is worse than that of hydrophilic surfaces. The infiltration evaluation experiments also confirm this characteristic. In comparing the dispersion media, it can be observed that the IPA-based dispersion penetrates deeper inside the TSVs.

A closer look at the infiltration rates for the two aspect ratios identifies a higher infiltration rate for smaller diameter sizes and constant immersion depths in IPA-based dispersions. Surface forces increasingly dominate with growing surface-to-volume ratios. By decreasing the diameter size with constant TSV depth, the hydrophilicity has a greater effect on the infiltration. The IPA dispersion is soaked in the TSV with a higher surface-to-volume ratio. However, the DIW-based immersion experiment reveals a more than 20 % deeper infiltration for hydrophilic TSVs with a larger diameter size. Trapped air inside the TSV trenches is considered to be responsible for this result. Air bubbles appear to inhibit contact between the fluid with relatively high surface tension and the hydrophilic TSV surface, thereby preventing the suction effect from occurring.

In summary, the highest penetration depth on TSV Type I and TSV Type II wafers has been determined for the hydrophilic surface in combination with the IPA test suspension. The infiltration rate for high surface tension suspensions is smaller than the rate for low surface tension. No infiltration was detected for the suspension with a high surface tension on the hydrophobic surface. Notably, on all TSV Type I and TSV Type II wafers a 100% infiltration of the DIW and IPA suspensions down to the bottom was not possible. These experimental results provide direct evidence that a TSV with or without polymer residue on the sidewalls can be not wetted completely by a fluid with a contact angle of more than 8 ° at ambient temperature during 10 minutes of immersion time.

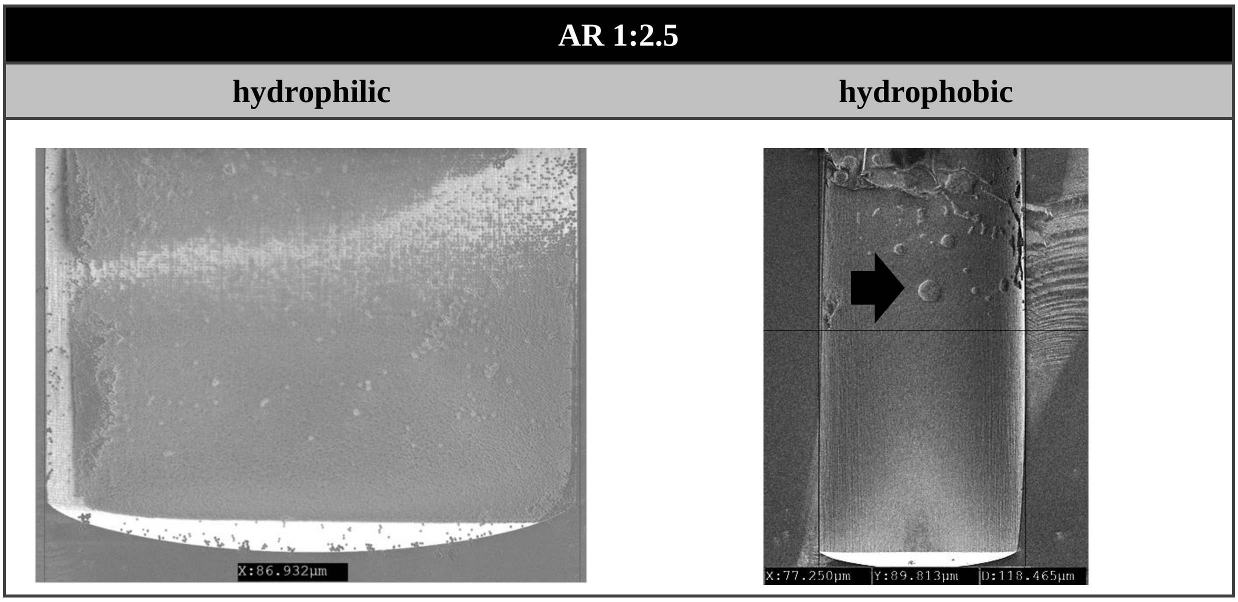

Figure 4. 34: Wetting of hydrophobic and hydrophilic TSV surfaces.

To visualize the difference between a prime wetting surface and a non-wetting surface, SEM images of hydrophilic and hydrophobic TSV structures following immersion experiments are compared (see Figure 4.34). It can be observed that the monospheres are arranged differently on these two surfaces. While on the hydrophilic surface a layer of particles is deposited nearly homogeneously over the complete area, the monospheres on the hydrophobic surface form drop-like shapes. This drop formation results from the repellent properties of the polymer, which force the suspension to shape into a structure with the smallest possible contact with the polymer, i.e., a sphere.

4.3.1 Effects of Increased Temperature and Agitation on Penetration Depth

The wetting experiments indicate that a 100% infiltration down to the bottom of the TSV structure is not possible with the sole application of static force that results from the hydrodynamic pressure. Since the complete cleaning and rinsing of the TSV structures is of great importance for their reliability, the influence of agitation on the infiltration rate is analysed. Typically, high-frequency sound waves in the ultra and megasonic range, as well as increased temperatures, are used to support wafer cleaning. In order to study the effects of increased temperature and agitation on the test suspensions' penetration depth into hydrophobic and hydrophilic TSV structures, both options are applied independently of each other.

4.3.1.1 Hydrophilic TSV Samples with AR of 1:2.5

Hydrophilic TSV samples with an AR of 1:2.5 are examined after 10 minutes of soaking at 30 °C with ultrasonic support. The cross-sectional analysis of the hydrophilic samples did not allow for an exact determination of the penetration depth after infiltration experiments that applied ultrasonic support and elevated temperature. Nevertheless, a layer of monospheres has accumulated on the bottom corner of the TSV, as can be observed on the SEM cross-sectional image (Figure 4.35a). However, what all analysed samples have in common is that no particle layers were found in the centre of the TSV bottom. In Figure 4.35b, the wetting result after 10 minutes of soaking at 60 °C are depicted. The monospheres are distributed along the sidewall down to the bottom of the TSV. The main difference in particle distribution between the hydrophilic surface samples treated with ultrasonic agitation and those soaked at an elevated temperature is a more frequent contact of the monospheres to the TSV bottom when using ultrasonic support (see Figure 4.35a).

Hydrophilic TSV with AR 1:2.5

30 °C, ultrasonic	60 °C, no agitation

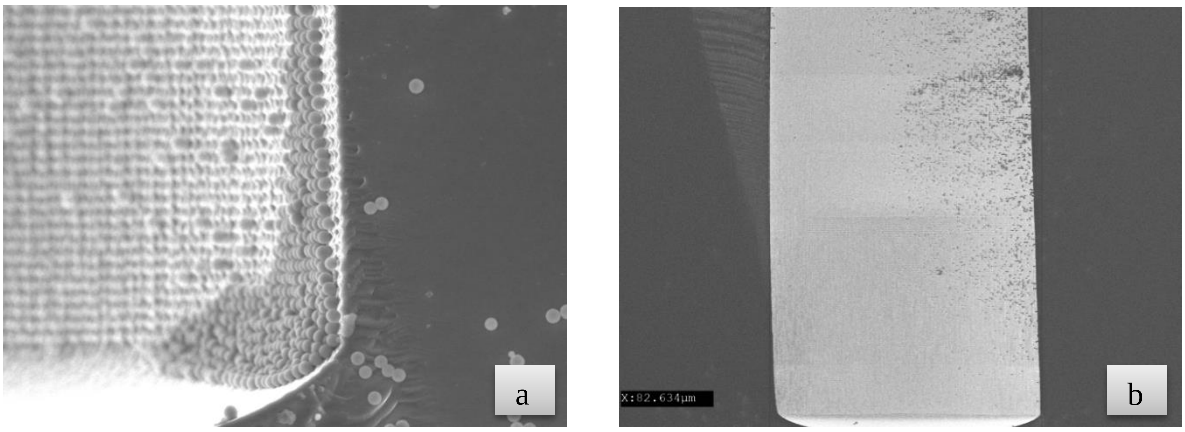

Figure 4. 35: Agitation (a) and temperature (b) supported wetting of a hydrophilic TSV surface (AR of 1:2.5).

4.3.1.2 Hydrophobic TSV Samples with AR of 1:2.5

For the hydrophobic TSV samples, which did not reveal any infiltration for either test suspension (see Table 4.3), the same process parameters have been applied. Comparing both cross-sectional images (Figure 4.36a, b), it is clearly recognizable that the areas covered with polymer residue (dark grey) are free from monospheres due to the repellent effect of the polymer surface. As mentioned before, the contact angle between water and fluoropolymers is relatively high (θ>100 °), which results in non-wetting of the surface. Areas without polymer residue are partially covered by the monospheres (black arrows) and thus have been wetted by the dispersion. The analyses of the hydrophobic TSV samples reveal that with ultrasonic agitation, a higher number of monospheres accumulate at the bottom corner of the TSV (Figure 4.36a, blue arrow) compared to the samples only soaked at an elevated temperature (Figure 4.36b).

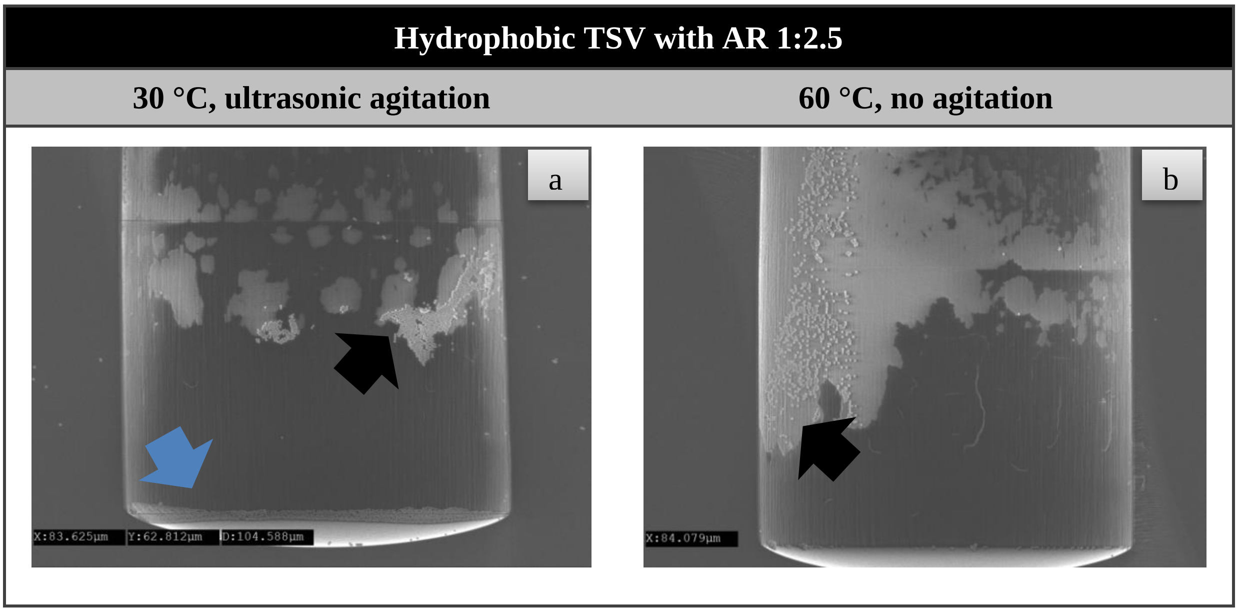

Figure 4. 36: SEM images of TSVs in cross-sectional view after infiltration evaluation experiments. Wetting of a hydrophobic TSV surface (AR of 1:2.5) was performed with ultrasonic agitation a) and temperature support b).

4.3.1.3 Hydrophilic TSV Samples with AR of 1:5

To prove and evaluate the beneficial effect of ultrasonic agitation and increased temperature on the infiltration rate of the test suspensions for smaller diameter-sized TSVs (hydrophilic and hydrophobic surfaces), the same parameter set is applied as described above for an AR of 1:2.5.

The hydrophilic TSV samples with an AR of 1:5 are examined after 10 minutes of soaking at 30 °C with ultrasonic agitation. The SEM cross-section indicates that the monospheres are arranged homogeneously on the TSV sidewall, ranging from top to bottom (Figure 4.37a). Figure 4.37b depicts the wetting result after 10 minutes of soaking at 60 °C. These monospheres are also distributed over the sidewall down to the bottom of the TSV. It can be observed that agitation induced by ultrasonic sound waves as well as increased temperature generate similar wetting results and support the penetration of liquids into TSV structures. The sidewalls indicate a relatively uniform particle distribution. In both cases, the TSV bottom is particle-free.

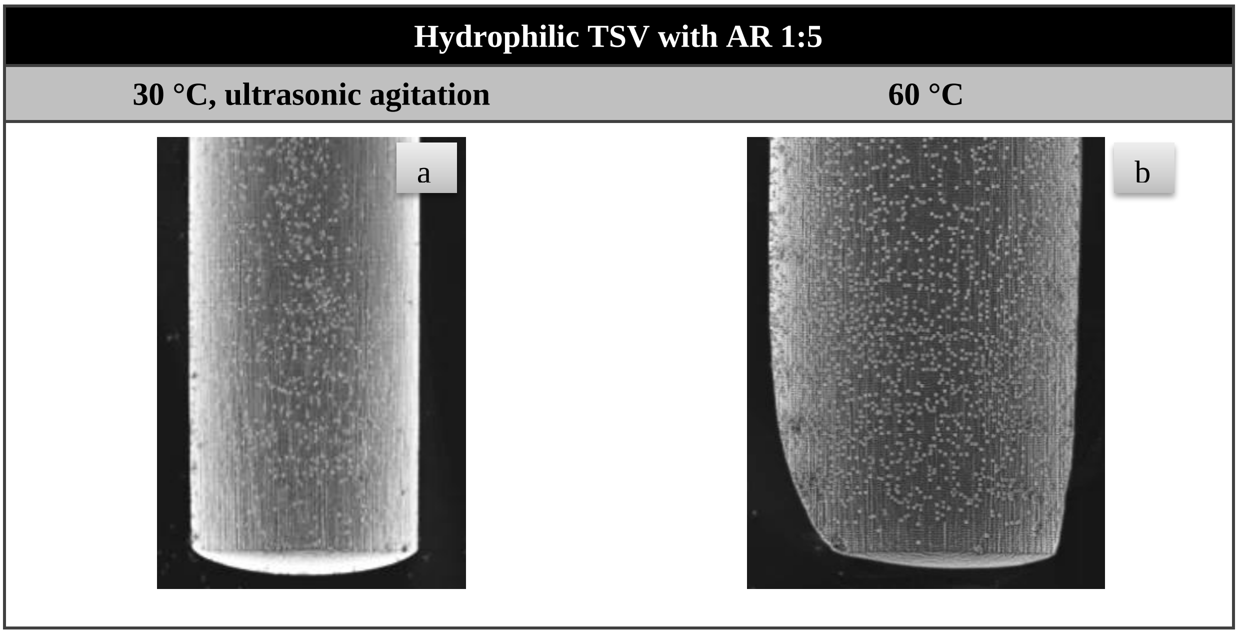

Figure 4. 37: SEM images of TSVs in cross-sectional view after infiltration evaluation experiments. Wetting of a hydrophilic TSV surface (AR of 1:5) was performed with ultrasonic agitation a) and temperature support b).

4.3.1.4 Hydrophobic TSV Samples with AR of 1:5

For the investigation of the wetting behaviour of hydrophobic TSV structures which did not reveal any infiltration for both DIW- and IPA-based suspensions, the same experiment settings are used. The SEM cross-sectional images (Figure 4.38) clearly indicate that the sidewall areas covered with polymer residue (dark grey) are free from monospheres, due to the repellent properties of the fluoropolymer residue. In case of ultrasonic agitation, more monospheres are densely packed at the TSV bottom corner (Figure 4.38a, black arrow) than in case of pure immersion at 60 °C (Figure 4.38b, black arrow). A comparison of the wetting results obtained for the different TSV aspect ratios with hydrophobic surfaces demonstrates that in total, a lower number of monospheres can be detected on the sidewall of the higher aspect ratio structures. However, the monospheres are accumulating in the bottom corner of the TSV.

Hydrophobic TSV with AR 1:5

30 °C, ultrasonic **60 °C**

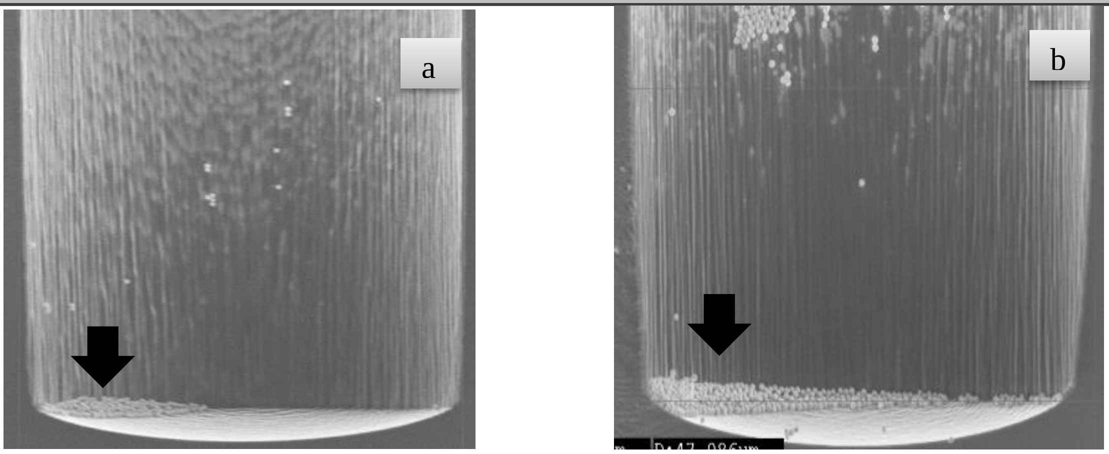

Figure 4. 38: SEM images of TSVs in cross-sectional view after infiltration evaluation experiments. Wetting of a hydrophobic TSV surface (AR of 1:5) was performed with ultrasonic agitation a) and temperature support b).

Another way to support the wetting behaviour of the surface is a pre-wetting treatment. Because of the small structural elements to be wetted, a pre-treatment in a gaseous phase can be advantageous. Saturated vapour can flow inside the TSV much more easily than a fluid. Droplets of the vapour condense on the TSV sidewall and generate a thin film. This film is able to attract the liquid due to the molecular interactions created by the hydrogen bonds. In the previous experiments, no infiltration of the hydrophobic TSV structures occurred without agitation using the DIW test suspension, regardless of the structure’s aspect ratio. For this purpose, these type of TSVs are analysed regarding their wettability behaviour change after a pre-wetting step using DIW steam. The specimen is located face-down above the DIW steam for a period of 5-10 minutes. After the infiltration test with a DIW-based dispersion, monospheres are detected in the middle of the TSV for both aspect ratios 1:2.5 and 1:5, as illustrated in Figure 4.39a, b. It also can be observed that the monospheres are gathering on a sort of plateau.

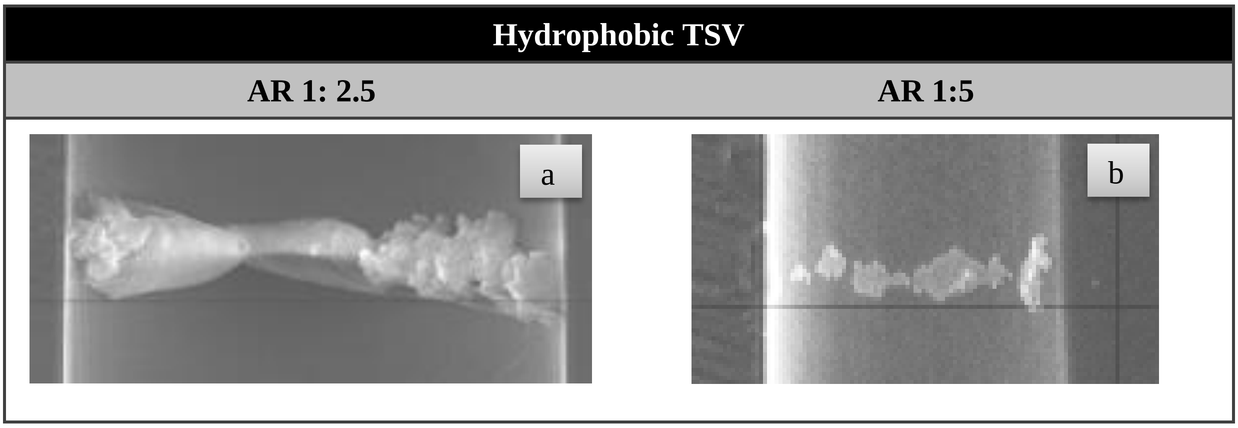

Figure 4. 39: SEM images of TSVs in cross-sectional view after a pre-wetting supported infiltration evaluation experiment on a hydrophilic TSV surface (AR of 1:2.5 and AR of 1:5).

On closer examination, an accumulation on a polymeric film protruding into the TSV centre is revealed (Figure 4.40). This strip is formed during a collapse of the film, which is depicted in Figure 4.40b where a strip is folding upwards and enclosing the monospheres. Since this strip reduces the inner diameter of the TSV, it is prone to inhibiting the infiltration of the suspension.

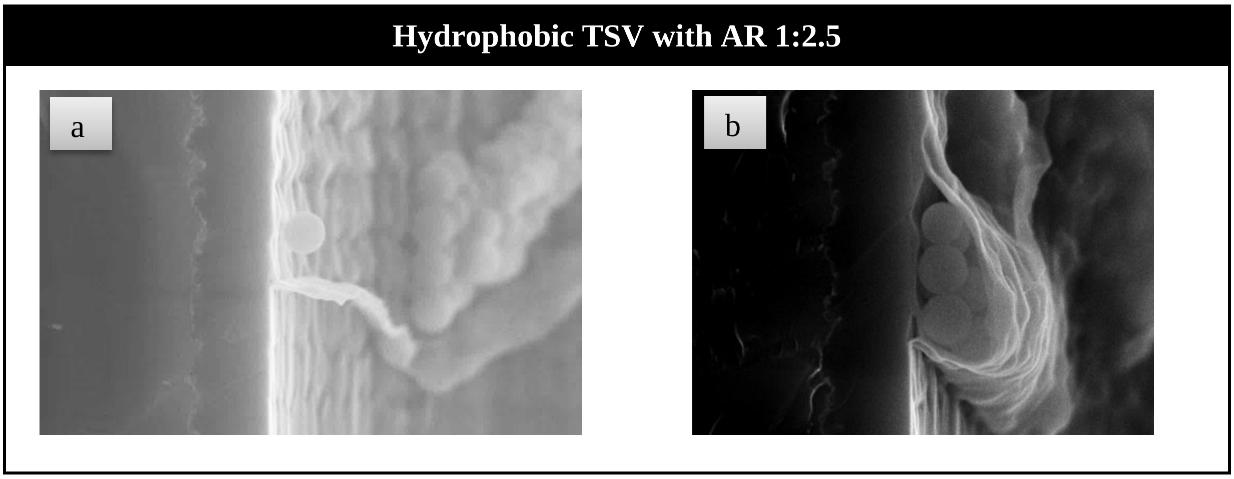

Figure 4. 40: Collapsed polymer residue film with monospheres on top (a) and with encapsulated monospheres (b).

As mentioned in section 3.2.2, it is possible to transition from the Cassie-Baxter wetting state into the Wenzel state by disturbing the thermodynamically stability of the trapped air inside the pores caused by the rough surface or inside the TSVs such as in this thesis. The experimental results indicate that pre-wetting the sidewall with saturated water vapour and ultrasonic in combination with increased temperature destabilizes the trapped air and improves the infiltration rate.

4.3.2 Effect of Trapped Air on TSV Wetting Behaviour

In order to clarify the effect of trapped air in a TSV on its wetting behaviour, an additional experiment is performed. A hydrophobic TSV is covered with a monosphere suspension, building up kind of a bridge (illustrated with a black line) as shown in Figure 4.41. The schematic drawing (Figure 4.41, right) promotes a better understanding of how a liquid (in this case, a DIW-monosphere dispersion) is arranged over the TSV (Figure 4.41, left). The dispersion wets the top edge of the TSV, as the TSV is hydrophilic and almost completely free from polymers.

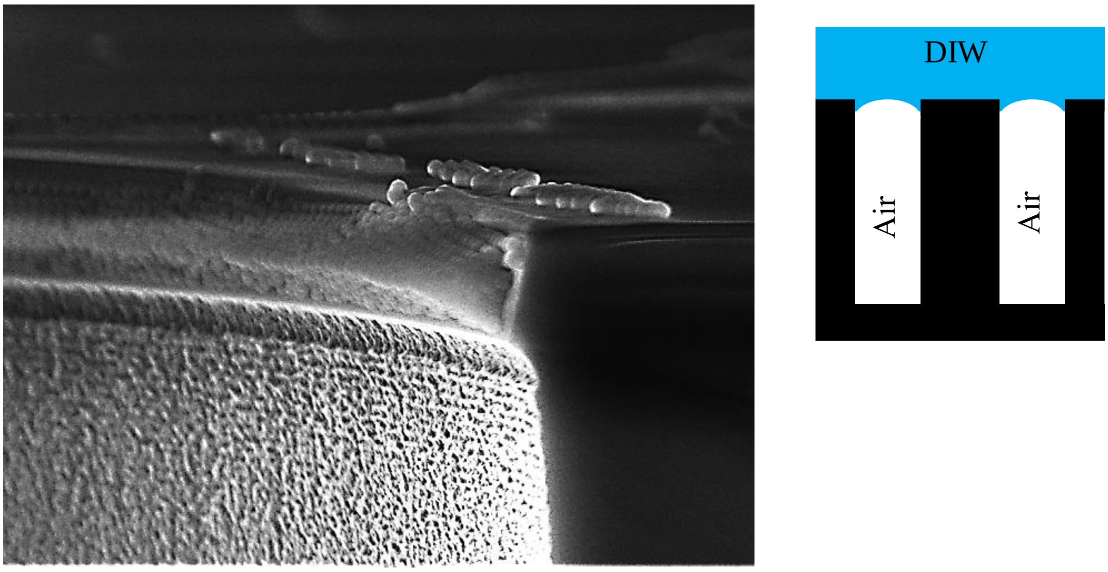

Figure 4. 41: SiO_2 monosphere dispersion on a TSE (left) and schematic image of TSVs with trapped air and immersed in DIW (right).

Using the newly-developed infiltration evaluation method, TSVs with different diameter sizes and aspect ratios and corresponding surfaces with various physico-chemical properties in combination with the wetting fluid can be investigated due to the wetting and infiltration behaviour. Moreover, this method provides a visual representation of the effect that air trapped in TSVs has on the infiltration of fluids. On the basis of the developed infiltration evaluation method, cleaning agents, cleaning processes, and cleaning tool can be reassessed and improved due to the wetting surfaces and infiltration in TSVs or, more generally, in trenches.

4.4 TSV Polymer Residue Removal

The reduced wettability of TSVs covered with repellent polymers on the sidewalls hampers the diffusion of the cleaning agent into the residue, thus likely impeding the stripping process.

To circumvent these difficulties, a pre-cleaning step using $scCO_2$ is performed. A wafer with sidewall polymer residue is placed in the pressure chamber with CO_2 in supercritical state for 15 minutes. An average temperature of 33 °C and pressure of 80 bar ensure process conditions just above the critical point of CO_2. Under pressure, $scCO_2$ diffuses like a gas into the polymer matrix (as discussed in chapter 3, 3.1.1). It is assumed that effects such as swelling, cracking, delamination, or collapse of the polymer residue will occur either individually or in combination. The CO_2 swells the polymer by diffusing into the polymer network and initiates delamination from the sidewall during the subsequent decompression. The swelling and partial delamination renders the polymer more susceptible to the attack of the cleaning agent which is applied in the subsequent stripping process.

In order to enhance infiltration of the following cleaning agent between the sidewall and the polymer, the wafers are dipped into a 2 wt% dilute HF solution for two minutes. The polymer undercut effect and subsequent delamination of the sidewall polymer caused by an HF dip has been explored in chapter 3, section 3.2.4. Since the diluted HF has a similar surface tension as water, penetration in the TSV should be limited. Therefore, the open metal layer at the bottom (if existing) will not be affected by the acid.

After the polymer layer is delaminated in the top of the TSV, a wet cleaning process using an amine-based stripping agent is performed at 65 °C for 10 minutes. Since air bubbles over TSV trenches have formed, the wet clean is repeated after a 5-minute DIW rinse, concluding with an ultrasonic-supported DIW clean of 10 minutes (Table 4.4).

Table 4. 4: Experimental cleaning parameters for TSE wafer.

Process step	Process type	Process parameters		
1	$scCO_2$- FPI	ΔT	°C	33
		Δp	bar	80
		t	min	15
2	HF Dip	c	%	2
		t	min	2
3	WET clean	T	°C	65
		t	min	10
	DIW rinse	t	min	5
	WET clean	T	°C	65
		t	min	10
	DIW US clean	t	min	10

The procedure described in Table 4.4 has been applied to TSV structures of two different aspect ratios, namely 1:2.5 and 1:5. The TSV with the lower aspect ratio displays a sidewall polymer layer of approximately 0.4 µm thickness after TSE processing. The layers can be clearly identified as a dark grey coating on top of the scalloped SiO_2 isolation layer (Figure 4.42a). The right image (Figure 4.42b) depicts the TSV bottom corner after application of the cleaning sequence outlined in Table 4.4. As can be observed in the cross-sectional view, the polymer film ④ on the sidewall (Figure 4.42a) has been completely removed (Figure 4.42b).

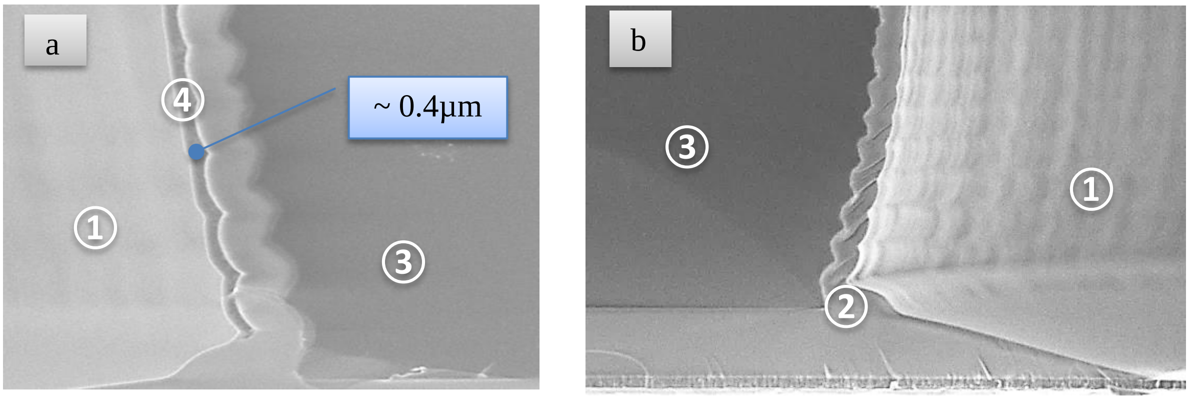

Figure 4. 42: TSV bottom with an AR of 1:2.5 in a cross-sectional view before (a) and after (b) the cleaning process based on a $scCO_2$ pre-clean. ① TSV inside, ② oxide, ③ silicon, ④ sidewall polymer.

The sidewall polymer layer ④ of the higher aspect ratio TSV is measured to approximately 0.13 µm (Figure 4.43a). After the cleaning sequence, there are no indications of a polymer layer remaining on the sidewall (Figure 4.43b).

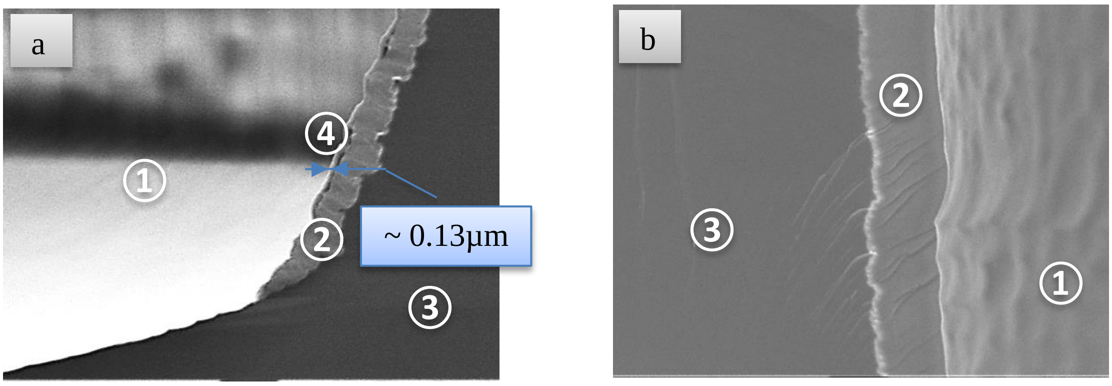

Figure 4. 43: TSV bottom with an AR of 1:5 in a cross-sectional view before (a) and after (b) the cleaning process based on a $scCO_2$ pre-clean. ① TSV inside, ② oxide, ③ silicon, ④ sidewall polymer.

Based on the experimental results, improved cleaning results can be achieved by using $scCO_2$ as a pre-cleaning step. An HF dip supports the sidewall polymer delamination, permitting the cleaning agent to penetrate the interface between the sidewall and the polymer residue. A regular wet cleaning agent dissolves the polymer residue. The improved cleaning process decreases the cleaning time and the volume of the cleaning agent, while both are interdependent.

Chapter 5 Conclusion and Outlook

This thesis introduced a newly-developed method for non-destructive inspection of TSVs with decreasing diameter sizes and increasing aspect ratios. Experimental results prove that smallest quantity of sidewall polymer residue in TSVs and other trench geometries can be detected under a confocal laser scanning microscope (CLSM) after the newly-developed method of fluorophore pressure impregnation (FPI). Depending on the size, several TSVs and trenches can be observed at once, before the labelled polymer residue can be precisely localized on the sidewall using the Z-reconstruction detection setting. A CLSM's additional reflection measuring improves the contrast of the red fluorescent labelled polymer, but also provides additional information due to sidewall roughness and possible surface damages. The laboratory autoclave developed for the FPI purpose provides the option to impregnate wafer specimens up to 200-mm in diameter within a short time under exclusion of strong chemicals.

The experimental results indicate that an impregnation of a fluorophore (ATTO 647N) in a PTFE-like polymer residue is possible using CO_2 in liquid or supercritical state. Emitted fluorescent light can be detected by the CLSM, generating an image of the scanned sample surface. Appropriate microscope settings make it possible to examine the labelled polymer matrix inside the TSVs with different aspect ratios. The intensity of the fluorescent light as well as the lateral and axial resolution is increased by heeding certain factors. By setting the pinhole aperture to the smallest possible diameter, the amount of light created as a result of laser excitation of the fluorophore is decreased, while at the same time the fluorescence intensity is increased. Zooming into the area of interest as well as accelerating the laser power increases both the fluorescence intensity and the spatial resolution, but also causes rapid photobleaching of the fluorophore. In comparison to the dry objective, an oil immersion objective provides sharper fluorescence images of the labelled polymer.

Independent variables such as impregnation duration, fluorophore concentration, and CO_2 phase states are tested for their influence on the labelling efficiency. Three solutions of high, middle, and low fluorophore concentrations are tested in combination with CO_2 in liquid, critical, and supercritical phase states. Comparing the fluorescence intensities demonstrates that the highest fluorescent signal intensities could be obtained with the combination of high fluorophore concentrations and supercritical state impregnation. Nevertheless, application of CO_2 in liquid state results in sufficiently-labelled polymer films for detection with the CLSM. Furthermore, with extended impregnation duration, the resulting fluorescence intensity increases when applying $scCO_2$.

It was demonstrated that delamination of a polymer film from the TSV sidewall becomes visible in the top-down view. Cross-sectional analysis of labelled TSV samples provides additional information about the distribution of the polymer residue inside the TSV after DRIE. The cross-sectional view reveals an accumulation of polymer residue in the bottom, with the highest concentration in the upper third of the TSV. Furthermore, following the through-spacer-oxide etching step (TSE), certain TSVs reveal delamination and collapse of the film in the upper third. In the present work, it is therefore demonstrated that fluoropolymers currently used for TSV formation and photoresists used in photolithography can be detected with a labelling method based on fluorescence microscopy.

To lower material costs, further fluorophore types and concentrations should be investigated in the future. The possibility of fluorophore pressure impregnation in liquid or at the critical point of CO_2 instead of $scCO_2$ should also be studied in further experiments with the aim of reducing process costs. If only information regarding polymer residue incidence is required, a dark-field microscope, which is cheaper and simpler in design than a CLSM, should be considered. To extend the FPI method to a standard wafer reception control, areas of inspection on the full-sized wafer in the form of wafer-mapping should be defined to minimize examination time. Besides the TSV depth and the sidewall roughness, information about polymer distribution on the TSV sidewalls during the etching process can be used for etch process optimization. This information can also be included in the package of data generated during wafer-mapping for the evaluation of equipment and manufacturing operations. Outside the semiconductor fabrication plant, fluorophore-labelled Teflon-like polymers on wafers with different trench sizes and geometries are particularly suitable for the evaluation of newly-developed cleaning agents, sequences, and tools.

Before establishing a theory about a new cleaning methodology for TSVs after TSE, preliminary investigations according to TSV surface physics have been performed. Since the new cleaning method remains a wet-chemical process, the most important factor for successful cleaning is the wetting behaviour of the TSV wafer in combination with the cleaning agent. The wetting behaviour of a surface is defined by the contact angle built up between the smooth solid surface, the environmental gas, and the liquid drop set on the surface. In contrast to contact angle measurements on smooth surfaces, taking a measurement on or inside a high-aspect-ratio topography structure such as a TSV is not possible. To overcome this bottleneck, an alternative method for verification of the wetting behaviour has been developed. In a first step, test liquids with well-known contact angles on silicon have been selected. In a second step, this liquid has been combined with a tracer (SiO_2 monospheres) of similar surface tension to create a test suspension, enabling the visual analysis of the infiltration rate into trenches. Because the majority of cleaning solutions are water-based, and IPA is frequently used in wafer rinsing and drying processes, water and IPA have been selected as test liquids. In addition to various TSV aspect ratios, different polymer contamination degrees have also been taken into account for the infiltration tests.

Cross-section analyses demonstrated on the one hand high penetration depth of a test suspension based on a fluid with a low surface tension in TSVs with a hydrophilic surface. On the other hand, no infiltration was detected for a test dispersion based on a fluid with high surface tension in the hydrophobic TSV surface. Notably, on all TSV types, a 100% infiltration of both dispersions down to the bottom was not possible. The wetting experiments confirmed the Cassie-Baxter theory applied to rough surfaces, trapping air in the roughness asperities, which resulted in an incomplete surface wetting behaviour. However, a transition from the Cassie-Baxter state to the Wenzel state has been achieved by adding a thermodynamic destabilisation of the captured air inside the TSV in terms of ultrasonic agitation, increase in enthalpy, and pre-wetting of the TSV surface.

The reduced wettability of TSVs covered with repellent polymers on the sidewalls hampers the diffusion of the cleaning agent into the residue, thus impeding the stripping process. On the basis of these results, it is evident that a TSV infiltration cannot be achieved without support either by temperature-affected or mechanical agitation. This leads to the assumption that wet cleaning of TSV with decreasing diameter sizes and increasing aspect ratios is nearing its end.

To avoid these difficulties, a pre-treatment step using $scCO_2$ has been performed. Since $scCO_2$ diffuses into the polymer matrix, a delamination of the polymer from the TSV sidewall can be encouraged. Furthermore, the newly-developed TSV wafer cleaning method applies a polymer undercut step, adding diluted HF for further sidewall polymer delamination. This delamination permits the cleaning agent to penetrate between the TSV sidewall polymer and the TSV sidewall. This penetration increases the contact surface of the cleaning agent, thus encouraging rupture and lifting of the polymer film.

Further experiments on CO_2 pre-cleaning should be performed, using different aggregate states, process temperatures, or liquid additives in CO_2 medium. In particular, switching between the CO_2 aggregate states during pre-cleaning should be considered. Based on the achieved results in the field of post-etch cleaning, future research should concentrate on reduction of the wet cleaning steps and agents until they are completely eliminated. To lower the cleaning time, the TSV pre-treatment with $scCO_2$ should be further enhanced by raising the process temperature and pressure. However, in the long term, wet cleaning should be preferably replaced by a CO_2-based cleaning.

On the basis of the results obtained from the newly-developed infiltration evaluation method the influence of liquid-solid interface properties like hydrophilicity or hydrophobicity, trench sizes or aspect ratios and trapped air inside the trenches can be visualized. With this method cleaning agents, cleaning tools and not least cleaning sequences can be evaluated and improved for complete infiltration of the cleaning agent, which is absolutely essential for a successful polymer residue stripping.

Acknowledgement

In the first place my thanks go to my PhD supervisor Prof. Lothar Pfitzner for his scientific work and methodical support throughout the editing process of my Dissertation.

In addition, my thanks go to Dr. Markus Pfeffer, Dr. Franz Schrank, Dr. Thomas Bodner of *ams AG*, who made this work possible in the first place and always assisted and supported me in the processing through targeted discussions and ongoing support.

I am grateful to all employees of *Fraunhofer Institute IISB*, as well as to all those involved in my studies, for the good and numerous support as well as the constructive and pleasant cooperation.

Especially at this point I would like to thank my family and my husband, for the tireless strengthening and motivation as well as for the always open ear for my thoughts.

References

[1] S. I. Association, *International Technology Roadmap for Semiconducturs,* 2013 Edition.

[2] B. Bonavoglia, G. Stort, M. Morbidelli, A. Rajendran and M. Mazzotti, “sorption and swelling of semicrystalline polymers in supercritical CO2,” Wiley, Switzerland, 2006.

[3] G. E. Moore and L. FELLOW, “Cramming More Components onto Integrated Circuits,” *IEEE,* vol. VOL. 86, no. NO.1, 1998.

[4] D. C. Brock and G. E. Moore, *Understanding Moore's Law: Four Decades of Innovation,* Philadelphia, Pennsylvania: Chemical Heritage Press, 2006.

[5] L. Dignan, “IBM Research builds functional 7nm processor,” *ZDNet,* 9 July 2015.

[6] C. Wong, “Next big future,” 26 February 2019. [Online]. Available: https://www.nextbigfuture.com/2019/02/the-end-of-moores-law-in-detail-and-starting-a-new-golden-age.html. [Accessed 14 Mai 2019].

[7] M. M. Waldrop, “The chips are down for Moore’s law,” *nature,* 9 February 2016.

[8] G. Q. Zhang and A. Roosmalen, “The Changing Landscape,” in *More than Moore: Creating High Value Micro/Nanoelectronics Systems,* Springer, 2009, p. 10.

[9] C. S. Tan, R. J. Gutmann and L. R. Reif, in *Wafer Level 3-D ICs Process Technology,* Springer, 2008.

[10] S. William, “Semiconductive wafer and method of making the same”. USA Patent US3044909 A, 23 October 1958.

[11] J. Happich, “3D TSV chip market to grow more than 10 times faster than the global semiconductor industry, says Yole Développement,” *EE Times europe,* 26 July 2012.

[12] Yole developpement, “3D TSV technologies are essential for the development of heterogeneous interconnection, high end memory and performance applications,” *Yole Developpement,* 5 October 2016.

[13] Q. T. Le, G. Vereecke, H. Struyf, E. Kesters and M. R. Baklanov, “Wet Clean Application in Porous Low-k Patterning Process,” in *Advanced Interconnects for ULSI Technology,* Wiley, 2012.

[14] C. XPS, “www.casaxps.com,” 2016. [Online]. Available: http://www.casaxps.com/help_manual/casaxps2316_manual/xps_spectra.pdf. [Accessed 8 February 2017].

[15] O. Schneider, G. O. Ilevbare, J. R. Scully and R. G. Kelly, “Confocal Laser Scanning Microscopy as a Tool for In Situ Monitoring of Corrosion Underneath Organic Coatings,” ECS, 2001.

[16] www.hi.helsinki.fi, “Confocal Microscopy tutorial,” Helsinki Finland, 2004.

[17] Leica, “Leica TCS SP8 – Confocal Platform,” 2015.

[18] S. M., H. J. and E. J., Handbook of Fluorescence Spectroscopy and Imaging, Germany: Willey-VCH, 2011.

[19] J. Albani, Structure and Dynamics of Macromolecules, UK: Elsevier, 2004.

[20] Q. Zheng and S. C. Blanchard, “Single Fluorophore Photobleaching,” in *Encyclopedia of Biophysics,* Springer, 2013, pp. 2324-2326.

[21] M. Abramowitz and M. W. Davidson, “olympus microscopy resource center,” olympus, 2012. [Online]. Available: http://www.olympusmicro.com/primer/anatomy/numaperture.html. [Accessed 8 February 2017].

[22] J. Jonkman and C. M. Brown, “Any Way You Slice It—A Comparison of Confocal Microscopy Techniques,” *J Biomol Tech,* pp. 54-65, 19 Mar 2015.

[23] University of Zurich, “Leica SP5 Operating Manual,” Zurich.

[24] K. R. Spring, J. C. Russ and M. W. Davidson, *Basic Properties of Digital Images,* 2016.

[25] A. S. F. Lärmer, “Verfahren zum anisotropen Ätzen von Silicium”. Germany Patent DE4241045, 5 December 1992.

[26] F. Laermer and A. Urban, “Through-Silicon Vias Using Bosch DRIE Process Technology,” in *Ultra-thin Chip Technologies and Applications*, New York, Springer, 2011, pp. 81-92.

[27] P. Garrou, M. Koyanagi and P. Ramm, Handbook of 3D Integration, Volume 3: 3D Process Technology, Germany: Wiley, 2014.

[28] X. Li, X. Hua, L. Ling and G. S. Oehrlein, “Fluorocarbon-based plasma etching of SiO2: Comparison of C4F6/Ar and C4F8/Ar discharges,” *American Vacuum Society,* 3 September 2002.

[29] J. W. Butterbaugh, D. C. Gray and H. H. Sawin, “Plasma-surface interactions in fluorocarbon etching of silicon dioxide,” *J. Vac. Sci. Technol.,* pp. 146-147, May/Jun 1991.

[30] R. d`Agostino, *J. Appl. Phys.,* p. 52, 1981.

[31] R. Shishoo, Plasma technologies for textiles, Cambridge: CRC Press, 2007.

[32] T. F. Tadros, Applied Surfactants: Principles and Applications, Germany: Wiley, 2005.

[33] R. Massey, N. Wood and J. Huang, “Developments in Fine Line Resist Stripping,” *The PCB Magazine,* pp. 12-24, April 2013.

[34] W. M. Lee and J. Cullen, “A proven sub-micron photoresist stripper solution for post metal via hole processes”.*Contact Metallization and Multilevel Metalization, Volume 93-25.*

[35] R. Sherman, “Carbon Dioxide Snow Cleaning,” in *Developments in Surface Contamination and Cleaning. Fundamentals and Applied Aspects,* New York, William Andrew Publishing, 2008, pp. 987-1012.

[36] R. Sherman, “Cleaning with carbon dioxide snow,” in *Handbook for Critical Cleaning. Cleaning Agents and Systems, vol. 1,* FL, CRC Press, 2011, pp. 397-410.

[37] R. Kohli, “Precision cleaning and processing in industrial applications,” in *Particles on Surfaces 5&6: Detection, Adhesion and Removal*, The Netherlands, VSP, 1999, pp. 117-

133.

[38] A. F. M. Leenaars, J. A. M. Huethorst and J. J. V. Oekel, “Marangoni drying: A new extremely clean drying process,” Langmuir, Netherlands, 1990.

[39] A. Pacco, M. Wada, T. Bearda and P. W. Mertens, “Drying of High Aspect Ratio Structures: A Comparison of Drying Techniques via Electrical Stiction Analysis,” *Solid State Phenom,* pp. 145-146, 2009.

[40] D. L. Goldfarb, J. J. de Pablo, P. Nearly, J. P. Simons, W. M. Moreau and M. Angelopoulos, “Aqueous-Based Photoresist Drying Using Supercritical Carbon Dioxide to Precent Pattern Collapse,” *J. Vac. Sci. Technol.,* 2000.

[41] K. Saga and T. Hattori, “Wafer Cleaning Using Supercritical CO2 in Semiconductor and Nanoelectronic Device Fabrication,” *Solid State Phenom. 134, 97* , 2008.

[42] “Multiple papers on scCO2 cleaning,” *Solid State Phenomena Vol. 92* , 2003.

[43] “Multiple papers on scCO2 cleaning,” *Proc. First International Surface Cleaning Workshop,* pp. 214-289, November 2002.

[44] W. H. Mullee, M. A. Biberger and P. Schilling, “Removal of photoresist and residue from substrate using supercritical carbon dioxide process related applications”. Patent WO Patent 2001/033613., 2001.

[45] J. M. DeSimone, T. Romack, B. E. Betts and J. B. McClain, “Cleaning process using carbon dioxide as a solvent and employing molecularly engineered surfactants”. USA Patent US Patent 5783082, 1998.

[46] P. V. Gadkari and M. Balaraman, “Solubility of caffeine from green tea in supercritical CO2: a theoretical and empirical approach,” *PMC,* pp. 8004-8013, 1 Aug 2015.

[47] W. Steffen, U. Scherf, L. Berger, J. Kadam, A. Schlewing and R. Güntner, “Polymerization in supercritical carbon dioxide: Surfactants, micelle formation, and heterophase polymerization,” in *Supercritical Fluids as Solvents and Reaction Media,* Elsevier, 2004, pp. 533-558.

[48] M. J. Meziani, P. Pathak and S. Ya-Ping, “Supercritical Carbon Dioxide in Semiconductor Cleaning,” in *Handbook of Semiconductor Manufacturing Technology, Second Edition*, NY, CRC Press, 2008, pp. 1-21.

[49] Vopak; Antony Veder, “KNOWLEDGE SHARING REPORT–CO2 Liquid Logistics Shipping Concept (LLSC),” 2011.

[50] S. M. Burkinshaw, “Non-aqueous Dyeing,” in *Physico-chemical Aspects of Textile Coloration*, UK, Wiley, 2015, pp. 571-594.

[51] E. Szekely, *What is a supercritical fluid?*, Budapest University of Technology and Economics, 2014.

[52] A. Sehgal, “Making supercritical CO2 cleaning work: Proper selection of co-solvents and other issues,” in *Cleaning Technology in Semiconductor Device Manufacturing VIII: Proceedings of the International Symposium*, 2003, p. 215.

[53] C. D. Wood, J. C. Yarbrough, G. Roberts and J. M. DeSimone, “Production of Fluoropolymer in Supercritical Carbon Dioxide,” in *Supercritical Carbon Dioxide: In Polymer Reaction Engineering*, Germany, Wiley, 2005, pp. 189-203.

[54] K. Wynne, S. Shenoy, S. Ire and Y. Ohsaka, “Fluoropolymer-carbon dioxide compositions and methods of processing fluoropolymers”. US Patent US6960633 B2, 1 Nov 2005.

[55] A. Jimenez, G. L. Thompson, M. A. Matthews, T. A. Davis, K. Crocker, J. S. Lyons and A. Trapotsis, “Compatibility of Medical-Grade Polymers with Dense CO2,” *J Supercrit Fluids*, pp. 366-372, 1 Oct 2007.

[56] J. F. Shackelford, *Introduction to Materials Science for Engineers, 5th Ed*, NY: McGraw-Hill, 200.

[57] Y. Yuan and T. R. Lee, “Contact Angle and Wetting Properties,” in *Surface Science Techniques*, Germany, Springer, 2013, pp. 3-33.

[58] A. M. Nilsson, R. J. Daniello and J. P. Rothstein, “A novel and inexpensive technique for creating superhydrophobic surfaces using Teflon and sandpaper,” *JOURNAL OF*

PHYSICS, 12 January 2010.

[59] F. Zhanga, M. G. Kibriaa, K. Cormierb and H. M. M. R., “Surface and Interface Characterization of Sequentially Plasma Activated Silicon, Silicon dioxide and Germanium Wafers for Low Temperature Bonding Applications,” *ECS Transactions*, pp. 329-338, 2012.

[60] X. Zhou, L. Che, Z. Wang, S. Liang and X. Meng, “Development of cell microarray by using superhydrophilic silicon dioxide nano structure,” *Nanotechnology (IEEE-NANO),* 24 November 2016.

[61] K. Othmer, *Encyclopedia of Chemical Technology. 4th ed. Volumes 1,* NY: Wiley, 1994.

[62] T. Fukushima, T. Konno, E. Iwata, R. Kobayashi, T. Kojima and M. Murugesan, “Self-Assembly of Chip-Size Components with Cavity Structures: High-Precision Alignment and Direct Bonding without Thermal Compression for Hetero Integration,” *Micromachines*, pp. 49-68, 18 February 2011.

List of Figures

List of Tables

Glossary

2.5D/3D	Integration
AOBS	Acousto-Optical Beam-Splitter
AR	aspect ratio
ATTO 647N	fluorescent labels for the red spectral region
CLSM	confocal laser scanning microscope
CMOS	complementary metal-oxide-semiconductor
DIW	deionized water
DPSS 561 nm	diode pumped solid state
DRIE	deep reactive ion etching
EDS	energy-dispersive X-ray spectroscopy
FPI	fluorophore pressure impregnation
HF	hydrogen fluoride
HyD	hybrid detector
IC	integrated circuit
IPA	isopropyl alcohol
ITRS	international technology roadmap for semiconductors
LUT	look-up-table
MEA	monoethanolamine
MEMS	micro-electro-mechanical systems
NA	numerical aperture
PMT	photomultiplier tube

PTFE	polytetrafluoroethylene
QLUT	Quick Look Up Table
RDL	redistribution layer
RF	radio frequency
$scCO_2$	super critical CO_2
SEM	scanning electron microscopy
SiP	System-in-Package
SoC	System-on-a-Chip
TSE	through silicon-oxide-spaceretch
TSV	trough silicon via
TWE	through-wafer etch
US	ultrasonic
UV	ultraviolet
XPS	X-ray photoelectron spectroscopy